Karlsruhe Institute of Technology

Jingyuan Qu

On Thermoelastic and Poroelastic Metamaterials

2018
Dissertation

On Thermoelastic and Poroelastic Metamaterials

Zur Erlangung des akademischen Grades eines
DOKTORS DER NATURWISSENSCHAFTEN
von der Fakultät für Physik des
Karlsruher Instituts für Technologie (KIT)

genehmigte

DISSERTATION

von

Jingyuan Qu, M.Sc.
geboren in Gießen

Tag der mündlichen Prüfung: 02. November 2018
Referent: Prof. Dr. Martin Wegener
Korreferent: Prof. Dr. Georg Weiß

Contents

Publications

Parts of this thesis have already been published ...
... in scientific journals:

- J. Qu, M. Kadic, A. Naber, and M. Wegener, "Micro-structured two-component 3D metamaterials with negative thermal-expansion coefficient from positive constituents", *Sci. Rep.* **7**, 40643 (2017)
- J. Qu, M. Kadic, and M. Wegener, "Poroelastic metamaterials with negative effective static compressibility", *Appl. Phys. Lett.* **110**, 171901 (2017)
- J. Qu, A. Gerber, F. Mayer, M. Kadic, and M. Wegener, "Experiments on metamaterials with negative effective static compressibility", *Phys. Rev. X* **7**, 041060 (2017)
- J. Qu, M. Kadic, and M. Wegener, "Three-dimensional poroelastic metamaterials with extremely negative or positive effective static volume compressibility", *Extreme Mech. Lett.* **22**, 165–171 (2018)

... at scientific conferences (only own presentations):

- J. Qu, M. Kadic, A. Naber, and M. Wegener, "Micro-structured 3D metamaterials with negative thermal-expansion coefficient from positive constituents", Metamaterials'2016, Crete, Greece, September 2016
- J. Qu, M. Kadic, A. Naber, and M. Wegener, "Poroelastic metamaterials with negative absolute effective static compressibility", Metamaterials'2017, Marseille, France, August 2017

ADDITIONAL RELATED WORK HAS ALREADY BEEN PUBLISHED ...
... in scientific journals:

- M. Hippler, E. Blasco, J. Qu, M. Tanaka, C. Barner-Kowollik, M. Wegener, and M. Bastmeyer, "Controlling the Shape of 3D Microstructures by Temperature and Light", *submitted* (2018)

Chapter 1

1 Introduction

Every single application is based on certain materials with appropriate range of properties. There are optical properties, such as refractive index, electrical properties, such as conductivity, thermal properties, such as thermal expansion and heat capacity, mechanical properties such as elastic modulus and Poisson's ratio, and acoustical properties like speed of sound or acoustic impedance. A lens, for example, requires an ideally large refractive index and a high transparency. At the same time it needs to be form stable, calling for a large Young's modulus and low thermal expansion.

Nature provides us with a large variety of accessible materials, which from a historical perspective helped us to achieve numerous technological advancements. Nevertheless, the limitation for these improvements lies on the point when the requisite properties cannot be reached by available materials. Current technology is, therefore, often limited by the range of currently accessible material properties. Some of these constraints have been overcome by discovering or synthesizing new materials. In addition, available constituent materials can also be used to build composite materials. Two well-known examples are reinforced concrete and carbon fiber reinforced polymer. These composites employ the strength of one component to overcome the weakness of another, for instance, the high tensile strength of steel is protecting the surrounding concrete, which has high compressional strength, but low tensile strength. However, the properties of composites usually lie within the range of their constituents. Reinforced concrete still has lower tensile strength than pure steel [1].

Metamaterials, on the other hand, are generally not limited by their constituents for many material properties. These are artificial materials with unusual effective material properties, that are mainly defined by the structural design rather than the characteristics of the constituents. Not merely can metamaterial properties exceed the bounds given by the constituents,

but they often do by a large magnitude and sometimes even with a different sign [2]. One popular example are metamaterials with negative refractive indices [3], a highly unusual property that is not found in any known natural occurring material. Hence, metamaterials open a new realm of possible material properties. The strength of metamaterials is not only the range of accessible material parameters, but also the ability to tailor them by adjusting simple geometrical parameters.

Discussions about metamaterials often come hand in hand with discussions about 3D printing [2]. The advancement of 3D printing during the last decade has made it possible to print even highly complex three-dimensional metamaterials. In future, the benefit may also be vice versa, as metamaterials endow 3D printers the ability to print materials with a variety of properties from a small number of cartridges. It has even been proven that, theoretically, two constituent materials are enough to print metamaterials with any elastic property [4, 5] or unbounded thermal expansion [6].

In the scope of this work, direct laser writing, a state-of-the-art 3D micro printing technique, is used to fabricate micro-structured three-dimensional metamaterials out of ordinary polymers. The objective is to tailor certain thermoelastic and poroelastic properties, namely thermal expansion and effective compressibility, beyond the range of the constituents. especially towards negative values which is very uncommon. It implies a material that shrinks upon temperature increase, or one that expands under elevated air pressure.

Outline of this Thesis

In Chapter 2, I will cover the theoretical background on classical thermodynamics and continuum mechanics, which is required to understand and interpret the results of this work. It is followed by a short introduction to metamaterials, negative thermal expansion and negative compressibility.

In Chapter 3, the methods I have employed to fabricate and measure our metamaterial samples are described. To begin with, direct laser writing, a three-dimensional laser lithography based on two-photon polymerization, is introduced. Afterwards I will explain the experimental setup and measurement techniques including image cross-correlation.

Chapter 4 covers the experimental results for both thermoelastic and poroelastic metamaterials, which demonstrate our ability to tailor the effective thermal expansion coefficient and effective compressibility. I will present

the design and numerical optimization of the unit cells and demonstrate the novel techniques I have applied to fabricate the two-component samples and the novel designs that include sealed hollow volumes. Moreover, I will measure gas permeation through the microscopic polymer membranes of the poroelastic metamaterials to prove that the sealed hollow volumes are airtight.

In Chapter 5, I will close this thesis with the summary of main results and a brief outlook.

Chapter 2

2 Theory

In the scope of this work, I will characterize and discuss metamaterials with unusual thermoelastic or poroelastic properties. Therefore, I will give a short introduction to thermodynamics and continuum mechanics in this chapter with focus on the parts that are relevant for understanding the later chapters. For a more detailed introduction I recommend the books from Reichl [7] and Slaughter [8]. In the end of this chapter I will talk about bounds of material properties, concentrating on thermal expansion and compressibility, and briefly introduce the concept of metamaterials.

2.1 Fundamentals of Thermodynamics

Classical thermodynamics considers macroscopic systems at equilibrium and the transition between equilibrium states. Based on four simple laws, very fundamental statements about the behavior of a thermodynamic system are made, giving important relations between heat and work and defining temperature and entropy.

Intensive and Extensive State Variables

Each thermodynamic system is fully defined by a set of state variables. Each state variable can be either intensive or extensive. Intensive variables describe quantities that do not depend on the size of the system, like temperature T, pressure P, density ρ or chemical potential μ. If, for example, one system with temperature T is divided into two subsystems, each of them will still be at temperature T.

Extensive variables are additive with regard to the size of the system. Examples are internal energy U, entropy S, volume V or particle number N. If two systems with internal energies U_1 and U_2 are combined, the resulting system will have internal energy $U = U_1 + U_2$.

These state variables and their relations among each other will be described more precisely in the following parts.

Thermodynamic Equilibrium

A system is said to be in thermodynamic equilibrium, if the corresponding state variables stay constant in space and time, which also means that no macroscopic energy or particle flow occurs. Similarly, two equilibrium systems are in thermodynamic equilibrium with each other, if their intensive state variables are equal. When brought into contact with each other, no net energy or particle flow will occur between them. Being in thermodynamic equilibrium is an equivalence relation, as stated in the zeroth law of thermodynamics [7]:

Two thermodynamic systems that are in equilibrium with a third system are in equilibrium with each other.

It assures that intensive properties of a system can be uniquely measured by bringing it into contact with a measurement device like a thermometer.

Ideal Gas

In thermodynamics, gases are often described as an ideal gas, in which the particles are considered to be point like and only interact via elastic collisions. Under this assumption, the pressure P and volume V are found to be proportional to the temperature T (also see 2.1.3) and the amount of substance n, known as the ideal gas law

$$PV = nRT \,. \tag{2.1}$$

The proportionality factor is the gas constant $R = 8.314\,\mathrm{J\,mol^{-1}\,K^{-1}}$. With the Avogadro constant $N_\mathrm{A} = 6.022 \times 10^{23}\,\mathrm{mol^{-1}}$, particle number $N = nN_\mathrm{A}$ and Boltzmann constant $k_\mathrm{B} = R/N_\mathrm{A} = 1.381 \times 10^{-23}\,\mathrm{J\,K^{-1}}$, the ideal gas law can also be written as

$$PV = Nk_\mathrm{B}T \,. \tag{2.2}$$

2.1.1 First Law of Thermodynamics

The first law of thermodynamics is a statement on energy conservation:

Within a closed system, the internal energy U stays constant. It can only be changed by adding heat δQ or mechanical work δW from an external source.

Assuming constant particle number N, it is written as

$$\mathrm{d}U = \delta Q + \delta W. \tag{2.3}$$

Here, the δ indicates that the differentials are not exact, i.e., the corresponding values (here Q and W) can not be expressed as a gradient of another function and depend on the path taken, to change a system from one state to another. The value δW usually represents the volume work performed on the system,

$$\delta W = -P\,\mathrm{d}V, \tag{2.4}$$

but also additional terms are possible, like a change of surface area $\mathrm{d}A$ at surface tension σ or a change of the electrical polarization $\mathrm{d}P$ in an electric field E. These additional terms will be neglected for the rest of this chapter, and only work on the volume is considered.

In a reversible process, during which no energy is dissipated, δQ can be written as

$$\delta Q = T\,\mathrm{d}S. \tag{2.5}$$

This equation introduces the entropy S, an extensive variable that is a quantitative measure of disorder in a system. Later it will be shown that $\mathrm{d}S$ is indeed an exact differential and S a real state variable.

Thermodynamic Potentials

If additionally, particles are allowed to flow in or out of the system, a change in particle number $\mathrm{d}N$ changes the internal energy by $\sum_j \mu_j\,\mathrm{d}N_j$, where μ_j is the chemical potential and N_j the number of the particles of type j. Together with Equations 2.4 and 2.5, the differential of the internal energy can be written as

$$\mathrm{d}U = T\,\mathrm{d}S - P\,\mathrm{d}V + \sum_j \mu_j\,\mathrm{d}N_j\,. \tag{2.6}$$

This equation shows that $(S, V, \{N_j\})$ are the independent variables of U and all other properties can be derived from these via

$$T = \frac{\partial U}{\partial S}\,, \qquad P = -\frac{\partial U}{\partial V}\,, \qquad \text{and} \quad \mu_j = \frac{\partial U}{\partial N_j}\,. \tag{2.7}$$

Depending on the conditions within a system, i.e., depending on which state variables are kept constant, it is convenient to introduce other thermodynamic potentials, namely the Helmholtz free energy $F = U - TS$, the enthalpy $H = U + PV$, the Gibbs free energy $G = U + PV - TS$ and the grand potential $\Phi = U - TS - \sum_j \mu_j \, \mathrm{d}N_j$. With Equation 2.6 their differentials are

$$\mathrm{d}F = -S \, \mathrm{d}T - P \, \mathrm{d}V + \sum_j \mu_j \, \mathrm{d}N_j \, , \tag{2.8}$$

$$\mathrm{d}H = \quad T \, \mathrm{d}S + V \, \mathrm{d}P + \sum_j \mu_j \, \mathrm{d}N_j \, , \tag{2.9}$$

$$\mathrm{d}G = -S \, \mathrm{d}T + V \, \mathrm{d}P + \sum_j \mu_j \, \mathrm{d}N_j \, , \tag{2.10}$$

$$\text{and} \quad \mathrm{d}\Phi = -S \, \mathrm{d}T - P \, \mathrm{d}V - \sum_j N_j \, \mathrm{d}\mu_j \, . \tag{2.11}$$

2.1.2 Carnot Cycle

The Carnot cycle might be the most important cyclic process in thermodynamics. It defines an upper bound for the efficiency of cyclic processes and can also be employed to define an absolute temperature scale, as shown later. Essentially, a system transports heat from a hot reservoir at temperature T_2 to a cold reservoir at temperature $T_1 < T_2$ while generating work during the process. This is done in a cyclic manner through the following steps:

1. Isothermal expansion: The system expands isothermally at temperature T_2 while being in thermal contact with the hot reservoir and insulated from the cold reservoir. In the process, the entropy increases from S_1 to S_2 and the heat $Q_2 = T_2(S_2 - S_1)$ is added to the system.

2. Isentropic expansion: Afterwards, the system is insulated from both reservoirs and is allowed to expand further without heat exchange and at constant entropy S_2 until the temperature drops from T_2 to T_1.

3. Isothermal compression: Now the system is brought into thermal contact with the cold reservoir at T_1 and is compressed by the surrounding. The heat $Q_1 = T_1(S_2 - S_1)$ flows from the system into the cold reservoir.

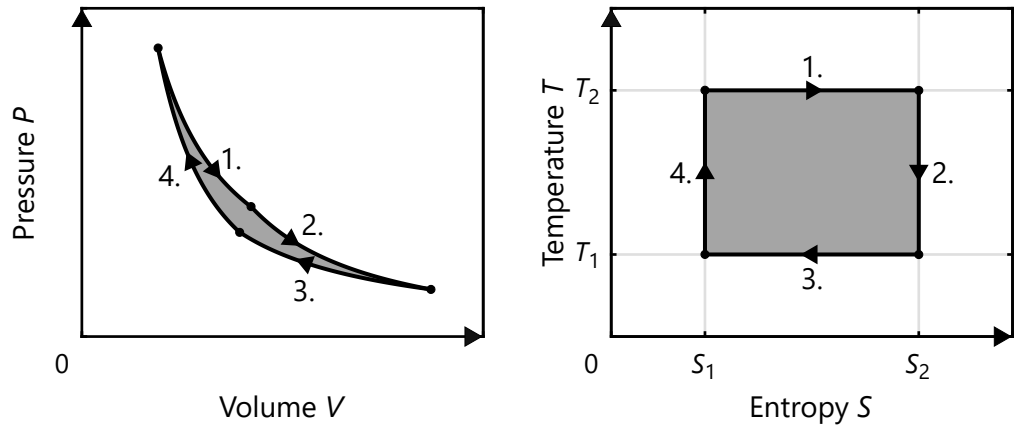

Figure 2.1: PV and TS diagrams of an ideal Carnot process. The net work done after one Carnot cycle is shown in gray on the left and is equal to the difference in heat, shown in gray on the right.

4. Isentropic compression: In the last step, the system is thermally insulated and compressed further while the temperature increases from T_1 to T_2.

In Figure 2.1, the steps are depicted in a PV and a TS diagram. During expansion, the system does work on the surroundings, and during compression, work is done on the system from outside. The difference is the net work W (gray area in the PV diagram) done after one Carnot cycle and is equal to the difference of the heat taken from the hot reservoir and the heat added to the cold reservoir (gray area in the TS diagram)

$$W = Q_2 - Q_1 = (T_2 - T_1)(S_2 - S_1) \, . \tag{2.12}$$

The fraction of the heat Q_2 that is converted into work is the Carnot efficiency

$$\eta = \frac{W}{Q_2} = 1 - \frac{T_1}{T_2} \, . \tag{2.13}$$

2.1.3 Second and Third Law of Thermodynamics

The first law of thermodynamics forbids the existence of a machine that periodically generates energy (perpetuum mobile of the first kind). However, one could imagine a perpetuum mobile that does not violate energy

conservation, for example, a cyclic process that converts heat from only one reservoir into work (perpetuum mobile of the second kind). The second law of thermodynamics states the impossibility of a perpetuum mobile of the second kind. There are lots of other equivalent formulations of the second law. One expressed using the notion of the Carnot cycle states [7]:

No cyclic process has a higher efficiency than the Carnot cycle, and all reversible cycles have the same efficiency.

Another equivalent formulation of the second law, that is based on entropy, will be given in the following.

Temperature and Entropy

An absolute scale of temperature can be defined in several ways. A straight forward method is to use the ideal gas equation (2.2), since it is also the principle of gas thermometers. At constant pressure, an enclosed volume of an ideal gas is found to be proportional to temperature. This defines the absolute zero temperature at a point, where the volume would be zero. However, the assumption of an ideal gas breaks down at low temperature.

This is why instead of the ideal gas law, Equation 2.13 is used. The efficiency of a Carnot cycle defines the relative temperature between two heat reservoirs. To obtain an absolute scale, one temperature value at a fixed state has to be defined. Usually the temperature is chosen at the triple point of water 273.16 K to define the Kelvin scale.

The entropy is then defined via Equation 2.5. For the Carnot cycle, the closed integral over $\delta Q/T$ is zero, which also holds true for any reversible cycle. Therefore, $\mathrm{d}S$ is a real differential (unlike δQ) and the entropy is a state variable,

$$\mathrm{d}S \geq \frac{\delta Q}{T}. \tag{2.14}$$

Equality holds for reversible processes. This inequality is another formulation of the second law, also known as the principle of maximum entropy:

In a closed adiabatic system, entropy cannot decrease and only stays constant during reversible processes.

Third Law of Thermodynamics

To obtain an absolute scale for entropy, one absolute value has to be defined. This is done in the third law of thermodynamics:

It is impossible for any system to reach absolute zero temperature.

An implication of this statement is that the entropy converges to zero for $T \to 0$ in perfect crystals,

$$\lim_{T \to 0} S(T) = 0 \, . \tag{2.15}$$

Statistical Approach

Statistical thermodynamics approaches the field from a microscopic viewpoint via the statistics of particles. A thermodynamic system defined by macroscopic properties like temperature, pressure, or volume is called a macrostate. While the macroscopic properties stay constant at equilibrium, particles within that system still move and occupy different positions. Any arrangement of these microscopic particle positions—or more generally, every configuration of microscopic states—is called a microstate. In this context, there is another very intuitive definition of entropy:

$$S = -k_\mathrm{B} \sum_i P_i \log P_i \, . \tag{2.16}$$

The sum goes over all possible microstates of the macrostate and P_i is the probability of the system to be in state i. Since $P_i \in [0, 1]$ it follows immediately that $S \geq 0$.

If M is the number of microstates, and all are equally probable, Equation 2.16 becomes

$$S = k_\mathrm{B} \log M, \tag{2.17}$$

which implies that the entropy gives the amount of disorder in a system. The larger the number of microstates, the larger the entropy, and if there is only one possible configuration in the system ($M = 1$), the entropy is zero.

With this definition of entropy and by using Equations 2.5 and 2.6, the temperature can alternatively be defined as

$$T = \left(\frac{\partial U}{\partial S} \right)_{V,N} \, . \tag{2.18}$$

The principle of maximum entropy mentioned earlier will be used to derive conditions for the stability of a system. This will give fundamental bounds to the heat capacity and the isothermal compressibility which will be defined in the next subsection.

2.1.4 Thermodynamic Susceptibilities

Thermodynamic susceptibilities specify how much an extensive variable changes as a result of a variation of an intensive variable. Consider a thermodynamic system with fixed particle number N:

To increase the temperature of a system by $\mathrm{d}T$ the heat δQ has to be added to the system. This defines the heat capacity

$$C = \frac{\delta Q}{\mathrm{d}T} = T\frac{\mathrm{d}S}{\mathrm{d}T} \,. \tag{2.19}$$

The heat capacity depends on the circumstances under which temperature is changed. If the volume is kept constant, the heat capacity C_V is obtained. Likewise, the heat capacity C_P is defined under constant pressure. With Equations 2.6 and 2.9 they can be written as

$$C_V = \left(\frac{\partial U}{\partial T}\right)_V \,, \qquad \text{and} \qquad C_P = \left(\frac{\partial H}{\partial T}\right)_P \,. \tag{2.20}$$

The thermal volume expansion coefficient α_V gives the relative volume change with respect to temperature change at fixed pressure,

$$\alpha_V = \frac{1}{V}\left(\frac{\partial V}{\partial T}\right)_P \,. \tag{2.21}$$

Similarly, the (static) isothermal volume compressibility κ gives the relative volume change with respect to pressure change at fixed temperature,

$$\kappa = -\frac{1}{V}\left(\frac{\partial V}{\partial P}\right)_T \,. \tag{2.22}$$

Analogous to α_V, the thermal length-expansion α is defined along one dimension. For now let us assume isotropy and hence equal thermal length-expansion along every direction,

$$\alpha = \frac{1}{L}\left(\frac{\partial L}{\partial T}\right)_P \,. \tag{2.23}$$

With $V = L^3$ it is shown that α_V and α are connected via

$$\alpha_V = 3\alpha \,. \tag{2.24}$$

For the rest of this thesis "thermal expansion" and and "thermal expansion coefficient" will always imply a length expansion. The word "volume" will be added to specify a volume expansion.

Additionally, the following equations hold [9],

$$\left(\frac{\partial P}{\partial T}\right)_V = \frac{\alpha_V}{\kappa} , \tag{2.25}$$

$$\text{and} \quad C_P - C_V = \frac{TV\alpha_V^2}{\kappa} . \tag{2.26}$$

The last equation implies $C_P \geq C_V$ as long as $\kappa > 0$. Equality holds if $\alpha_V = 0$. We will see that indeed $\kappa > 0$ always holds at equilibrium. However, there are also non-equilibrium cases where $\kappa < 0$ is possible.

2.1.5 Fluctuations and Stability

With the principle of maximal entropy, conditions for stability can be derived by looking at small fluctuations around equilibrium. Here, the approach of References [7] and [9] is followed.

Consider a closed system defined by U and V that is split into two equal subsystems. For simplicity, the particle number N is assumed to be constant in each subsystem for now,

$$S(U,V) = S_1\left(\frac{U}{2}, \frac{V}{2}\right) + S_2\left(\frac{U}{2}, \frac{V}{2}\right) . \tag{2.27}$$

U and V are now allowed to fluctuate, changing their values in subsystem 1 by ΔU_1 and ΔV_1, and consequently in subsystem 2 by $-\Delta U_1$ and $-\Delta V_1$. The principle of maximum entropy now implies that any fluctuation in a stable equilibrium can only decrease the entropy,

$$\begin{aligned} 0 \geq \Delta S = S_1\left(\frac{U}{2} + \Delta U_1, \frac{V}{2} + \Delta V_1\right) \\ + S_2\left(\frac{U}{2} - \Delta U_1, \frac{V}{2} - \Delta V_1,\right) - S(U,V) . \end{aligned} \tag{2.28}$$

Looking now at the Taylor expansion of ΔS around the equilibrium situation in Equation 2.27,

$$\Delta S = \left(\frac{\partial S_1}{\partial U_1} - \frac{\partial S_2}{\partial U_2}\right)\Delta U_1 + \left(\frac{\partial S_1}{\partial V_1} - \frac{\partial S_2}{\partial V_2}\right)\Delta V_1 + \dots , \tag{2.29}$$

it can be seen that the linear terms have to vanish, since the fluctuations can be both positive or negative. With Equation 2.6 it follows that $T_1 = T_2$ and $P_1 = P_2$. If also fluctuations in N are considered, the equality $\mu_1 = \mu_2$ of both chemical potentials is shown in the same way.

These are the conditions for two subsystems to be in equilibrium introduced in Section 2.1. As the conditions hold, the partial differentials that are evaluated at equilibrium are equal for both subsystems. The Taylor expansion up to the second order now reads

$$\begin{aligned} 0 \geq \Delta S = &\frac{1}{2}\left(\frac{\partial^2 S_1}{\partial U_1^2} + \frac{\partial^2 S_2}{\partial U_2^2}\right)(\Delta U_1)^2 + \frac{1}{2}\left(\frac{\partial^2 S_1}{\partial V_1^2} + \frac{\partial^2 S_2}{\partial V_2^2}\right)(\Delta V_1)^2 \\ &+ \left(\frac{\partial^2 S_1}{\partial U_1 \partial V_1} + \frac{\partial^2 S_2}{\partial U_2 \partial V_2}\right)\Delta U_1 \Delta V_1 + \dots \\ = &\frac{\partial^2 S_1}{\partial U_1^2}(\Delta U_1)^2 + \frac{\partial^2 S_1}{\partial V_1^2}(\Delta V_1)^2 + 2\frac{\partial^2 S_1}{\partial U_1 \partial V_1}\Delta U_1 \Delta V_1 + \dots \,. \end{aligned} \tag{2.30}$$

The condition $\Delta S \leq 0$ has to hold for all (small) fluctuations of arbitrary sign. This implies that the first two terms on the last line have to be negative,

$$\frac{\partial^2 S_1}{\partial U_1^2} = -\frac{1}{T^2 C_V} \leq 0 \,, \tag{2.31}$$

$$\text{and} \quad \frac{\partial^2 S_1}{\partial V_1^2} \leq 0 \,. \tag{2.32}$$

Together with the inequality $-x^2 - y^2 + 2|xy| \leq 0, \forall x, y \in \mathbb{R}$ it follows that

$$\frac{\partial^2 S_1}{\partial U_1^2}(\Delta U_1)^2 + \frac{\partial^2 S_1}{\partial V_1^2}(\Delta V_1)^2 + 2\sqrt{\left|\frac{\partial^2 S_1}{\partial U_1^2}\frac{\partial^2 S_1}{\partial V_1^2}(\Delta U_1 \Delta V_1)^2\right|} \leq 0 \,. \tag{2.33}$$

Equality can hold for arbitrarily small, but finite $|\Delta U_1|$ and $|\Delta V_1|$. For these fluctuations, Equation 2.33 is inserted into 2.30 to derive the inequality

$$\frac{\partial^2 S_1}{\partial U_1^2}\frac{\partial^2 S_1}{\partial V_1^2} - \left(\frac{\partial^2 S_1}{\partial U_1 \partial V_1}\right)^2 = \frac{1}{T^3 V \kappa C_V} \geq 0 \,. \tag{2.34}$$

From 2.31 and 2.34 it can be seen that heat capacity and compressibility have to be positive, i.e.,

$$C_V \geq 0 \,, \qquad \text{and} \qquad \kappa \geq 0 \,. \tag{2.35}$$

These conditions are implications of the principle of Le Chatelier. Any spontaneous fluctuation from equilibrium leads to a reaction of the system that moves it back towards equilibrium. If that would not be the case, the system would be unstable, and hence, also not in equilibrium. In a system with negative heat capacity, the temperature would increase as a response to a spontaneous outflow of heat due to fluctuations, leading to even more outflow of heat and increase in temperature. Similarly, a system with negative compressibility, would increase its pressure as a response to a spontaneous volume increase, which increases its volume even further.

2.2 Fundamentals of Continuum Mechanics

When studying macroscopic effects of materials, it is convenient to model it as a continuum instead of individual atoms and use a small set of material parameters to describe it. Just like the permittivity ε and the permeability μ, that describe the optical behavior of a material, continuum mechanics uses properties like density, Young's modulus and Poisson's ratio to describe the mechanical behavior. We will first derive some of these properties from Hooke's law.

Hooke's Law

An ordinary helical spring will elongate by x if a force F pulls on it. There is a range where force F and elongation x are proportional to each other, which is described in Hooke's law:

$$F = Dx \, . \tag{2.36}$$

The proportionality factor D is the spring constant, and quantifies the stiffness of the spring. In Figure 2.2, the situation is shown for a helical spring (left) fixed at the top end and pulled on the bottom. There, the elongation x can also be identified as the displacement of the bottom end. On the right, the spring is replaced by a rod with length L and radius $r \ll L$. Assuming an isotropic material under small displacements $x \ll L$, Hooke's law is also valid.

D depends on L and the cross section $A = \pi r^2$ and is, therefore, not a specific property of the material. By replacing the displacement x with the (normal) strain

$$\varepsilon = \frac{\partial x}{\partial L} = \frac{x}{L} \, , \tag{2.37}$$

and the force F with the (normal) stress

$$\sigma = \frac{F}{A} \, , \tag{2.38}$$

Hooke's law can be written in another form,

$$\sigma = E\varepsilon \, . \tag{2.39}$$

This equation introduces the Young's modulus $E = DL/A$, a specific

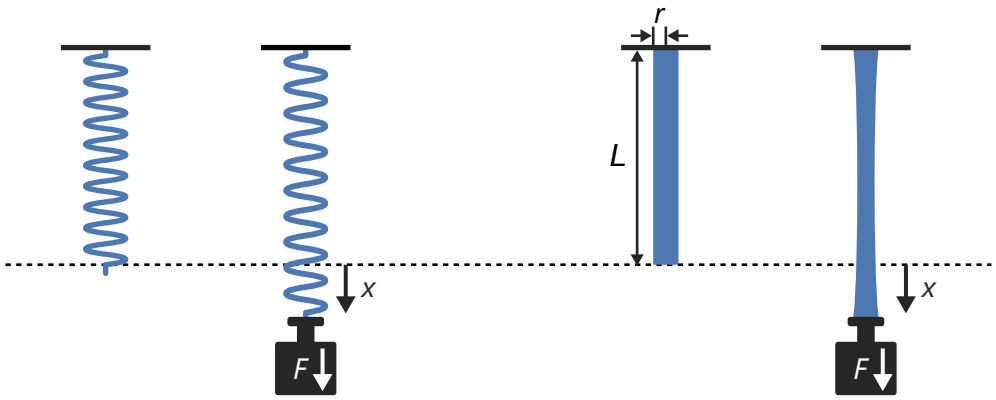

Figure 2.2: A force F that pulls on a spring (left) or a rod (right) will elongate them by x. Within a certain range, F and x are proportional to each other and Hooke's law 2.36 holds.

property that describes the elasticity of the material. The elongated rod in Figure 2.2 also gets thinner. This behavior is described with the Poisson's ratio

$$\nu = \frac{L}{r}\frac{\partial r}{\partial L} \,. \tag{2.40}$$

It is measured in the middle of a long rod to exclude any boundary effects. As we will see later, E and ν together fully define the static behavior of an isotropic material.

Alternatively, the static elastic behavior is described with the bulk modulus K and the shear modulus G. In Figure 2.3, the conditions are illustrated on a cube with volume $V = L^3$. The bulk modulus specifies the resistance of a material with volume V against hydrostatic compression under pressure P,

$$K = -V\frac{\partial P}{\partial V} \,. \tag{2.41}$$

It is the inverse of the compressibility defined in Equation 2.22, in a region where the function $P(V)$ can be inverted.

The shear modulus G quantifies the resistance against a tangential force F_t. It defines the linear dependence between shear stress $\tau = F_t/A$ and shear strain $\gamma = x/L$,

$$G = \frac{\tau}{\gamma} = \frac{F_t/A}{x/L} \,. \tag{2.42}$$

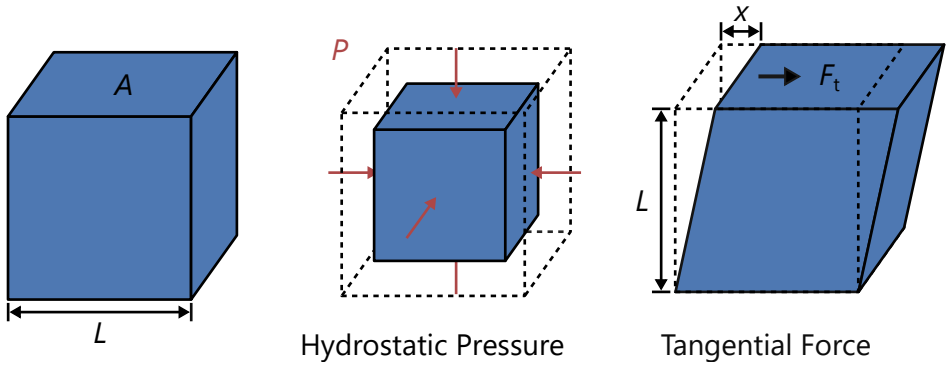

Figure 2.3: A cube of an isotropic material (left) is compressed under hydrostatic pressure (middle) or sheared under a tangential force (richt). The stiffness against these type of deformations define bulk and shear moduli, respectively.

Bulk modulus and shear modulus are related to Young's modulus and Poisson's ratio via

$$K = \frac{E}{3(1-2\nu)} , \qquad \text{and} \qquad G = \frac{E}{2(1+\nu)} . \tag{2.43}$$

E, K and G are positive. As a result, the Poisson's ratio has to lie inside the interval $[-1, 0.5]$ [8].

2.2.1 Continuum Formulation of Linear Elasticity

In continuum mechanics, a body is modeled by an infinite set of points $\mathbb{B}$. Each point $P \in \mathbb{B}$ has a unique initial position in space $\vec{x}(P) \in \mathbb{R}^3$. After a continuous deformation, each point moves to a possibly new position $\vec{X}(P) \in \mathbb{R}^3$.

The difference between positions after deformation and initial positions is the displacement, which is now a continuous vector field

$$\vec{u}(\vec{x}(P)) = \vec{X}(P) - \vec{x}(P) . \tag{2.44}$$

Here the displacement is defined with respect to the initial positions $\vec{x}(P)$. For small deformations, the strain ε can be assumed to be linear to the displacement [8]:

$$\varepsilon_{ij} = \frac{1}{2}\left(\frac{\partial u_i}{\partial x_j} + \frac{\partial u_j}{\partial x_i}\right) . \tag{2.45}$$

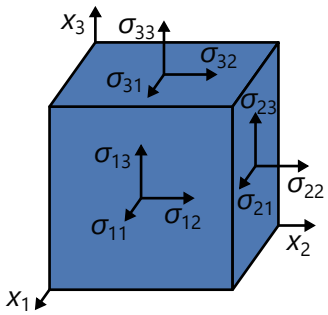

Figure 2.4: Visualization of the normal and tangential stress components on an infinitesimal cube.

It is a symmetric second order tensor containing normal strains on its diagonal and tangential strains on its off diagonal elements. It can be represented in the matrix form

$$\boldsymbol{\varepsilon} = \begin{pmatrix} \varepsilon_{11} & \varepsilon_{12} & \varepsilon_{13} \\ \varepsilon_{12} & \varepsilon_{22} & \varepsilon_{23} \\ \varepsilon_{13} & \varepsilon_{23} & \varepsilon_{33} \end{pmatrix} . \tag{2.46}$$

Likewise, three normal stresses and six shear stresses can influence each point. They are illustrated on an an infinitesimal cube in Figure 2.4. The resulting Cauchy stress tensor is also symmetric [8], leaving only three shear stresses,

$$\boldsymbol{\sigma} = \begin{pmatrix} \sigma_{11} & \sigma_{12} & \sigma_{13} \\ \sigma_{12} & \sigma_{22} & \sigma_{23} \\ \sigma_{13} & \sigma_{23} & \sigma_{33} \end{pmatrix} . \tag{2.47}$$

2.2.2 Constitutive Equations

Stress and strain are connected via a forth order elasticity tensor, giving the generalization of Hooke's law (2.39),

$$\boldsymbol{\sigma} = \mathbf{C} : \boldsymbol{\varepsilon} . \tag{2.48}$$

Component wise and with Einstein notation, it can be written as

$$\sigma_{ij} = C_{ijkl}\varepsilon_{kl} . \tag{2.49}$$

The symmetric stress and strain tensors still have six independent elements, resulting in 36 elements in the elasticity tensor. For isotropic materials the situation is much simpler and only two parameters are necessary to describe the elasticity tensor [8]

$$\sigma_{ij} = 2\mu\varepsilon_{ij} + \lambda\varepsilon_{kk}\delta_{ij} \,. \tag{2.50}$$

λ and μ are the first and second Lamé parameter, respectively. Equation 2.50 can be represented with the Voigt notation as

$$\begin{pmatrix} \sigma_{11} \\ \sigma_{22} \\ \sigma_{33} \\ \sigma_{23} \\ \sigma_{13} \\ \sigma_{12} \end{pmatrix} = \begin{pmatrix} 2\mu+\lambda & \lambda & \lambda & 0 & 0 & 0 \\ \lambda & 2\mu+\lambda & \lambda & 0 & 0 & 0 \\ \lambda & \lambda & 2\mu+\lambda & 0 & 0 & 0 \\ 0 & 0 & 0 & \mu & 0 & 0 \\ 0 & 0 & 0 & 0 & \mu & 0 \\ 0 & 0 & 0 & 0 & 0 & \mu \end{pmatrix} \begin{pmatrix} \varepsilon_{11} \\ \varepsilon_{22} \\ \varepsilon_{33} \\ \gamma_{23} \\ \gamma_{13} \\ \gamma_{12} \end{pmatrix} , \tag{2.51}$$

with $\gamma_{ij} = 2\varepsilon_{ij}$. Comparing this to Equation 2.45, it can easily be seen that γ_{ij} are equivalent to the shear stress γ defined in Equation 2.42. As a result, the second Lamé parameter μ, that connects γ_{ij} with the shear strain, is the shear modulus G.

The first Lamé parameter has no simple physical interpretation. However, it can be represented with other elastic constants. Considering a small hydrostatic pressure increase ΔP acting on an isotropic solid and assuming there are no other stresses present, the pressure increase leads to normal stresses $\sigma_{11} = \sigma_{22} = \sigma_{33} = -\Delta P$. The resulting relative volume change $\Delta V/V$ is the total volumetric strain or dilatation

$$e = \varepsilon_{11} + \varepsilon_{22} + \varepsilon_{33} = \nabla \cdot \vec{u} \,. \tag{2.52}$$

and with Equation 2.51 the bulk modulus can hence be written as

$$K = \frac{\sigma_{11} + \sigma_{22} + \sigma_{33}}{3e} = \frac{(2\mu + 3\lambda)e}{3e} = \lambda + \frac{2}{3}\mu \,. \tag{2.53}$$

The first Lamé parameter can, therefore, be represented by bulk and shear modulus:

$$\lambda = K - \frac{2}{3}G \,. \tag{2.54}$$

In total, five elastic parameters have been introduced (counting $G = \mu$ as one). The static behavior of an isotropic material is fully determined by specifying any two of those. Common pairs are (E, ν), (K, G), and (λ, μ).

Elastic and Acoustic Waves

For the dynamical behavior of elastic solids, another property, the density ρ, has to be taken into account.

Newton's second law is generalized for continuous media according to [5, 10]. The divergence of the stress is a force density, which is connected to an acceleration of a mass density. Neglecting body forces, this is written in the following equation:

$$\rho \frac{\partial^2 \vec{u}}{\partial t^2} = \nabla \cdot \boldsymbol{\sigma} \,. \tag{2.55}$$

For isotropic materials, Equation 2.50 and 2.45 are inserted to obtain a differential equation for the displacement

$$\rho \frac{\partial^2 \vec{u}}{\partial t^2} - (\lambda + 2\mu)\nabla(\nabla \cdot \vec{u}) + \mu \nabla \times (\nabla \times \vec{u}) = 0 \tag{2.56}$$

By applying the divergence on this equation, the rotational term drops out. Together with Equation 2.52 this results in a wave equation for longitudinal waves.

$$\left((\lambda + 2\mu)\nabla^2 - \rho \frac{\partial^2}{\partial t^2} \right) e = 0 \tag{2.57}$$

The longitudinal wave velocity v_L is therefore

$$v_\mathrm{L} = \sqrt{\frac{\lambda + 2\mu}{\rho}} = \sqrt{\frac{K + \frac{4}{3}G}{\rho}} \,. \tag{2.58}$$

Fluids have zero shear moduli and are described by only one elastic constant. Therefore, they only allow propagation of longitudinal waves. Setting $\mu = 0$ in Equation 2.57 the acoustic wave equation

$$\left(\nabla^2 - \frac{1}{v_\mathrm{L}^2} \frac{\partial^2}{\partial t^2} \right) p = 0 \,, \tag{2.59}$$

with $v_\mathrm{L} = \sqrt{K/\rho}$, is obtained. The acoustic pressure p is connected to the dilatation e via $e = -\kappa p$.

Equation 2.56 can be rewritten as

$$\rho \frac{\partial^2 \vec{u}}{\partial t^2} - (\lambda + \mu)\nabla(\nabla \cdot \vec{u}) - \mu \nabla^2 \vec{u} = 0 \,. \tag{2.60}$$

This time the rotation is applied. Remembering that the rotation of a gradient field is zero and with the definition $\mathbf{\Omega} = \nabla \times \vec{u}$, an equation for rotational waves is obtained.

$$\left(\mu\nabla^2 - \rho\frac{\partial^2}{\partial t^2}\right)\mathbf{\Omega} = 0 \tag{2.61}$$

Rotational waves are superpositions of shear or transversal waves. The transversal wave velocity v_T is therefore

$$v_\mathrm{T} = \sqrt{\frac{\mu}{\rho}} = \sqrt{\frac{G}{\rho}}\,. \tag{2.62}$$

2.2.3 Thermoelasticity

Until now, only mechanical stresses and strains were considered. However, also changes in temperature can cause stresses and strains in an elastic solid due to thermal expansion. Generally, thermal expansion can be anisotropic and is described with a symmetric tensor of rank two including all normal and tangential thermal expansion coefficients,

$$\boldsymbol{\alpha} = \begin{pmatrix} \alpha_{11} & \alpha_{12} & \alpha_{13} \\ \alpha_{12} & \alpha_{22} & \alpha_{23} \\ \alpha_{13} & \alpha_{23} & \alpha_{33} \end{pmatrix}\,. \tag{2.63}$$

If the ambient temperature is changed from T_0 to T, the temperature change $\Delta T = T - T_0 =: \theta$ causes a thermal strain $\boldsymbol{\alpha}\theta$. In the elastic stress-strain relations (Equation 2.49), the thermal strain has to be subtracted from the total strain, leading to the Duhamel–Neumann relation [11]

$$\sigma_{ij} = C_{ijkl}(\varepsilon_{kl} - \alpha_{kl}\theta)\,. \tag{2.64}$$

In the following, isotropic solids are considered. The isotropic thermal expansion tensor is proportional to the identity matrix I_3,

$$\boldsymbol{\alpha} = \alpha \begin{pmatrix} 1 & 0 & 0 \\ 0 & 1 & 0 \\ 0 & 0 & 1 \end{pmatrix}\,, \tag{2.65}$$

where α is the coefficient of length expansion defined in Equation 2.23. Equation 2.64 can now be simplified to [11]

$$\sigma_{ij} = 2\mu\varepsilon_{ij} + \lambda\varepsilon_{kk}\delta_{ij} - \beta\theta\delta_{ij}\,, \tag{2.66}$$

with $\beta = (2\mu + 3\lambda)\alpha$.

Equation 2.66 only includes mechanical stresses and strains caused by the temperature change θ. However, the coupling also happens in the other direction: mechanical stresses and strains cause temperature and entropy changes, which occur, for example, in thermoelastic damping [12]. For a full description of thermoelasticity, entropy change per unit volume s as well as temperature change θ have to be considered as individual stress and strain components. For isotropic solids, Equation 2.51 is expanded to [12]

$$\begin{pmatrix} \sigma_{11} \\ \sigma_{22} \\ \sigma_{33} \\ \sigma_{23} \\ \sigma_{31} \\ \sigma_{12} \\ -s \end{pmatrix} = \begin{pmatrix} 2\mu+\lambda & \lambda & \lambda & 0 & 0 & 0 & -\beta \\ \lambda & 2\mu+\lambda & \lambda & 0 & 0 & 0 & -\beta \\ \lambda & \lambda & 2\mu+\lambda & 0 & 0 & 0 & -\beta \\ 0 & 0 & 0 & \mu & 0 & 0 & 0 \\ 0 & 0 & 0 & 0 & \mu & 0 & 0 \\ 0 & 0 & 0 & 0 & 0 & \mu & 0 \\ -\beta & -\beta & -\beta & 0 & 0 & 0 & -c/T_0 \end{pmatrix} \begin{pmatrix} \varepsilon_{11} \\ \varepsilon_{22} \\ \varepsilon_{33} \\ \gamma_{23} \\ \gamma_{13} \\ \gamma_{12} \\ \theta \end{pmatrix} . \quad (2.67)$$

It can be seen that thermal expansion, which is included in β, acts as a coupling parameter between mechanical and thermal behavior. The thermal parameters θ and s are connected via the heat capacity per unit volume c (compare Equation 2.19).

2.2.4 Poroelasticity

Poroelasticity studies the mechanical behavior of elastic solids with pores that are filled with a fluid, often water. A special property of poroelastic materials is the existence of two longitudinal modes, which are coupled modes from a longitudinal wave traveling through the solid and fluid, respectively. A few basic concepts and results obtained by Biot [13, 14] are summarized and brought into our context. For a complete introduction the books [5] and [15] are recommended.

In the following an effective isotropic poroelastic material is considered, consisting of a connected solid skeleton with volume V_s and an open connected pore volume V_p. In the example of a cubic porous structure shown in Figure 2.5, V_s and V_p are the blue and gray parts of the porous volume $V = L^3$, respectively. The volume of the porous material is the sum of solid volume and pore volume,

$$V = V_s + V_p \, . \quad (2.68)$$

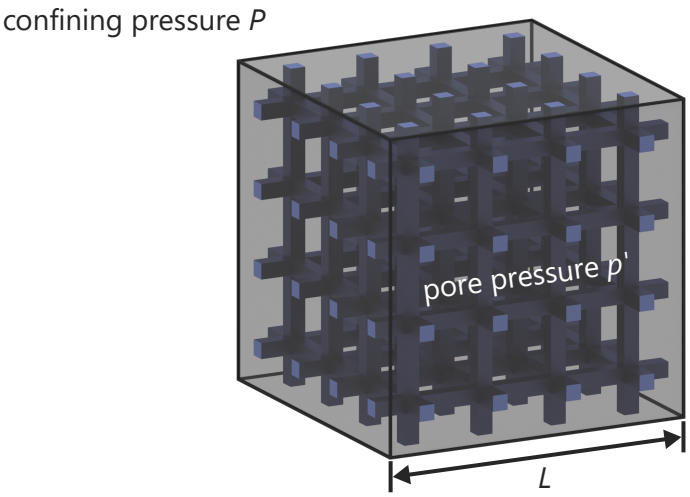

Figure 2.5: Illustration of a cubic porous structure with volume $V = L^3$. The solid portion is depicted in blue, the fluid part with pressure p' is shown in gray. A confining pressure P acts on all six facets of the cube.

The fraction of the pore volume is the porosity $f = V_\mathrm{p}/V$. Depending on which volume is observed under which pressure change, many different coefficients with the units of a compressibility can be defined. The pore pressure p' is the pressure inside the pore fluid and the confining pressure P is the sum of all normal forces acting on the boundary, divided by the area of the boundary (cube facets with area $6L^2$ in Figure 2.5). To keep an overview, all poroelastic volumes, pressures and compressibilities defined in this section are summarized in Table 2.1.

A porous material is said to be saturated if the pores are completely filled with fluid, or drained if the fluid is completely drained from the pores. In a saturated porous solid, stress and strain inside the fluid can interact with the solid portion, which is shown in the constitutive equations.

Poroelastic Constitutive Equations

The constitutive equations of poroelasticity are equivalent to those of thermoelasticity [12, 16]. In the isotropic case they can be written as [14]:

$$\begin{pmatrix} \sigma_{11} \\ \sigma_{22} \\ \sigma_{33} \\ \sigma_{23} \\ \sigma_{31} \\ \sigma_{12} \\ \tilde{\sigma} \end{pmatrix} = \begin{pmatrix} 2\mu + A & A & A & 0 & 0 & 0 & Q \\ A & 2\mu + A & A & 0 & 0 & 0 & Q \\ A & A & 2\mu + A & 0 & 0 & 0 & Q \\ 0 & 0 & 0 & \mu & 0 & 0 & 0 \\ 0 & 0 & 0 & 0 & \mu & 0 & 0 \\ 0 & 0 & 0 & 0 & 0 & \mu & 0 \\ Q & Q & Q & 0 & 0 & 0 & R \end{pmatrix} \begin{pmatrix} \varepsilon_{11} \\ \varepsilon_{22} \\ \varepsilon_{33} \\ \gamma_{23} \\ \gamma_{13} \\ \gamma_{12} \\ \tilde{\varepsilon} \end{pmatrix}, \tag{2.69}$$

with $A = \lambda + Q^2/R$

The similarities with the thermoelastic constitutive equations 2.67 can clearly be seen. Instead of temperature and entropy, now the additional stress and strain components are the stress acting on the contained fluid $\tilde{\sigma}$, which is related to the pore pressure p' via $\tilde{\sigma} = -f p'$ and the fluid dilatation $\tilde{\varepsilon}$ given by

$$\tilde{\varepsilon} = \sum_{i=1}^{3} \frac{\partial U_i}{\partial x_i}, \tag{2.70}$$

with the components U_i of the fluid displacement. There are two additional elastic constants defining the poroelastic properties of the material. Q is a coupling parameter between fluid and solid part and R connects fluid dilatation and stress. μ is the shear modulus, and A corresponds to the first Lamé parameter λ of the drained solid frame. Q and R can be expressed with measurable values from the following two experiments.

Jacketed Compressibility Test

During the jacketed experiment, the confining pressure is increased from the initial value P_0 to $P = P_0 + \Delta P$ while the pore pressure is kept constant at $p' = P_0$. As a result, the incremental force induced by the pressure increase ΔP acts sorely on the solid portion of the porous boundary. Experimentally, this is usually done by sealing the sample inside a jacket and applying a confining pressure. The pore fluid is allowed to escape out of the jacket via a thin tube, to keep the pore pressure constant.

Character	Description
V	volume of porous structure
V_s	volume of the solid skeleton
V_p	pore volume
$f = V_p/V$	porosity
P	confining pressure
p'	pore pressure
κ_{eff}	unjacketed or effective compressibility
κ_j	jacketed compressibility
κ_s	compressibility of the solid skeleton
κ_{fl}	compressibility of the pore fluid

Table 2.1: Summary of characters naming different volume, pressure and compressibility values.

By measuring the relative volume change e (see Equation 2.52), the jacketed compressibility κ_j is determined.

$$\kappa_j = -\frac{1}{V}\left(\frac{\partial V}{\partial P}\right)_{p'=P_0} \approx -\frac{e}{\Delta P} \tag{2.71}$$

Within linear approximation, κ_j can be assumed independent of P_0 and is hence equal to the drained compressibility of the solid skeleton.

Unjacketed Compressibility Test

Here, the jacket is left away and both the confining pressure and the pore pressure are increased by ΔP. In an experiment, the solid skeleton is immersed into a fluid that exerts ΔP as a hydrostatic pressure increase. By measuring e, the unjacketed compressibility is determined.

$$\kappa_{eff} = -\frac{1}{V}\left(\frac{\partial V}{\partial P}\right)_{p'=P} \approx -\frac{e}{\Delta P} \tag{2.72}$$

The unjacketed compressibility will be called effective compressibility later on. To avoid confusion, the symbol κ_{eff} is used for both.

The compressibility of the solid skeleton under hydrostatic loading is defined by

$$\kappa_s = -\frac{1}{V_s}\left(\frac{\partial V_s}{\partial P}\right)_{p'=P} . \tag{2.73}$$

If the solid skeleton consists of only one material and has no sealed hollow volumes, κ_s would be equal to the compressibility of the constituent material.

Under the same experimental conditions, the coefficient of fluid content $\tilde{\gamma}$ is defined by

$$\tilde{\gamma} = \frac{f(e-\tilde{\varepsilon})}{\Delta P} . \tag{2.74}$$

It measures the fluid volume that is injected into the pores of a unit volume of the poroelastic media per hydrostatic pressure increase. There is another way to express this value. If the fluid is incompressible, the volume flow in, or out of the pores is a direct result of a change in pore volume ΔV_p:

$$\tilde{\gamma} = \frac{1}{V}\left(\frac{\partial V_p}{\partial P}\right) = (1-f)\kappa_s - \kappa_{eff} \tag{2.75}$$

For finite fluid compressibility κ_{fl}, there will be an additional volume flow due to compression of the fluid.

$$\tilde{\gamma} = (1-f)\kappa_s - \kappa_{eff} + f\kappa_{fl} \tag{2.76}$$

Poroelastic Constants

The poroelastic constants Q, and R can be written in terms of the measurable values f, κ_j, κ_{eff} and $\tilde{\gamma}$ as [14]

$$Q = \frac{f(1-f-\frac{\kappa_{eff}}{\kappa_j})}{\tilde{\gamma}+\kappa_{eff}-\frac{\kappa_{eff}^2}{\kappa_j}} , \tag{2.77}$$

$$\text{and} \quad R = \frac{f^2}{\tilde{\gamma}+\kappa_{eff}-\frac{\kappa_{eff}^2}{\kappa_j}} . \tag{2.78}$$

The dependence of κ_{eff} is particularly interesting here, as the metamaterials introduced in this work will be able to tune the value of κ_{eff} over a large range and even to negative numbers. At first glance, the denominator seems

to depend on the sign of κ_{eff}. However, by inserting Equation 2.76 for $\tilde{\gamma}$, Q and R are rewritten as

$$Q = \frac{f(1 - f - \frac{\kappa_{\text{eff}}}{\kappa_{\text{j}}})}{(1-f)\kappa_{\text{s}} + f\kappa_{\text{fl}} - \frac{\kappa_{\text{eff}}^2}{\kappa_{\text{j}}}} , \tag{2.79}$$

$$\text{and} \quad R = \frac{f^2}{(1-f)\kappa_{\text{s}} + f\kappa_{\text{fl}} - \frac{\kappa_{\text{eff}}^2}{\kappa_{\text{j}}}} . \tag{2.80}$$

Only κ_{eff}^2 remains in the denominator, which does not depend on the sign of κ_{eff}. κ_{s} and κ_{fl} do not depend on the sign of κ_{eff}, either. The nominator of the coupling parameter Q does depend on the sign of κ_{eff}. However, since usually $\kappa_{\text{eff}}/\kappa_{\text{j}} < 1$ [14], the contribution is rather small.

Longitudinal Poroelastic Waves

In contrast to ordinary elastic waves, it has been predicted and derived by Biot [13] that poroelastic waves have two longitudinal modes. Without coupling these can be seen as two pressure waves traveling through solid and fluid, respectively.

Several densities have to be considered for the dynamic behavior. Let $\rho = \rho_1 + \rho_2$ be the density of an isotropic poroelastic material, ρ_1 the density of the solid portion, and ρ_2 the density of the fluid portion (both with respect to the aggregate volume). Due to coupling between solid and fluid, their relative movement hinders their individual displacement, resulting in an increased apparent mass density of the solid $\rho_{11} = \rho_1 + \rho_a$ and fluid $\rho_{22} = \rho_2 + \rho_a$. The relative movement between solid and fluid enters as a third, negative apparent mass density $\rho_{12} = -\rho_a$. In the kinetic energy T, this can be expressed as [13]

$$T = \frac{1}{2}\sum_{i=1}^{3}\left(\rho_{11}\left(\frac{\partial u_i}{\partial t}\right)^2 + 2\rho_{12}\left(\frac{\partial u_i}{\partial t}\frac{\partial U_i}{\partial t}\right) + \rho_{11}\left(\frac{\partial U_i}{\partial t}\right)^2\right) \tag{2.81}$$

The equation for longitudinal waves are now two coupled equations [13],

$$\begin{aligned} \nabla^2(Pe + Q\tilde{\varepsilon}) &= \frac{\partial^2}{\partial t^2}(\rho_{11}e + \rho_{12}\tilde{\varepsilon}) , \\ \text{and} \quad \nabla^2(Qe + R\tilde{\varepsilon}) &= \frac{\partial^2}{\partial t^2}(\rho_{12}e + \rho_{22}\tilde{\varepsilon}) . \end{aligned} \tag{2.82}$$

with $P = A + 2\mu$. By setting the coupling parameters Q and ρ_{12} to zero, the first equation becomes the equation for ordinary longitudinal elastic waves defined in 2.57.

The wave equation can be solved with an exponential ansatz

$$e = C_1 e^{i(kx-\omega t)} , \qquad \text{and} \qquad \tilde{\varepsilon} = C_2 e^{i(kx-\omega t)} . \tag{2.83}$$

If there is no relative motion between solid and fluid, only one longitudinal wave will exist with the velocity

$$V_c = \sqrt{\frac{H}{\rho}} , \tag{2.84}$$

with $H = P + R + 2Q$.

Generally, two solutions exist, each is a coupled wave of the solid dilatation e and the fluid dilatation $\tilde{\varepsilon}$. For one mode, the amplitudes have the same sign, which means that e and $\tilde{\varepsilon}$ are in phase. For the other mode, the amplitudes are of opposite sign, i.e., e and $\tilde{\varepsilon}$ are out of phase [13]. The velocities of both longitudinal waves can be expressed as

$$V_1 = \frac{V_c}{\sqrt{z_1}} , \qquad \text{and} \qquad V_2 = \frac{V_c}{\sqrt{z_2}} , \tag{2.85}$$

where z_1 and z_2 are the two roots of the equation

$$(\tilde{\sigma}_{11}\tilde{\sigma}_{22} - \tilde{\sigma}_{12}^2)z^2 - (\tilde{\sigma}_{11}\tilde{\rho}_{22} + \tilde{\sigma}_{22}\tilde{\rho}_{11} - 2\tilde{\sigma}_{12}\tilde{\rho}_{12})z + (\tilde{\rho}_{11}\tilde{\rho}_{22} - \tilde{\rho}_{12}^2) = 0 , \tag{2.86}$$

with the nondimensional parameters:

$$\tilde{\rho}_{11} = \frac{\rho_{11}}{\rho} , \qquad \tilde{\rho}_{22} = \frac{\rho_{22}}{\rho} , \qquad \tilde{\rho}_{12} = \frac{\rho_{12}}{\rho} , \tag{2.87}$$

$$\tilde{\sigma}_{11} = \frac{P}{H} , \qquad \tilde{\sigma}_{22} = \frac{R}{H} , \qquad \text{and} \quad \tilde{\sigma}_{12} = \frac{Q}{H} . \tag{2.88}$$

2.3 Bounds of Material Properties

Bounds play an important role in the theory of composites [5]. Understanding the reasons why and under which conditions they exist will usually lead to a better understanding and sometimes even to a refining of the underlying physics. In the previous sections, it was shown that heat capacity and compressibility have to be positive and that the Poisson's ratio of isotropic materials lies in the interval $[-1, 0.5]$. These fundamental "hard" bounds can only be circumvented by introducing new effects or changing initial assumptions. Negative heat capacity exists inside dying stars [17], which are not at equilibrium and have strong gravitational fields, that are not described by classical thermodynamics. Negative compressibility is possible, if, for instance, the requirement of thermodynamic equilibrium is omitted, as we will see later.

There are also "soft" bounds that hold for all or most naturally occurring materials. For example, for all natural materials, Poisson's ratio, refractive index and effective compressibility are positive, and most natural materials have positive thermal expansion. However, for man-made materials, especially metamaterials, these bounds can be exceeded, sometimes even by orders of magnitude. This can lead to new applications that were not possible before.

2.3.1 Metamaterials

The idea of metamaterials is to obtain novel artificial materials with unusual effective properties, and at the same time, to be able to control and tailor them. Instead of a periodic arrangement of atoms or molecules, metamaterials generally consist of a periodic alignment of often complex building blocks, the unit cells. The properties are not limited to specific fields and can, for instance, be of optical [3, 18–20], mechanical [10, 21–23], acoustical [24–27], thermal [28] or electrical [29, 30] nature. They are defined by the structure of the unit cell rather than the constituent materials. Generally speaking, the properties of a metamaterial that is built from different constituent materials do not lie within the properties of its constituents [2]. Often, by tailoring only one structural parameter, the metamaterial effect can be tuned over a large range, sometimes even including sign inversions.

The behavior inside one unit cell can be very complex. For optical metamaterials they can be a result of rapidly oscillating currents or polarization, for

mechanical metamaterials there can be complex deformation fields, including local rotations. In the limit of many unit cells, the complex local behavior vanishes with respect to an effective global behavior. The metamaterial can be described as a homogeneous medium with certain effective material parameters. For wave phenomena, this usually means that the unit cell has to be much smaller than the wavelength.

Metamaterials have refined many material bounds and have especially allowed properties that are usually positive to become negative including negative index of refraction [3, 20, 31], negative Poisson's ratio [22, 32, 33] and negative Hall coefficient [30, 34, 35]. This work will explore the possibility to flip the sign of two other properties that are usually positive: negative thermal expansion and negative effective compressibility.

2.3.2 Negative Thermal Expansion

Unlike compressibility, thermal expansion is fundamentally allowed to be negative. Well-known examples are water between 0 °C and 4 °C and zirconium tungstate ($Zr(WO_4)_2$) between −273 °C and 777 °C [36]. However, most materials have positive thermal expansion: they shown an increase of their volume when heated. The thermal expansion of ideal gases can be directly derived from the ideal gas law 2.1:

$$\alpha = \frac{nR}{VP} = \frac{1}{T} \,. \tag{2.89}$$

It is therefore always positive.

In solids, the usual positive thermal expansion is a result of the anharmonic interatomic potential. A common approximation is the Lennard-Jones potential

$$V_{\mathrm{LJ}}(r) = 4\varepsilon \left[\left(\frac{\sigma}{r}\right)^{12} - \left(\frac{\sigma}{r}\right)^{6} \right] \,, \tag{2.90}$$

which is shown in Figure 2.6. It can be seen that the anharmonicity leads to an increased atomic distance for higher temperatures, which usually results in positive thermal expansion. Exceptions are discussed in the following.

Mie–Grüneisen Equation of State

The connection between an anharmonic interatomic potential and the thermal expansion can also be seen in the Mie–Grüneisen equation of state. It holds

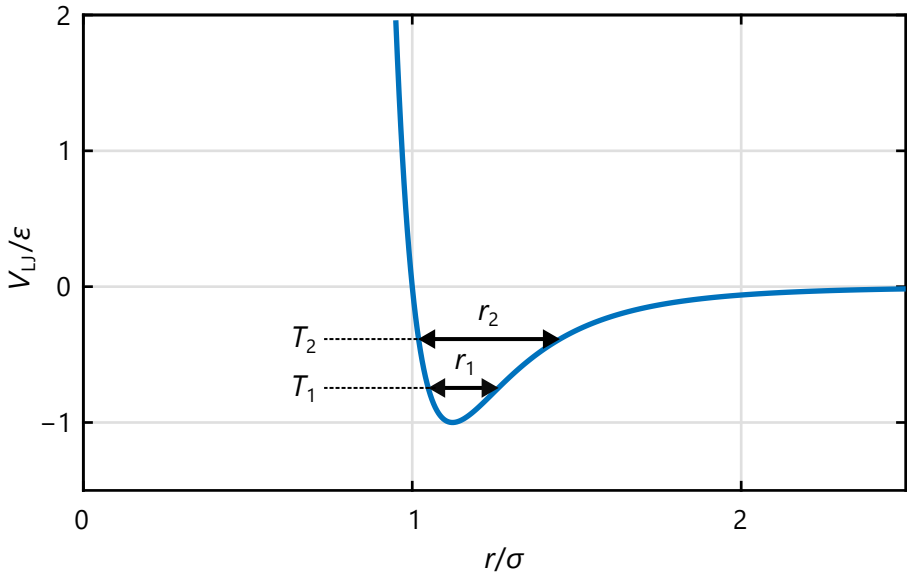

Figure 2.6: Lennard-Jones potential. Due to the anharmonic potential, the average atomic distance increases from r_1 to r_2 if the temperature is increased from T_1 to T_2, leading to positive thermal expansion.

for crystalline solids, for which the thermal behavior is mainly defined by phonons [9],

$$P - P_0 = \gamma \frac{U - U_0}{V} \,. \tag{2.91}$$

Here, P_0 and U_0 are the pressure and the internal energy at a reference state and γ is the dimensionless Grüneisen parameter, that expresses the change of phonon frequencies ω_k of a particular mode with respect to the volume,

$$\gamma = -\frac{\partial \log \omega_k}{\partial \log V} = -\frac{V}{\omega_k}\frac{\partial \omega_k}{\partial V} \,. \tag{2.92}$$

Usually γ is assumed to be independent of k. For an anharmonic potential like in Figure 2.6, ω_k will, in most cases, increase if the volume is decreased, which results in a positive Grüneisen parameter [37].

Using Equation 2.25 and 2.91, the connection between thermal expansion and Grüneisen parameter is shown to be

$$\frac{\alpha}{\kappa} = \left(\frac{\partial P}{\partial T}\right)_V = \gamma \frac{C_V}{V} \tag{2.93}$$

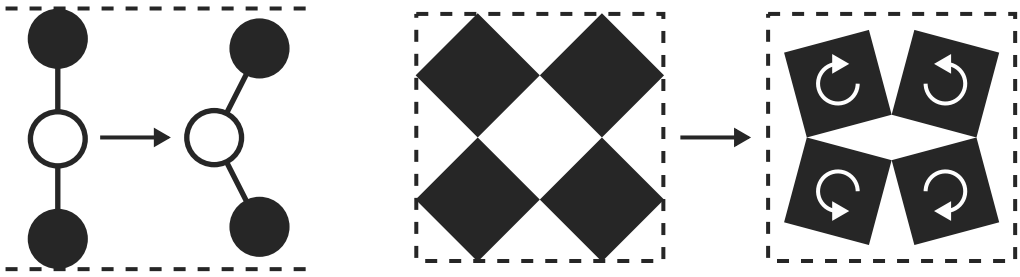

Figure 2.7: Schematic illustration of transverse vibrations (left) and RUMs (right) that can result in a decrease in volume, even if the interatomic bond length increases. Adapted from [38].

$$\Rightarrow \alpha = \gamma \frac{\kappa C_V}{V} \,. \tag{2.94}$$

Generally, different phonon modes can have different Grüneisen parameters γ_i, in which case γ should be understood as a weighted average over γ_i [36]. Since all other parameters on the right side of Equation 2.94 are positive, it follows that if only phonons contribute to the thermal expansion, a negative thermal expansion requires a negative Grüneisen parameter.

Figure 2.7 depicts possible phonon modes with negative Grüneisen parameter are transverse phonons and rigid unit modes (RUMs) [37, 39]. These can lead to negative thermal expansion, even if the interatomic bond length increases with temperature. RUMs account for negative thermal expansion in many solids, like $Zr(WO_4)_2$, in some perovskites [36–38, 40], and the crystalline phase of glass ceramics [41]. There, rigid polyhedra that consist of metal oxides with strong bonds are connected to each other at their edges sharing one oxygen atom. These comparably weak bonds between the rigid units act as hinges, allowing rotational movement of the polyhedra and lead to a decrease in volume with increasing temperature.

Two-Component Materials

It is also possible to obtain negative thermal expansion in a porous composite of two isotropic materials A and B. Assuming two different thermal expansion coefficients α_A and $\alpha_B > \alpha_A$, it has been shown by Lakes that the possible effective thermal expansion coefficients of the composite are, in principle, unbounded in both positive and negative direction [6, 42]. The idea

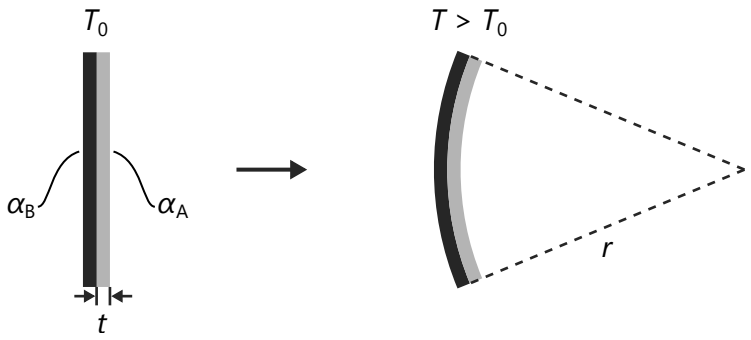

Figure 2.8: A bilayer beam made out of materials A and B with thermal expansion coefficients α_A and $\alpha_B > \alpha_A$ will bend in the direction as illustrated if the temperature is increased from T_0 to $T > T_0$ according to Equation 2.95.

is using bilayer beams in a porous lattice that bend when the temperature changes due to the difference in thermal expansion. These and similar types of two-component materials have recently gained increasing experimental attention [43–48].

The bending of bilayer beams with large length to thickness and width ratios has been investigated analytically by Timoshenko [49]. The mechanism is depicted in Figure 2.8. If both layers have the same thickness t, thermal expansion coefficients of α_A and α_B and Young's moduli E_A and E_B, respectively, a temperature increase of ΔT will lead to a bending of an initially straight beam. Its curvature is given by

$$\tilde{\kappa} = \frac{1}{r} = \frac{(\alpha_B - \alpha_A)\Delta T}{t} \frac{12}{14 + \frac{E_A}{E_B} + \frac{E_B}{E_A}} \,. \tag{2.95}$$

For $t \to 0$ the curvature diverges and hence, thermal expansion using a mechanism based on bending of bilayer beams can be unbounded [42]. The curvature also depends on the ratio of Young's moduli of the constituents and is maximal if they are equal. The effect is only significant at very large ratios, for which the curvature will eventually vanish. For small ratios, the effect is negligible. For instance, if the Young's moduli are different by a factor of 3, the curvature will decrease by less than 8 % compared to the case of equal Young's moduli.

2.3.3 Negative Compressibility

In Section 2.1.5, it was shown that negative static volume compressibility is not possible in thermodynamic equilibrium. It violates the second law of thermodynamics. A thermodynamic system with negative static volume compressibility is therefore unstable. As we will see, stability can be forced via volume constraints, but an active volume constraint that reacts to a change in pressure would violate energy conservation. We will also see that under certain alterations of the assumptions, e.g. "dynamic" instead of "static" or "linear" instead of "volume" it is possible to obtain negative compressibility. But first, an alternative explanation why the static volume compressibility can not be negative is given.

Response Functions and Causality

In the definition of compressibility in Equation 2.22, V and P are volume and pressure of the same thermodynamic system. The derivative indicates that the volume change is observed with respect to the pressure. In equilibrium, the confining pressure of the system is equal to P and acts as a normal force on ∂V. The volume change is therefore a linear response [50] to the change in confining pressure.

Generally, if a time dependent function $F(t)$, e.g. a force, acts on a system leading to a reaction $x(t)$, the linear dependence can be expressed via a response function χ as

$$x(t) = \int_{-\infty}^{\infty} \chi(t - t')F(t')\,\mathrm{d}t' \,. \tag{2.96}$$

Because of causality, $x(t)$ can not depend on future events $F(t' > t)$, and hence, $\chi(t - t') = 0$ for $t < t'$. The mathematical implication is that the complex Fourier-transformed response function $\chi(\omega) = \chi_1(\omega) + \mathrm{i}\chi_2(\omega)$ is holomorphic in the upper half of the complex plane. If $\chi(\omega)$ converges to zero for $|\omega| \to \infty$ with $1/|\omega|$ or faster, it can be shown that its real and

imaginary parts are connected via the Kramers-Kronig relations [7]:

$$\chi_1(\omega) = \frac{2}{\pi}\,\mathcal{P}\int_0^\infty \frac{\omega'\chi_2(\omega')}{\omega'^2-\omega^2}\,\mathrm{d}\omega' \tag{2.97}$$

$$\text{and}\quad \chi_2(\omega) = -\frac{2}{\pi}\,\mathcal{P}\int_0^\infty \frac{\omega\chi_1(\omega')}{\omega'^2-\omega^2}\,\mathrm{d}\omega'\,. \tag{2.98}$$

The Kramers-Kronig relations are well-known from optics, connecting the real and imaginary part of the electric susceptibility or dielectric constant. It has been shown that they also hold for the complex dynamic compressibility [51]. The imaginary parts describe attenuation and are positive for $\omega > 0$ and therefore, it follows from Equation 2.97 that $\chi_1(0) \geq 0$. As a result, the real part of the compressibility can not be negative in the static case.

However, if the volume change is not measured as a response to pressure change, but is rather constrained and the pressure is measured with respect to volume instead, the static bulk modulus and hence, the compressibility can become negative, as we will see in the following.

Negative Compressibility During Buckling

The differential stiffness can be seen as an one-dimensional mechanical analog of bulk modulus. During a common phenomenon called buckling, negative differential stiffness is observed [52, 53], if the force that is acting onto one buckling object is measured under controlled displacement.

Figure 2.9 depicts the force-displacement curve of one buckling element modeled with two linear Hooke's springs and one torsional spring [53]. If the force is measured under displacement control, it follows the solid curve, showing a region with negative differential stiffness (red). Under force control, the curve follows the dashed lines, which are discontinuities in the displacement. If one buckling element is prepared at negative differential stiffness at position 2 under volume control, and the situation is then switched to force control, small fluctuations will cause a jump to position 1 or 3. Therefore, no position on the red part of the curve is stable under force control.

If three buckling elements are arranged in three dimensions, all previous arguments still hold. By replacing "force" with "pressure" and "displacement" with "negative volume change", the red part of the curve represents a

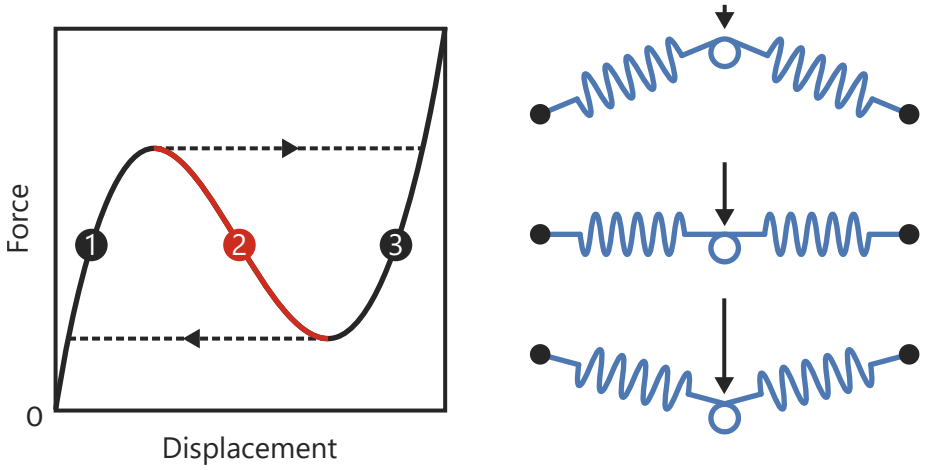

Figure 2.9: Relation between force and displacement of one buckling element, which can be modeled by two linear Hooke's springs and one torsional spring. Under displacement control, the force follows the S-shaped curve, showing a section with negative differential stiffness (red). If the force is controlled, instead of moving along the red part of the curve, the displacement has discontinuous jumps along the dashed lines. Adapted from [53]

region of negative bulk modulus, and hence negative compressibility, which is only observable under volume control. This kind of negative compressibility has been observed in specific foams [54] and was also attributed to a buckling behavior. Just like in the linear case before, the configuration with negative compressibility is unstable under pressure control [55].

Strictly speaking, compressibility is a volume reaction under pressure control and the given buckling examples do not react to a change in confining pressure with negative compressibility. One could principally regain pseudo pressure control using an active volume control mechanism, that reacts to a change in confining pressure with negative compressibility, moving along the red curve of Figure 2.9 to the corresponding pressure value. Even if this kind of mechanism can be achieved, it would need to change the volume against the pressure difference, performing work in the process. In passive media, this is not possible and would violate the first law of thermodynamics.

Negative Compressibility During Transitions

Negative compressibility can occur during transitions between different stable states [56]. A pressure increase can be used to release trapped potential energy, which will move the system to a new stable state at larger volume.

Negative Dynamic Compressibility

Unlike in the static case, a negative dynamic compressibility is possible in resonant metamaterial structures [24, 27, 57–59]. These structures show local resonances under an acoustic pressure wave, which can, for instance, be generated by hard spheres with high density embedded in a soft surrounding material [57]. In a region just above resonance frequency, density and pressure wave have a phase shift of 180 degrees resulting in negative dynamic compressibility.

Negative Linear Compressibility

Very anisotropic materials can show negative linear compressibility or negative area compressibility [60–62], meaning that under increased hydrostatic pressure, these structures are "stretch densified". They expand along one or two dimensions, while shrinking along the other dimensions and getting denser. The volume compressibility is therefore still positive. These materials have potentially interesting applications as artificial muscles or actuators [62].

Negative Effective Compressibility in Porous Materials

It is safe to say that negative static volume compressibility simply does not exist in equilibrium under pressure control. However, it is possible for a stable *porous* material to expand as a response of increased static air pressure without any volume constraints. To understand how this is not a contradiction, we have to specify what the volume of a porous material is, and identify on which volume the air pressure acts.

When talking about the volume of a porous structure, one usually means the effective volume V_{eff}, that includes the volume of the pores (see Section 2.2.4). In the upper panels in Figure 2.10(b) and (c), the effective volume of the cube shaped porous structures with length L is simply L^3. V_{eff} is the intuitive definition of a porous volume. The pores may even be much

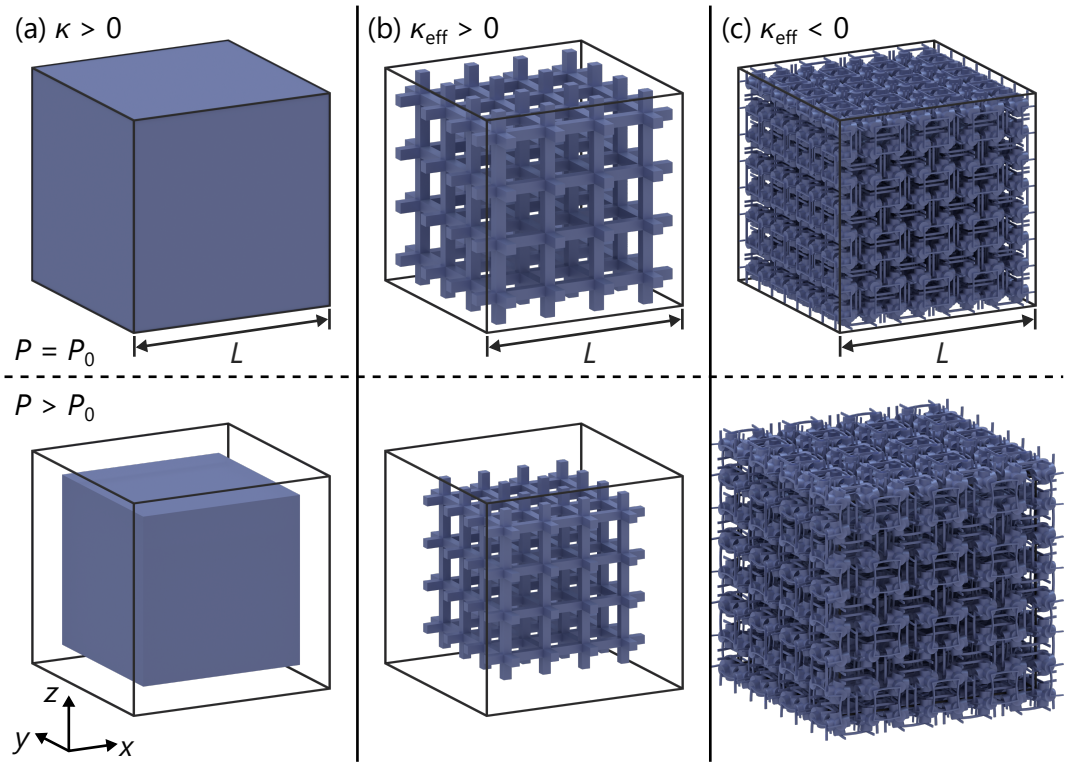

Figure 2.10: Illustration of effective volume change between ambient hydrostatic pressure $P = P_0$ increased hydrostatic pressure $P > P_0$ for (a) ordinary solid material with positive compressibility, (b) porous structure with positive effective compressibility, and (c) poroelastic metamaterial with negative effective compressibility. At $P = P_0$, all structures have the effective volume $V_{\text{eff}} = L^3$ (volume enclosed by the cube). The skeleton volume V_s is the volume enclosed by the outer blue surfaces. All volume changes at $P > P_0$ are largely exaggerated: for (a) and (b) both V_{eff} and V_s decrease, for (c) V_s still decreases, but V_{eff} increases. Adapted from Reference [63].

smaller than the wavelength of light and not resolvable by conventional optics. However, as long as the pores are still much bigger than air molecules, an increased air pressure will also increase the pressure inside the pores. The air pressure is therefore applied on the volume of the solid skeleton V_s (volume enclosed by the blue surfaces in Figure 2.10) rather than V_{eff}. We will call the change in effective volume with respect to hydrostatic pressure effective compressibility

$$\kappa_{\text{eff}} = -\frac{1}{V_{\text{eff}}}\left(\frac{\partial V_{\text{eff}}}{\partial P}\right)_T . \tag{2.99}$$

Comparing with Equation 2.72, the effective compressibility is equivalent to the unjacketed compressibility from poroelasticity. We will keep the notion "effective compressibility", to emphasize that it is an effective metamaterial property. As it always implies a static volume compressibility, we will omit the words "static" and "volume" in later occurrences.

The effective compressibility is usually assumed to be positive [14]. However, this is not a fundamental bound, since it is not a direct response, and neither are confining pressure and effective volume connected in a thermodynamical sense. While V_s can not increase at elevated hydrostatic pressure, V_{eff} can increase (see Figure 2.10). Several ways to obtain negative effective compressibility have been discussed theoretically. For instance, using an arrangement of negative linear compressibility materials [60], or a two-component material [64]. Later, we will introduce metamaterials with negative effective compressibility, and show theoretically and experimentally that by including hollow sealed volumes, only one isotropic solid constituent is necessary and that the modulus of the effective compressibility is at least two orders of magnitude larger than the compressibility of the constituents.

In the next chapter, I will introduce the methods used to fabricate and characterize the metamaterials discussed in the scope of this work.

3 Chapter 3 Methods

In this chapter, I will first describe the three-dimensional laser lithography method which I apply for fabrication of metamaterial samples and the typical work flow connected to it. It is followed by a short introduction on the employed finite-element method using COMSOL Multiphysics. Afterwards, I will present the measurement setup and explain the methods used to measure thermal expansion coefficients and effective compressibilities. It will include a detailed introduction to image cross-correlation, which was employed to measure tiny length changes on our samples. Finally, I will measure the thermal expansion coefficient of copper as a benchmark and quantify small systematic errors.

3.1 Direct Laser Writing

The metamaterials I will introduce in this work require large ratios between sample size and minimum feature size, which is highly demanding for fabrication. In order to fabricate the samples in reasonable time, while still maintaining high precision and quality, a three-dimensional laser lithography method called direct laser writing (DLW) is used.

Basically, DLW is a sub-micron resolution 3D printing technique [65] for structures up to millimeter size [66, 67]. At these structure sizes, deformations due to gravitation are negligible and almost arbitrary three-dimensional designs can be realized without the need of support structure. This technique has enabled the fabrication of complex structures in many different research areas, like photonic crystals [68], optical metamaterials [19, 69], mechanical metamaterials [70] or micro-scaffolds for examination of living cells [71].

DLW uses a focused laser beam, that changes the solubility of a photoresist within its focus volume via a nonlinear effect. By moving the laser focus relative to the sample, a three-dimensional structure is written serially. The

photoresist can either be an insoluble solid that is rendered soluble (positive tone photoresist) or a soluble liquid that is transformed into an insoluble solid by the laser (negative tone photoresist). In the scope of this work we will use the latter: a liquid photoresist that is composed of a photoinitiator and a monomer that can be polymerized. After writing the desired structures, the unexposed photoresist is washed away in a development step.

Two-Photon Polymerization

The photoinitiator contained in the photoresist can be excited via two-photon absorption (or in general multi-photon absorption) [72] to produce radicals that initiate free-radical polymerization of the monomer. At a certain exposure level, the polymerization threshold, enough radicals are created to form an insoluble cross-linked polymer. Usual photoinitiators have a (one-photon) absorption peak at a wavelength of around 400 nm and are therefore excited via two-photon absorption at about 800 nm. Ideally one-photon absorption should be close to zero at the two-photon wavelength.

A nonlinear excitation of the photoinitiator is crucial for writing in three dimensions, as it ensures that the polymerization only occurs within the laser focus. In general, three-dimensional laser lithography is not possible with a linear process like one-photon absorption [73].

The probability for two-photon absorption albeit small, scales with the square of the intensity. Therefore, high intensities are preferable. To avoid thermal damage of the photoresist [74], femtosecond pulsed lasers with high peak intensities at moderate average intensities are used.

Resolution

In general, one has to distinguish between the resolution of DLW and the minimum structure size (or line width), that is defined by the size of the smallest polymerized volume, also called voxel [75]. Due to the threshold behavior, the polymerized voxel has the approximate shape of the volume inside an iso-intensity surface of the laser focus. It is, therefore, elongated along the axial direction, depending on the numerical aperture (NA) of the focusing objective. By changing the intensity of the exposure laser, the size of the voxel will vary and, in theory, can be made arbitrary small. In reality, minimum structure sizes are limited by the sharpness of the polymerization threshold, fluctuations of the laser power, and chemical aspects of the polymerization reaction.

On the other hand, the resolution of DLW is defined by the minimum distance two lines can be written next to each other. This is similar to conventional optical microscopy, where the resolution is defined by the minimum lattice constant a_{xy} of a grating to be resolved. For optical microscopy, the existence of an optical resolution limit has been known since Ernst Abbe published his famous formula in 1873,

$$a_{xy} = \frac{\lambda}{2n\sin(\alpha)} = \frac{\lambda}{2\mathrm{NA}} \,. \tag{3.1}$$

When exposing two parallel lines simultaneously in DLW (e.g. with two laser foci), the intensities add up, and there is a distance, under which no local minimum in the intensity exists and the exposure always results in a single polymerized line. This is the well-known Sparrow-criterion, often used in fluorescence microscopy [76]. At first glance, it seems to be different when writing in sequence, which is the usual case for DLW. However, the photoresist "remembers" prior exposure doses that were below threshold and it can be assumed that sequential exposure doses are accumulated linearly [75]. As a result, also the resolution of sequential writing is limited by optical diffraction. Because of the quadratic dependence of the exposure dose on intensity, the squares of the intensities have to be added to determine the resolution with the sparrow criterion. For calculated focus intensity profiles at a wavelength of $\lambda = 800\,\mathrm{nm}$ and $\mathrm{NA} = 1.4$, a lateral resolution of $a_{xy} = 200\,\mathrm{nm}$ and an axial resolution of $a_z = 500\,\mathrm{nm}$ have been determined [75].

3.1.1 Setup

All metamaterial structures in the scope of this thesis are fabricated by the commercially available DLW system Photonic Professional GT (Nanoscribe GmbH) and the 63×, NA = 1.4 objective (Plan-Apochromat Oil DIC, Carl Zeiss). The setup is shown in Figure 3.1. It uses a frequency doubled erbium fiber laser with a wavelength of 780 nm, a pulse width of under 100 fs and a repetition rate of 80 MHz. An acousto-optic modulator (AOM) tunes the transmitted laser power electronically. From there, the laser beam is widened by two lenses, passes two galvanometric mirrors and is coupled into an inverted microscope. A piezoelectric stage, that is mounted onto a mechanical stage, carries the sample holder.

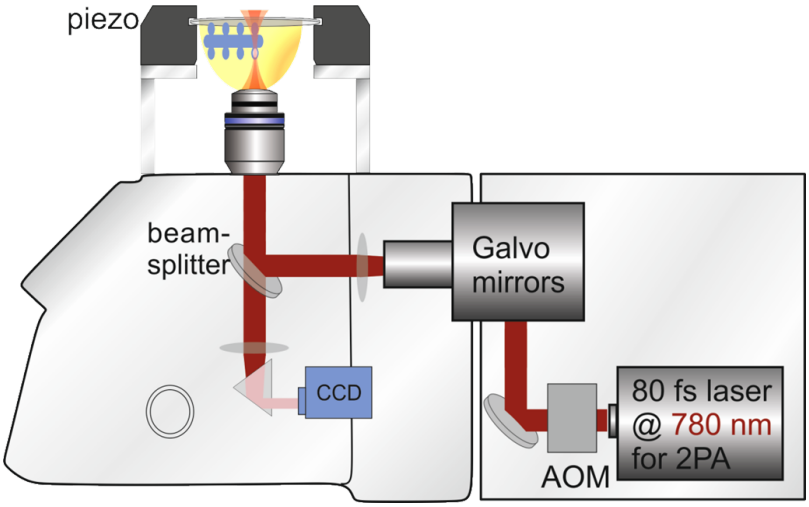

Figure 3.1: Illustration of the DLW setup Photonic Professional GT employed in the scope of this thesis. A femtosecond pulsed laser is coupled into a inverse microscope, where it is focused and polymerizes a liquid photoresist. The piezo stage can move the sample along all three spacial directions and two galvanometric mirrors allow rapid lateral scanning of the laser focus. An acousto-optic modulator adjusts the laser power electronically. The setup is shown in the dip-in configuration, for which the objective is directly immersed into the liquid photoresist. Adapted from [77].

There are different possibilities to move the laser focus relative to the sample to write a structure:

1. The mechanical stage is used, when large lateral movements are needed, like moving between sample positions or writing fields.
2. The z-drive moves the microscope objective axially.
3. The piezoelectric stage allows movement in all three dimensions within a volume of 300 µm × 300 µm × 300 µm.
4. Two galvanometric mirrors allow rapid lateral scanning the laser focus. For the 63× objective, typical scanning speeds lie on the order of 2 cm/s within a circular writing field with a radius of 100 µm.

Writing Configuration

When writing on the top side of a glass substrate, the working distance of the objective fundamentally limits the structure height at 190 µm assuming

a glass cover slip with a thickness of 170 µm. Even before reaching that height, aberrations will deteriorate structure quality, since the laser has to pass already written structures. In order to fabricate taller samples, the so called dip-in configuration [70] is used. There, the objective is directly immersed into the photoresist (also see Figure 3.1) and moves away from the substrate while writing the structure from bottom to top. The refractive index of the photoresist has to be matched to the objective, as it acts both as resist and immersion liquid. Using this method, structure heights of even several millimeters can be realized [67].

3.1.2 Sample Fabrication

In the following, our typical workflow for fabrication of metamaterial structures with DLW is presented.

ITO Evaporation

The substrates are conventional glass cover slips (22 mm × 22 mm × 0.17 mm, Carl Roth). In order to find the interface between substrate and photoresist more easily, the cover slips are cleaned from dust with a paper towel and a nitrogen gun and a thin film (8 nm) of indium tin oxide (ITO) is evaporated via electron-beam evaporation. The cover slips are then tempered at 450 °C for 10 hours during which the ITO film becomes transparent.

Silanization

The ITO substrates are then exposed to air plasma for 30 min to generate hydroxyl-groups at the surface [78] and immersed into a 1 mM solution of 3-(trimethoxysilyl)propyl-methacrylate in toluene for one hour. The trimethoxysilyl-groups bind with the hydroxyl groups, forming a layer of methacrylate groups at the surface, that can react with the monomer during radical polymerization. This way, the later written structure is covalently bound to the surface, which greatly improves the adhesion.

Writing the Structure

Three-dimensional structures are directly imported from a STL-file. Using the software DeScribe (Nanoscribe GmbH), large structures are split into smaller writing blocks and each block is sliced by parallel planes of constant

axial position. Afterwards each slice is hatched into parallel lines. Slicing distance and hatching distance can be freely chosen.

The metamaterial structures are written in the dip-in configuration (see Section 3.1.1) using the 63×, NA = 1.4 objective and the corresponding index-matched photoresist IP-Dip (Nanoscribe GmbH), that is drop-casted onto the silanized substrate. Within one writing block each slice is scanned by the galvanometric mirrors while the piezo stage moves the sample axially after finishing each slice. The mechanical stage and the z-drive are employed to move between different writing blocks, each one approached from the same direction to avoid hysteresis effects.

Development and Supercritical Drying

The written samples are developed in mr-Dev 600 (Micro Resist Technology), which dissolves the remaining liquid monomer. To avoid damages from capillary effects during drying, the samples are transfered into acetone and supercritical dried in CO_2 using the Leica EM CPD030 (Leica Microsystems).

3.2 Finite-Element Calculations

It is convenient to calculate the theoretically expected behavior of our metamaterials to better understand the mechanisms and to be able to optimize geometrical parameters before fabricating actual samples. For this, we use the finite-element method [79] with the commercially available software COMSOL Multiphysics and its Structural Mechanics module. The given problem is solved with the multifrontal massively parallel sparse direct solver (MUMPS). A complex geometry is discretized into small simple elements, which is called the mesh. In our case, the three-dimensional geometry is decomposed into tetrahedrons (typically a number in the order of 10^5). Within each simple element, the equations are solved analytically. To find a solution for the entire geometry, the parameters of the analytical solutions have to be chosen to fulfill certain continuity and boundary conditions depending on the problem, which is done numerically. Generally, results become better for finer meshes and ideally converge to the exact solution in the limit of infinite fine meshes. Of course, also the computing time increases with the mesh size.

To obtain the static mechanical behavior, the static version of Equation 2.55 is solved under the corresponding constitutive equations, which are, if thermal expansion is included, the Duhamel-Neumann relation (see Equation 2.64), and Equation 2.45:

$$\nabla \cdot \sigma = 0 \,, \tag{3.2}$$

$$\sigma_{ij} = C_{ijkl}(\varepsilon_{kl} - \alpha_{kl}\theta) \,, \tag{3.3}$$

$$\varepsilon_{ij} = \frac{1}{2}\left(\frac{\partial u_i}{\partial x_j} + \frac{\partial u_j}{\partial x_i}\right) \,. \tag{3.4}$$

The displacement $\vec{u} = (u_1, u_2, u_3)^T$ only enters as a derivative, which means that boundary conditions that fix the absolute value of $\vec{u}$ are required.

Later, we will compute the phononic band structure of a periodic structure, including a surrounding fluid. For the solid part, the Fourier transform of Equation 2.55 is solved:

$$\nabla \cdot \sigma = -\rho\omega^2\vec{u} \,. \tag{3.5}$$

For the fluid portion, the Fourier transform of Equation 2.59 is solved:

$$\left(\nabla^2 + \frac{\omega^2}{v_L^2}\right) p = 0 \,, \tag{3.6}$$

At the boundary between solid and fluid, the connection between the normal components of force and acceleration is implemented via

$$\vec{n} \cdot \frac{\nabla p}{\rho} = \vec{n} \cdot \frac{\partial \vec{u}}{\partial t^2} \, . \tag{3.7}$$

The eigenfrequencies at fixed wave vectors $\vec{k}$ are calculated with a Bloch wave ansatz,

$$\psi(\vec{r}) = u(\vec{r}) \mathrm{e}^{i\vec{k}\cdot\vec{r}} \, , \tag{3.8}$$

with a lattice periodic function $u(\vec{r})$.

3.2.1 Boundary Conditions

For simplicity, let us consider one simple cubic unit cell with lattice constant a centered and aligned to an ordinary Cartesian coordinate system.

Open Boundaries

Open boundaries are those that have no additional constraints imposed on them.

Fixed Constraint

A fixed constraint at a boundary sets the displacement to zero, $\vec{u} = \vec{0}$.

Periodic Boundary Conditions

To obtain static effective (meta)material parameters, the limit of infinite number of unit cells is considered. For a cubic translational lattice, the normal components of the displacement vector on opposite cube facets with respect to the center have opposite sign. For instance, along the x-axis, it is implemented by $u_1(a/2, y, z) = -u_1(-a/2, y, z) \; \forall y, z \in [-a/2, a/2]$.

Floquet-Bloch Periodicity

For the calculations of eigenmode frequencies, Floquet-Bloch periodicity is used to mimic an continuous crystal for the wave. This is done by adding a phase factor $\exp(ik_x l)$ after a distance of l along the x-direction,

$$\vec{u}(l/2, y, z) = \vec{u}(-l/2, y, z) \mathrm{e}^{ik_x l} \, , \tag{3.9}$$

and analogous for y and z-directions.

3.3 Measurement

Since the microscopic samples are rather fragile, it is very challenging to measure length changes. In order to determine the thermal expansion or the effective static compressibility, microscopic images are taken at different temperatures or air pressures, respectively. From these images we extract the length changes directly via image cross-correlation analysis.

3.3.1 Experimental Setup

An illustration of the measurement setup is shown in Figure 3.2. The whole setup is fixed on a damped optical table. The sample chamber can be translated along all three dimensions using a piezo stage and a manual stage. Metamaterial samples are put inside a chamber and are illuminated by a diffuse light source made from white LEDs and diffusive foil. The samples are imaged through a window on top of the chamber using an infinity color corrected 20×, NA = 0.4 objective (LD Achroplan, Carl Zeiss AG), a tube lens with a focal length of $f = 100\,\mathrm{mm}$ (AC254-100-A-ML, Thorlabs) and a camera (BFLY-PGE-50H5M-C, Point Grey Research). The tube lens is placed in a distance of 100 mm to the camera sensor (a charge-coupled device), so that the chief rays between objective and tube lens are approximately parallel. Using a focal length of 100 mm instead of the standard focal length of 165 mm results in a magnification of about 12.12×. Camera and piezo stage are connected to a computer via an I/O data acquisition device (PCIe-6363, National Instruments), which allows automatic acquisition of images and sample positioning.

Two different sample chambers are used: one for temperature-controlled measurements and one that allows measurements under controlled hydrostatic pressure.

Heating Chamber and Temperature Control

The chamber designated for temperature controlled measurements is illustrated in Figure 3.2(b). It is made out of copper and has a glass window on top for imaging. Via two holes, one on the bottom and one on the top, temperature is monitored using Pt100 resistance thermometers. A Peltier element below pumps heat from the heat sink into the chamber or vise versa, thus heating or cooling the chamber in the progress. On the very bottom,

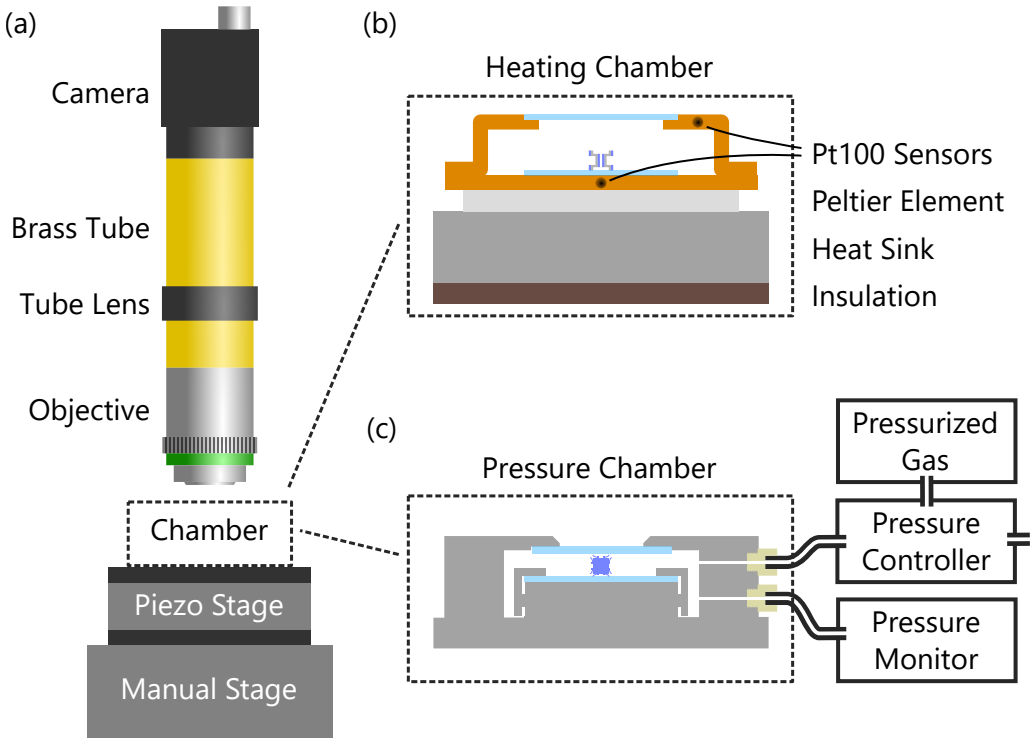

Figure 3.2: (a) Schematic measurement setup used in the scope of this thesis. The sample sits inside the chamber and is positioned with a manual stage and a piezo stage. A self built microscope made out of a 20×, NA = 0.4 objective, a $f = 100\,\text{mm}$ tube lens and a camera is utilized to image the samples. To allow different measurement types, either a heating chamber (b), or a pressure chamber (c) can be mounted on top of the piezo.

a plate made out of phenolic paper insulates the piezo, protecting it from thermal damages.

The temperature of the chamber is computer-controlled. We use two PT100 transducers (Pollin Electronic) to convert the linear Pt100 resistance dependence into a linear voltage range from 0 V for a temperature of 0 °C to 1 V for 100 °C. There are two potentiometers on each PT100 transducer to adjust the offset and the slope of the output voltage.

To calibrate the Pt100 resistances, they were insulated in paraffin film and immersed in deionized water. A high precision thermometer (GMH 3710, Greisinger) was employed to monitor the actual temperature in the water. First the water was cooled to near 0 °C using water ice, and the offset potentiometer was adjusted until the output voltage had the correct value

near 0 V. For the second calibration point, the water heated until 60 °C and the output voltage was calibrated to 0.6 V using the potentiometer assigned for the slope.

Pressure Chamber and Pressure Control

For pressure-controlled measurements, an airtight pressure chamber made out of aluminum is used (see Figure 3.2(c)). A 1 mm thick and 20 mm diameter cover slip is glued from the inside, sealing a 12 mm diameter hole on top of the chamber. Samples sealed inside the chamber can be imaged through this glass window.

The chamber is usually connected to filtered and pressurized air at an overpressure of $\Delta P = 5$ bar, but also other gases like CO_2 can be used. A computer controlled pressure controller (PQ1, AirCom) between chamber and pressurized gas adjusts the pressure inside the chamber proportional to the voltage applied by the data acquisition device. For this, an internal pressure transducer measures the pressure and actively triggers two valves that control both inlet and outlet until the desired pressure is reached, keeping it constant at that pressure. For an input overpressure of 5 bar, the pressure controller is able to adjust the overpressure inside the chamber from $\Delta P = 0$ bar to $\Delta P = 4.2$ bar. Additionally, the chamber pressure is observed with an digital pressure monitor (DC 400, tecsis). To stay away from possible inaccuracies for pressure control, we apply a maximum overpressure of $\Delta P = 3.8$ bar for the measurements.

3.3.2 Autofocus

During measurement, the sample can move out of focus. Especially during temperature controlled measurements, thermal expansion of the whole chamber causes unwanted motion. As the cross-correlation analysis relies on the quality of images, an autofocus algorithm is used to get rid of this problem as much as possible.

A focused image appears sharp because high frequency intensity fluctuations, typically at edges or small features, are resolved. Any value F_{image} that correlates with the sharpness of an image can be used and the optimal focal position is determined by at its maximum [80, 81]. Here, the sharpness is calculated by summing up all squared gray value differences of pixels

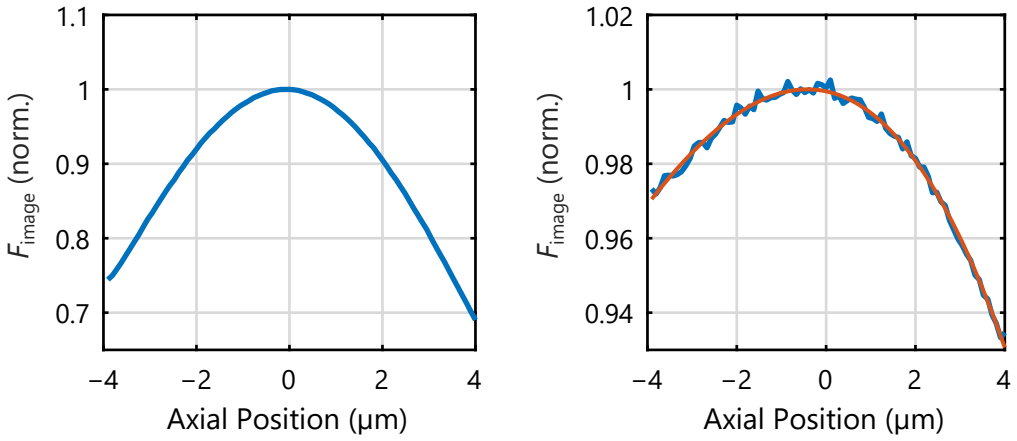

Figure 3.3: Calculated normalized F_{image} for images of a copper surface (left) and a plane within a three-dimensional metamaterial sample (right) taken over different axial positions. The right curve shows much more noise and is fitted with a cubic function (red). The peak position determines the best focused image.

neighboring along the x-axis:

$$F_{\text{image}} = \sum_{x=2}^{x_{\max}} \sum_{y=1}^{y_{\max}} \left(g(x,y) - g(x-1,y)\right)^2, \tag{3.10}$$

where $x_{\max}$ and $y_{\max}$ are the width and height of the image, respectively and $g(x,y)$ are the gray values of the pixels.

The implemented focusing algorithm works as follows: Starting at an axial position of z_0, the piezo stage is used to move from $z = z_0 - \Delta z$ to $z = z_0 + \Delta z$ during which N images are taken. A common choice is $\Delta z = 4\,\mu\text{m}$ and $N = 84$, which means that consecutive images are taken less than 100 nm apart. For these images, F_{image} is calculated and fitted using a cubic function (see Figure 3.3). The piezo stage then moves to the new axial position of the optimum focal point identified by the maximum in the fit and the image that was taken closest to that position is saved.

In Figure 3.3, F_{image} is plotted over the axial position. On the left, it is calculated for images of a copper surface, showing a smooth curve and a clearly defined maximum. Only 4 µm away from the peak position, F_{image} drops by about 30 %. The situation for a three-dimensional metamaterial sample is shown on the right. The peak can still be clearly identified, but

F_{image} now only drops by about 5 % at a distance of 4 µm from the maximum, and the data is more noisy, making it necessary to perform a curve fit.

3.3.3 Normalized Image Cross-Correlation

The measurement setup described in this section can take microscopic images of metamaterial samples either at different temperatures or at different gas pressures. Out of these images alone, it is possible to extract the thermally or pressure-induced deformations using normalized image cross-correlation [82]. The data can be used to observe the operation principle of the metamaterial and to calculate the thermal expansion coefficient [46], or effective static compressibility [83, 84]. Normalized image cross-correlation is a powerful tool and has also been applied in many other works in the past [22, 66, 67].

The cross-correlation between two functions $f, g \in L^2(\mathbb{R})$ is defined as

$$(f \star g)(\tau) = \int_{-\infty}^{\infty} f^*(t) g(t+\tau)\,\mathrm{d}t, \tag{3.11}$$

or for discrete values

$$(f \star g)(\tau) = \sum_{t=-\infty}^{\infty} f^*(t) g(t+\tau). \tag{3.12}$$

The normalized image cross-correlation is a normalized two-dimensional version of Equation 3.12 and compares two images. We will call one image the reference and the other one the region of interest (ROI). The reference is usually part of an image taken at reference conditions (e.g. room temperature, or atmospheric pressure) and the ROI a smaller region of the reference, or a region of an image taken at different conditions. For simplicity, reference and ROI shall both have an odd number of pixels, and the origin $(0,0)$ of the coordinate system is moved onto the center pixel.

To calculate the two-dimensional cross-correlation $C(\Delta x, \Delta y)$, the averages are subtracted from the gray values to define I_{ROI} and I_{ref}:

$$I_{\text{ROI}}(x,y) = g_{\text{ROI}}(x,y) - \bar{g}_{\text{ROI}} \tag{3.13}$$

$$I_{\text{ref}}(x-\Delta x, y-\Delta y) = g_{\text{ref}}(x-\Delta x, y-\Delta x) - \bar{g}_{\text{ref}}(\Delta x, \Delta y) \tag{3.14}$$

Here, $\bar{g}_{\text{ROI}}$ is the mean gray value of the ROI and $\bar{g}_{\text{ref}}(\Delta x, \Delta y)$ is the mean of

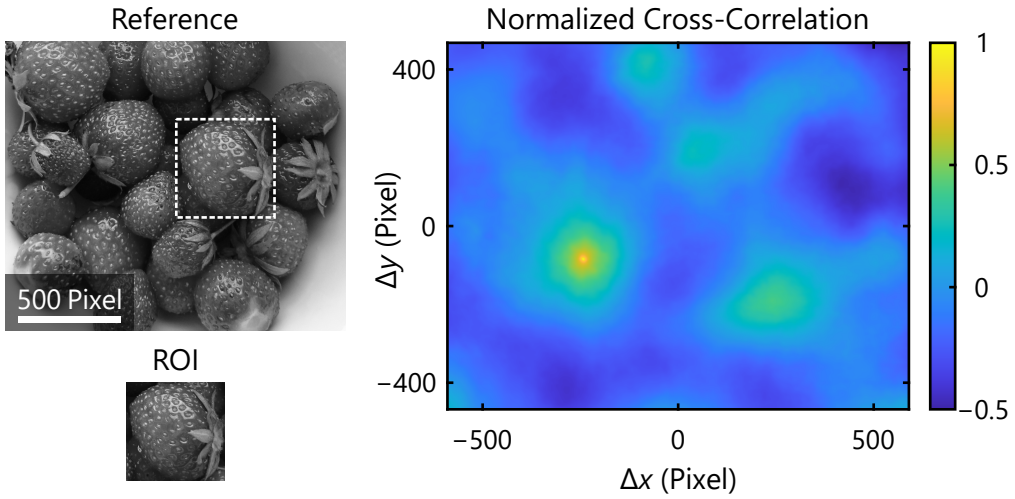

Figure 3.4: Calculated normalized cross-correlation $C(\Delta x, \Delta y)$ between the reference and the ROI. A clear peak can be seen. The position of the maximum represents the displacement between ROI and reference.

$g_{\text{ref}}(x - \Delta x, y - \Delta x)$ for (x, y) inside the ROI. Outside their respective areas, I_{ROI} and I_{ref} are set to zero. The image cross-correlation now reads [82]:

$$C(\Delta x, \Delta y) = \frac{\sum_{x,y} I_{\text{ref}}(x - \Delta x, y - \Delta y) I_{\text{ROI}}(x, y)}{\sqrt{\sum_{x,y} I_{\text{ref}}(x - \Delta x, y - \Delta y)^2 \sum_{x,y} I_{\text{ROI}}(x, y)^2)}} \tag{3.15}$$

The denominator is a normalization factor.

Figure 3.4 shows an example of calculated $C(\Delta x, \Delta y)$ between a reference and a ROI. Whenever the ROI is overlapping with the same, or a similar area of the reference, $C(\Delta x, \Delta y)$ shows a local maximum. In the example, a clear single absolute maximum can be seen at $(\Delta x, \Delta y) = (-242, -84)$. This is the displacement vector of the ROI with respect to the reference.

Sub-Pixel Position Tracking

The image cross-correlation described above can be used to track pixel positions over different images with sub-pixel precision. The algorithm used for that is based on the freely available software package *Digital Image Correlation and Tracking* for Matlab [85]. The principle is shown in the following.

First a set of pixel positions is chosen on the reference image. For each pixel position, the reference is cropped into a quadratic image, the reference area, with length $4n_{\text{corr}} + 1, n_{\text{corr}} \in \mathbb{N}$ and with the chosen pixel position being in the center. This reference area is now compared with a set of measurement images. On the first image, a quadratic ROI of length $2n_{\text{corr}} + 1$ is chosen around the initial pixel position and the cross-correlation between ROI and cropped reference is calculated. By finding the absolute maximum of the cross-correlation, the displacement vector is obtained. For the next image, the position of the ROI is updated by the calculated displacement vector and the procedure is repeated.

The updating of the ROI enables tracking of large continuous movements. Between two consecutive images, however, Δx or Δy should not be larger than n_{corr}, or else ROI and reference area will not fully overlap. If the overlap is too low, the algorithm can generate wrong results.

To obtain sub-pixel precision, in addition to finding the absolute maximum in the cross-correlation, the eight neighboring values around the maximum are selected. These 3×3 correlation values are then fitted with a two-dimensional parabola and its maximum position gives a displacement vector with a typical precision of at least $1/10$ of a pixel.

Limiting Factors

The value n_{corr}, that determines the size of the ROI and the reference area, has to be carefully chosen. Larger values will increase the precision, and, as described before, allow larger displacements between consecutive images. However, the calculation averages over the whole ROI. Therefore, when local displacements are tracked, the ROI cannot be much larger than the moving part.

Furthermore, if repeating patterns or translational invariance of the ROI are present, image cross-correlation will easily fail, since there will multiple maxima (see Figure 3.5). The ROI A chosen on top of the pen is (approximately) locally translational invariant. The cross-correlation shows a long line of highly correlating values instead of one well distinguishable peak. If the ROI B is chosen on one out of three thumbtacks, three maxima can be seen in the cross-correlation instead of one. Over a set of measurement images, peak finding may even jump between different maxima. Especially for metamaterials, that consist of periodically repeated unit cells, the size of the reference area $4n_{\text{corr}} + 1$ has to be chosen adequately, for instance, not

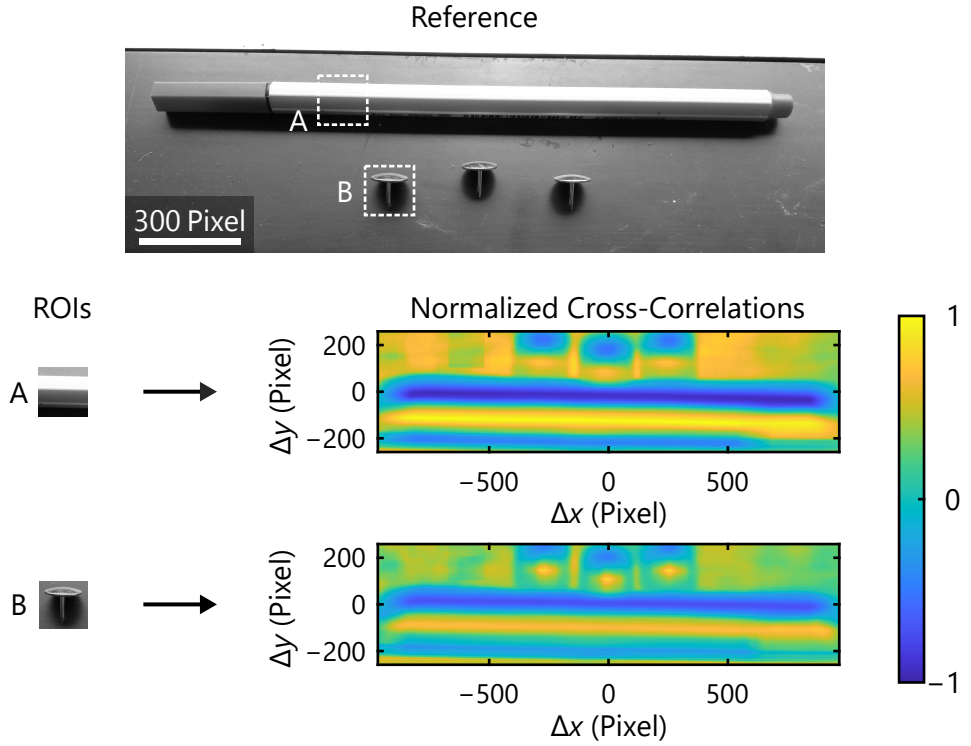

Figure 3.5: Visualization of a situation, where position tracking with normalized image cross-correlation can be unsuccessful. Instead of one peak, the cross-correlation between the reference image and the ROI on the pen shows a line of highly correlating values. Cross-correlation using the ROI on the thumbtack shows three maxima.

larger than one unit cell.

3.3.4 Thermal Expansion Coefficient of Copper

With the ability to track positions with sub pixel accuracy, very precise length changes can be measured from camera images alone. As a benchmark test, we have calculated the thermal expansion coefficient of copper from one reference image taken at room temperature (RT) and one image taken under a temperature increase of $\Delta T = 20\,\mathrm{K}$. The literature value at room temperature is $\alpha_{\mathrm{Cu}} = 1.65 \times 10^{-5}\,\mathrm{K}^{-1}$) [86], which means that over the length of 1000 pixels, a temperature increase of $\Delta T = 20\,\mathrm{K}$ only causes a length change of 0.33 pixels.

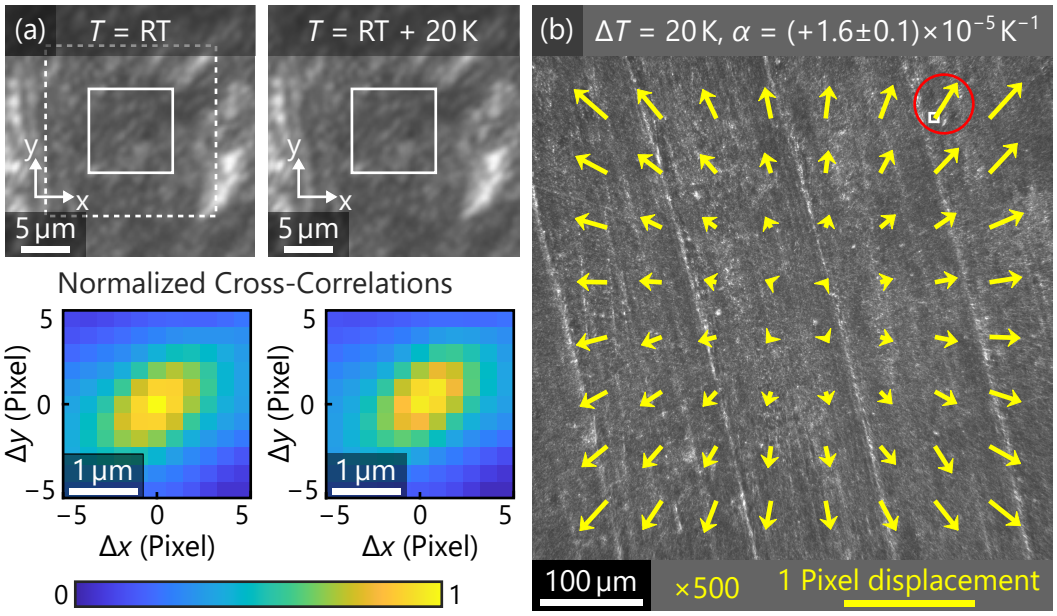

Figure 3.6: Image cross-correlation analysis of the surface of a copper block. (a) Zoomed-in views of one reference image taken at room temperature RT (left) and one image taken under a temperature increase of $\Delta T = 20\,\mathrm{K}$ (right), with small ROIs (solid white squares) and one reference area (dashed white square) with size $n_{\mathrm{corr}} = 16$. Cross-correlations between each ROI and reference area are calculated, showing a peak at zero displacement for the left ROI and a shifted peak for the right ROI, corresponding to a finite displacement vector $(\Delta x, \Delta y)$. (b) Calculated Displacement vector field on the surface. The mean displacement vector has been subtracted to visualize the thermal expansion. For visibility, all vectors are stretched by a factor of 500. ROI and displacement vector corresponding to (a) are indicated by a red circle. By averaging over all arrows, a thermal expansion coefficient of $\alpha = (1.6 \pm 0.1) \times 10^{-5}\,\mathrm{K}^{-1}$ is obtained. Reproduced from Reference [46].

Figure 3.6 illustrates the cross-correlation analysis to calculate the thermal expansion of copper. 64 individual pixel positions over the whole imaged surface are tracked with the same correlation size $n_{\mathrm{corr}} = 16$ as is later used for the thermal expansion measurements of our metamaterials. For one of these positions (red circle), zoomed-in views are shown in Figure 3.6(a) including the small ROIs of 33×33 pixels (solid white squares) and the reference area (dashed white square) of 65×65 pixels. The peak of the cross-correlations moves from zero at room temperature towards the upper left at $\Delta T = 20\,\mathrm{K}$ with a finite displacement vector $(\Delta x, \Delta y)$. After all

displacement vectors have been calculated, the mean displacement vector is subtracted, which removes any global translation of the sample. The resulting vectors are plotted in Figure 3.6(b) with a stretching factor of 500, showing an isotropic expansion. The yellow bar on the bottom indicates the length of a vector showing a displacement of one pixel (with the same stretching factor). All displacement vectors are therefore much shorter than one pixel, demonstrating a very high tracking precision. With the calculated displacement vectors, relative length changes with respect to their mean position are calculated and averaged over all pixel positions. The resulting thermal expansion coefficient $\alpha = (1.6 \pm 0.1) \times 10^{-5}\,\mathrm{K}^{-1}$ agrees well with the literature value.

3.3.5 Small Magnification Errors due to Window Warping

In contrast to the thermal expansion coefficient, the compressibility of copper can not be measured in our current setup, because of its large bulk modulus of 142 GPa [87]. Even at the largest overpressure of 3.8 bar $= 3.8 \times 10^5$ Pa, this results a relative length change of only -9×10^{-7}, which is practically undetectable.

Nevertheless, we have performed pressure-controlled measurements of $\Delta L/L$ on a piece of copper to detect possible systematic errors in our measurement setup. Surprisingly, the copper piece has seemingly expanded under pressure increase, which is, of course, not possible. The origin of this systematic error is an optical artifact, caused by outwards warping of the chamber window, through which the samples are imaged, at increased chamber pressure.

To quantify the magnitude of this effect, we have performed finite-element calculations with COMSOL Multiphysics (see previous Section). A pressure increase of 3.8 bar was introduced as normal forces on all interior surfaces of the chamber. The bottom layer of the chamber was fixed in position and all other boundaries were unconstrained. For the aluminum parts, we use standard literature values of $E = 69$ GPa and $\nu = 0.33$. The glass is modeled with $E = 71.7$ GPa and $\nu = 0.17$, which are typical values for fused silica.

Figure 3.7(a) compares the undeformed sample chamber at ambient conditions (left) with the deformed sample chamber at increased interior pressure obtained from the finite-element calculations. Shown are perpendicular cuts parallel to the yz-plane through the center of the chamber window. The

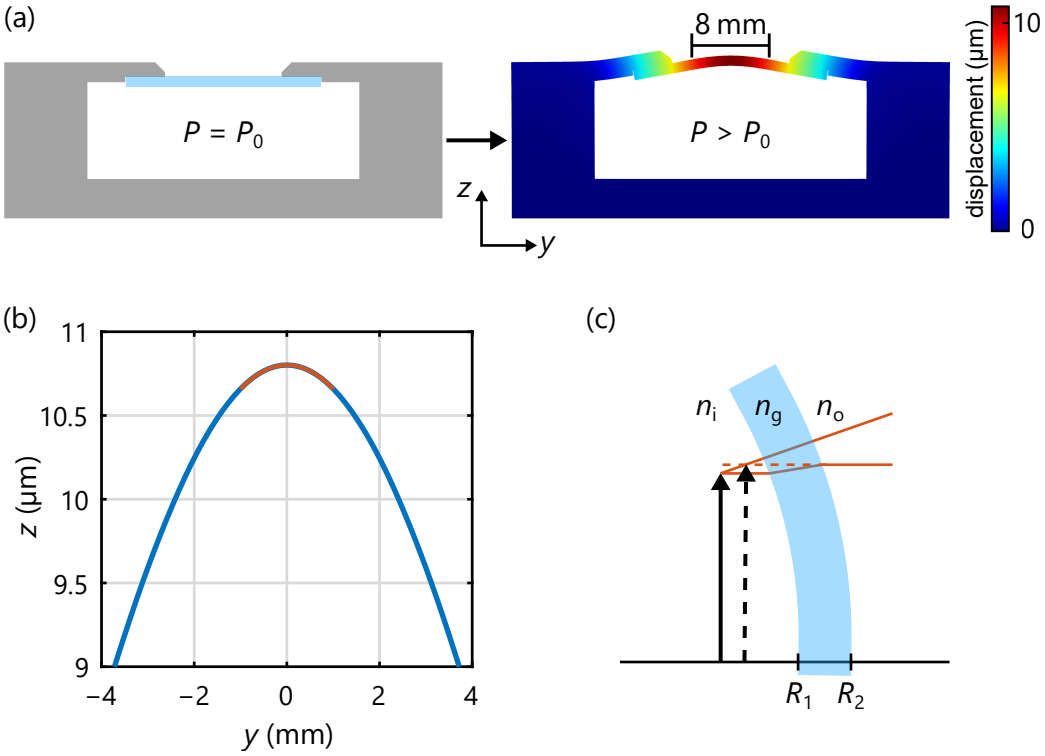

Figure 3.7: (a) Cut through the pressure chamber at ambient pressure $P = P_0 \approx 1\,\text{bar}$ (left) and a chamber overpressure of $\Delta P = 3.8\,\text{bar}$ (right). The modulus of the displacement vector plotted in a false color scale on the right. Deformations are largely exaggerated to show the outwards warping of the glass window. (b) shape of the top window surface along the y-direction through the center. The center part of $\pm 1\,\text{mm}$ is fitted with a parabola (red curve). (c) Qualitative beam paths, demonstrating how the window warping causes a magnification.

modulus of the displacement vector is plotted in a false color scale for the pressurized sample chamber and has a maximum of around 11 µm at the center of the window. A clear outward warping is observed. For visibility, all deformations have been largely exaggerated. A cut of the top surface of the deformed window is plotted in Figure 3.7(b) within a range of $\pm 4\,\text{mm}$ from the center. It corresponds to that part of the window marked by the 8 mm scale bar in panel (a). The center part ($\pm 1\,\text{mm}$) has been fitted with a quadratic function $a_0 + a_2 y^2$ (red curve) resulting in $a_2 = -1.420 \times 10^{-4}/\text{mm}$. The same evaluation for the cut through the bottom surface of the window (not depicted) gives a quadratic coefficient of $a_2' = -1.417 \times 10^{-4}/\text{mm}$. The curvatures are therefore $2a_2$ and $2a_2'$. The focal length f of the deformed

glass window with refractive index $n_g = 1.46$ and thickness $d = 1\,\mathrm{mm}$ can be calculated from the lensmaker's equation [76]

$$\frac{1}{f} = (n_g - 1)\left(2a_2' - 2a_2 + \frac{4(n_g - 1)da_2'a_2}{n_g}\right) . \tag{3.16}$$

As curvatures $2a_2$ and $2a_2'$ on top and bottom of the deformed window are almost identical, a very long focal length of $f = 3.5\,\mathrm{km}$ is obtained. Within the size of our measurement setup, the warping has, therefore, not introduced an additional lens. Instead of focusing parallel beams, it causes parallel displacement away from the center. This results in a magnified virtual image of a sample inside the chamber, as demonstrated qualitatively in Figure 3.7(c).

We have calculated this magnification via ray transfer matrix analysis assuming a distance of 1 mm between sample and glass window, which is equal to the window thickness d, a refractive index of $n_i = 1 + 14 \times 10^{-4}$ inside the chamber (air at 4.8 bar), and a refractive index of $n_o = 1 + 2.92 \times 10^{-4}$ outside (air at 1 bar). The propagation of a ray through the chamber window is described with matrices T_1 and T_2 for propagation inside the chamber and within the glass, respectively, R_1 for refraction at the inner glass surface and R_2 for refraction at the outer glass surface.

$$T_1 = T_2 = \begin{pmatrix} 1 & d \\ 0 & 1 \end{pmatrix} \qquad R_1 = \begin{pmatrix} 1 & 0 \\ \frac{n_i - n_g}{2a_2' n_g} & \frac{n_i}{n_g} \end{pmatrix} \qquad R_2 = \begin{pmatrix} 1 & 0 \\ \frac{n_g - n_o}{2a_2 n_o} & \frac{n_g}{n_o} \end{pmatrix} \tag{3.17}$$

Now we use the distance r_2 of a parallel beam outside the chamber and the equation

$$\begin{pmatrix} r_2 \\ 0 \end{pmatrix} = R_2 T_2 R_1 T_1 \begin{pmatrix} r_1 \\ \phi \end{pmatrix} \tag{3.18}$$

and calculate a magnification of $r_2/r_1 = 1 + 0.90 \times 10^{-4}$ or a relative length change of $(r_2 - r_1)/r_1 = 0.90 \times 10^{-4}$ at $\Delta P = 3.8\,\mathrm{bar}$. At $\Delta P = 0\,\mathrm{bar}$ the relative length change calculated from ray transfer matrix analysis is zero. In between the (small) displacement of the window is assumed to be proportional to ΔP [88], and hence also its curvature and magnification are proportional to ΔP.

The resulting $\Delta L/L$ obtained from ray transfer matrix analysis is plotted as a black line in Figure 3.8. It fits well with the measured $\Delta L/L$ of copper (blue points).

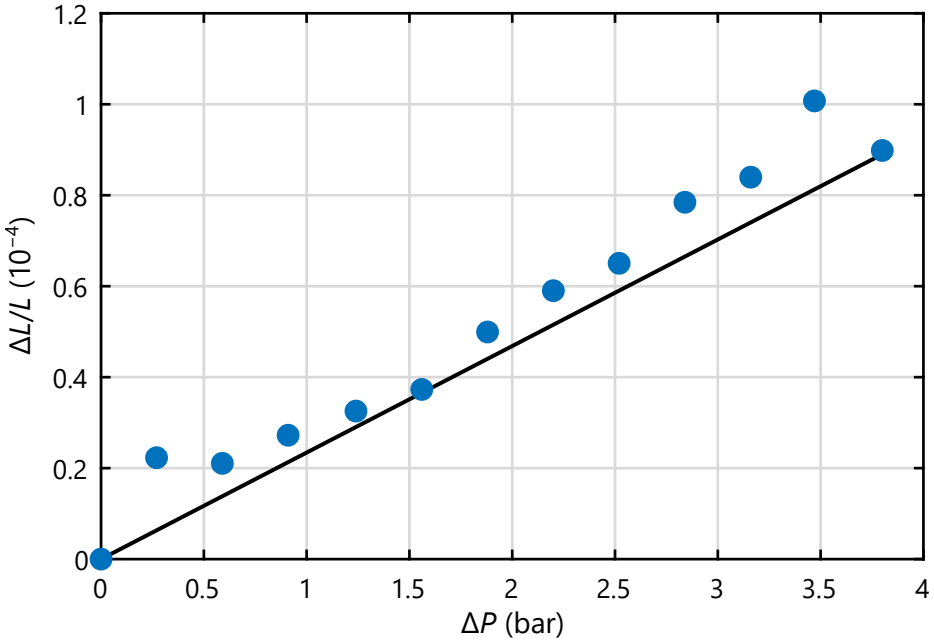

Figure 3.8: Apparent linear increase of $\Delta L/L$ of a copper piece measured under increased hydrostatic pressure, caused by outwards warping of the glass window (see Figure 3.7(a)). The magnitude of this optical artifact has been quantified with finite element simulations and ray transfer matrix analysis (black line).

In the next chapter, I will apply the methods introduced in this chapter to fabricate and measure micro-structured metamaterial samples. We will see that the systematic errors due to window warping are negligible, as these metamaterial samples show relative length changes that are at least two orders of magnitudes larger in absolute value.

Chapter 4
4 Results

This chapter is split into two sections. I will first present the results on thermoelastic metamaterials that can have negative, large positive, near zero or anisotropic effective thermal expansion, and then continue with poroelastic metamaterials with very large negative or positive effective compressibility with absolute values of up to five percent for one bar pressure increase. At the beginning of each section, I will introduce and explain the unit cell designs followed by numerical finite-element calculations including analysis of the dynamic behavior of our poroelastic metamaterials. In order to fabricate these designs, I have applied advanced DLW methods, that allow to realize fabrication of multi-component structures with only one photoresist and even to create sealed hollow volumes. I will perform cross-correlation analysis on the fabricated metamaterials which is used to determine temperature or pressure-induced length changes, and also to get insight into the operation principle. Finally, I will show measurements of the poroelastic metamaterials over time, demonstrating that the hollow volumes are sufficiently airtight.

4.1 Thermoelastic Metamaterials

In Section 2.2.3 it was shown that thermal expansion connects the elastic properties with the thermal properties of a material. In most applications, in which thermal expansion is dealt with, it is an unwanted effect, since the volume change can lead to cracks and failure. Bridges and railroad tracks have expansion joints as a countermeasure for the positive thermal expansion coefficients. Other applications employ materials with very low thermal expansion coefficients like the nickel–iron alloy Invar for shadow masks of CRT monitors. In this context, materials with negative thermal expansion coefficients have important applications. They can be employed to counteract a positive thermal expansion coefficient of a different material,

resulting in a near zero thermal expansion coefficient of the composite. The glass ceramic ZERODUR® [89] consists of a partially crystalline phase with a negative thermal expansion coefficient due to RUMs (see Section 2.3.2) and an amorphous phase with positive thermal expansion coefficient that cancel each other out. It is used for telescope mirrors (e.g. at the Very Large Telescope) and cooking tops (known under the name CERAN®).

Materials with near zero or negative thermal expansion are very rare and the existing ones may be unsuitable for new potential applications. This makes the possibility to obtain negative thermal expansion using a metamaterial very attractive. Negative thermal expansion would then be a result of the unit cell structure and all other desired material properties would be obtained from the constituent materials. For example, metals could be used as constituents if good electrical conductivity is required.

As we have mentioned in Section 2.1.4, all thermal expansion coefficients stated in this section are thermal *length*-expansion coefficients, which correspond to individual elements of the thermal expansion tensor. We have seen in Section 2.2.3 that the thermal expansion tensor of an isotropic material is proportional to the identity matrix. Under uniform temperature changes, the volume change is isotropic. As a result, a structure build from isotropic constituents with equal thermal expansion coefficient, will also have an effective thermal expansion coefficient equal to its constituents. Therefore, a metamaterial needs to be made of constituents with at least two different thermal expansion coefficients and voids, to allow us to tailor its effective thermal expansion coefficient.

In what follows, I will experimentally demonstrate tailored thermal expansion of a two-component metamaterial made by constituents of unequal thermal expansion coefficients. Despite having constituents with positive and isotropic thermal expansion coefficients, the effective thermal expansion coefficient of the metamaterials range from positive value exceeding that of any of the constituents, over zero, to even negative or anisotropic values.

4.1.1 Metamaterial Designs

Our main approach is based on a theoretical two-dimensional design by Gatt and Grima [64], that can be expanded into a three-dimensional structure [44]. It uses the mechanism of bending bilayer beams described in Section 2.3.2.

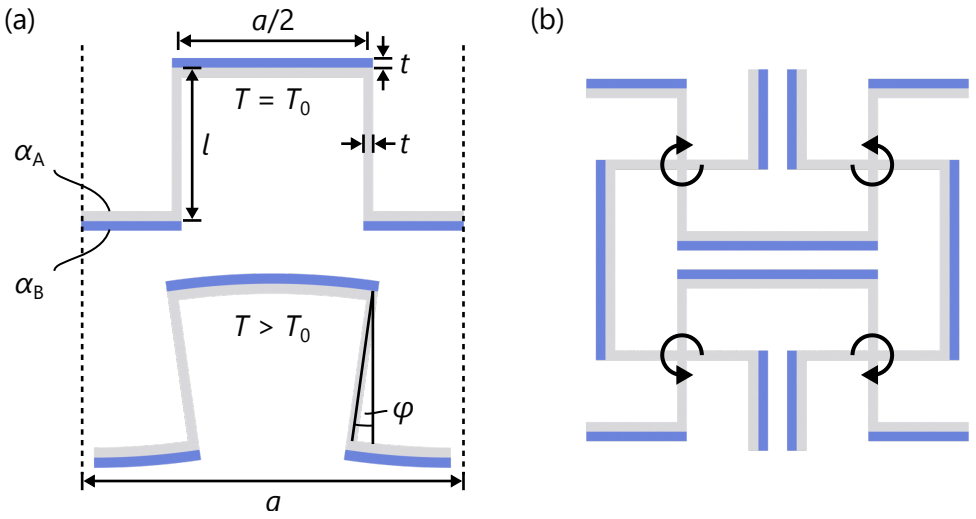

Figure 4.1: (a) Operation principle of one basic element with length a used to obtain negative thermal expansion. Two lever arms with length l are separated in distance of $a/2$. They are connected with bilayer beams with layer thickness t. Two constituent materials A (gray) and B (blue) have different thermal expansion coefficients of α_A and α_B, respectively. At increased ambient temperature, the bilayer beams bend and the lever arms convert the bending into a rotation (with angle φ), resulting in a decrease in length. (b) Four basic elements are arranged into a two-dimensional planar structure. The lever arms are now crosses. At increased temperature they rotate clockwise and anticlockwise in a checkerboard manner, which causes a shrinkage in 2D. Adapted from Reference [46].

Basic Mechanism

The mechanism is illustrated in Figure 4.1(a) with all relevant geometrical parameters indicated. One basic element consists of two constituent materials, which we will call component A (shown in gray) and component B (shown in blue). The thermal expansion coefficients of the components are α_A and $\alpha_B > \alpha_A$, both are assumed to be positive. The basic element can be decomposed into bilayer beams and lever arms. Within linear approximation, a small temperature increase ΔT will increase the length of the bilayer beams with a mean thermal expansion coefficient of $\langle\alpha\rangle$, that lies between α_A and α_B. Due to a finite difference of the thermal expansion coefficients, the bilayer beams will bend in addition, causing a rotation of the lever arms by an angle

φ, that can be calculated using Equation 2.95

$$\varphi = \frac{a/4}{r} = \frac{(\alpha_B - \alpha_A)\Delta T}{4} \frac{a}{t} \frac{12}{14 + \frac{E_A}{E_B} + \frac{E_B}{E_A}} . \tag{4.1}$$

The rotation angle decreases the length of one element by $2l \sin(\varphi)$. This geometrical length decrease can be described with a negative thermal expansion coefficient

$$\alpha_{geom} = -\frac{2l \sin(\varphi)}{a\Delta T} . \tag{4.2}$$

Inserting Equation 4.1 under linear approximation gives

$$\alpha_{geom} = (\alpha_A - \alpha_B) \frac{l}{t} \frac{6}{14 + \frac{E_A}{E_B} + \frac{E_B}{E_A}} . \tag{4.3}$$

The resulting effective thermal expansion coefficient, which is an effective metamaterial property, can be expressed as the sum of the mean thermal expansion coefficient $\langle \alpha \rangle$ of the constituents and the geometrical contribution described with α_{geom},

$$\alpha_{eff} = \langle \alpha \rangle + \alpha_{geom} = \langle \alpha \rangle + (\alpha_A - \alpha_B) \frac{l}{t} \frac{6}{14 + \frac{E_A}{E_B} + \frac{E_B}{E_A}} . \tag{4.4}$$

To obtain a negative effective thermal expansion coefficient, the mean thermal expansion coefficient has to be overcompensated by a negative geometrical contribution due to α_{geom}.

Three-Dimensional Unit Cells

Now, let us transition from the basic element towards a three-dimensional unit cell. Four basic elements are arranged into a two-dimensional unit cell [64] shown in Figure 4.1(b). Six of these planar structures, two parallel xy, xz and yz-planes, respectively, are stacked into a three-dimensional unit cell shown in Figure 4.2(a). Planar structures parallel to the xy-plane are highlighted in Figure 4.2(b). The geometrical parameters are listed in Table 4.1. All parameters were chosen with respect to the lattice constant a. Since we only consider relative length changes in the static regime, the effective thermal expansion coefficient of the unit cell is independent of a.

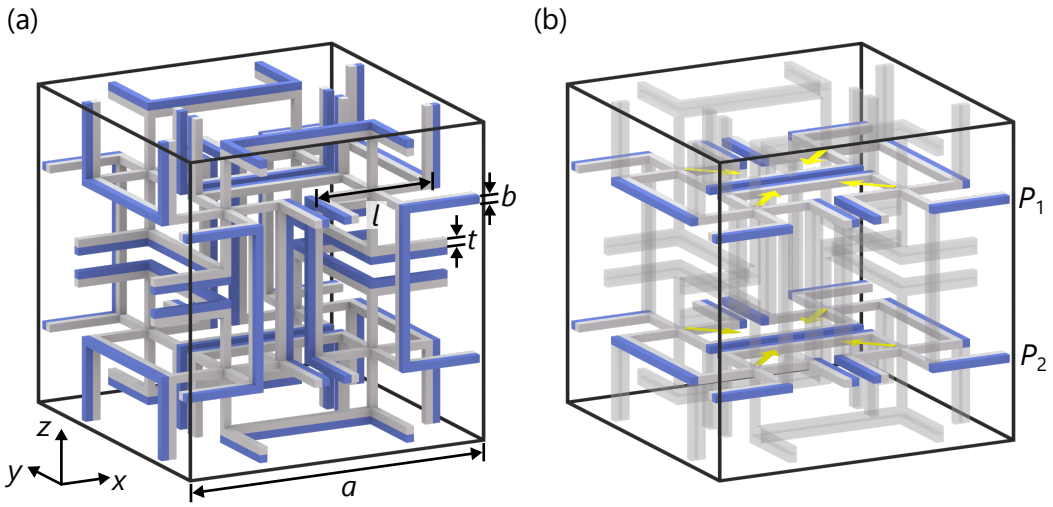

Figure 4.2: (a) Blueprint of a two-component unit cell that can be decomposed into the basic elements shown in Figure 4.1. It is assembled onto a simple cubic translational lattice with lattice constant a. Geometrical parameters are stated in Table 4.1. (b) Same unit cell as in (a), but with two planes P_1 and P_2 parallel to the xy-plane highlighted. These planes go through the centers of the three-dimensional crosses and correspond to the planes that are imaged in the measurements. At increased temperature, the bending beams rotate crosses within each plane, moving their centers inwards (illustrated by yellow arrows), resulting in a negative effective thermal expansion coefficient. Adapted from Reference [46].

In three dimensions, the lever arms of the basic element shown in Figure 4.1 become three-dimensional crosses (eight in each unit cell), and the beams now have a finite width b. The unit cell has three mirror planes going through its center and parallel to the xy, xz, and yz-planes, respectively. They cut the unit cell into eight centrosymmetric parts, each consisting of one three-dimensional cross and attached beams (also see Figure 4.4(b)). The unit cell is, therefore, not the primitive unit cell (see Appendix B), it is, however, much more suitable for description.

The operation principle of the three-dimensional unit cell is the same as for the basic element: At increased temperature, the bilayer beams bend and rotate the connecting crosses, which moves their centers inwards. For a negative effective thermal expansion coefficient, the rotation must overcompensate the positive mean thermal expansion coefficient of the beams.

Parameter	Value	Description
a	100 µm	lattice constant
b/a	2.5 %	width of beam relative to a
t/a	2.5 %	thickness of each layer relative to a
l/a	40 %	length of cross or lever arm relative to a

Table 4.1: Standard geometrical parameters used for modeling and numerical calculations of the thermoelastic metamaterials in this section, unless stated otherwise.

If the components A and B in each beam are exchanged, the geometrical effect is reversed. Instead of negative effective thermal expansion, the result would be a positive effective thermal expansion coefficient, that is much larger than that of each component. A blueprint for such a unit cell is shown in Figure 4.3(a).

Exchanging the constituent materials A and B only for those beams responsible for the length change along one direction, for instance, the y-axis seems to lead to a highly anisotropic thermal expansion tensor at first glance. However, the effects would cancel out in the current design. For example, an arrangement with a negative thermal expansion coefficient along the x-axis and a large positive thermal expansion coefficient along the y-axis would require each cross to simultaneously perform opposite counteracting rotations around the z-axis. The rotations couple of the length changes of different axes, which means that compressing the unit cell along one axis also compresses it along the orthogonal axes. This is the reason the negative Poisson's ratio of the unit cell is negative. We have calculated a value of -0.41 with COMSOL Multiphysics.

To solve this dilemma, only two basic elements with the same orientation are arranged in each plane. In the plane depicted in Figure 4.1(b), for example, only the vertically oriented elements are kept. In two dimensions, both remaining elements would be disconnected. Fortunately, in the three-dimensional arrangement, all the elements are still connected, as it can be seen in Figure 4.3(b). Each plane now only contains basic elements for length changes along one of the three principal axes and the thermal expansion coefficients along each axis can be independently tailored. The almost completely decoupled axes in regard to length changes results in a near zero Poisson's ratio of $\nu = 3 \times 10^{-5}$.

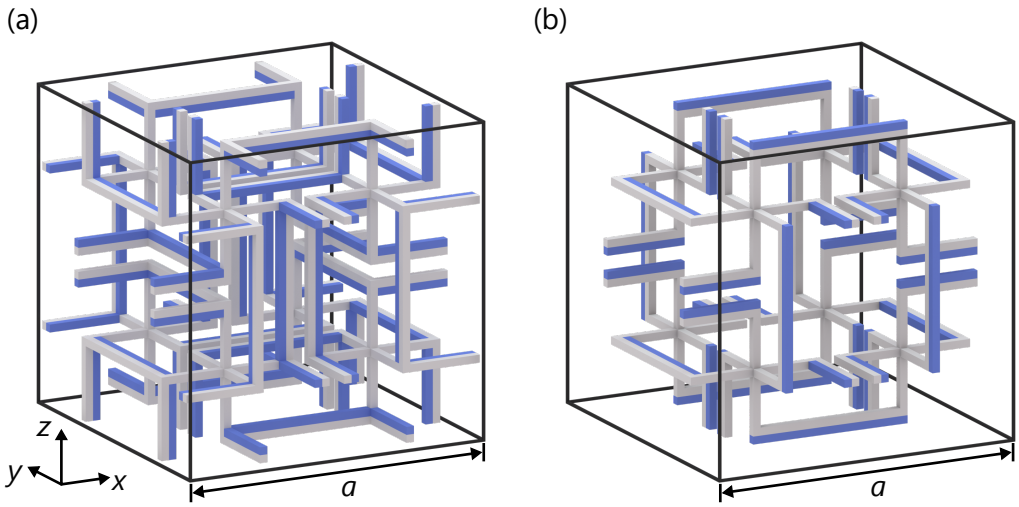

Figure 4.3: (a) Same blueprint as in Figure 4.2(a), but with constituents A (blue) and B (gray) exchanged in each beam. This unit cell has a large positive thermal expansion coefficient. (b) Unit cell for anisotropic thermal expansion with a negative thermal expansion coefficient along x and z-axes and a large positive thermal expansion coefficient along the y-axis.

4.1.2 Numerical Calculations

In order to better understand the three-dimensional behavior of our unit cells and to optimize geometrical parameters, we have analyzed them numerically with a COMSOL Multiphysics (see Section 3.2). In the following numerical calculations, unless stated otherwise, component A (gray) and B (blue) are modeled as elastic materials with thermal expansion coefficients of $\alpha_A = 4 \times 10^{-5}\,\mathrm{K}^{-1}$ and $\alpha_B = 6 \times 10^{-5}\,\mathrm{K}^{-1}$, Young's moduli of $E_A = 4\,\mathrm{GPa}$ and $E_B = 3\,\mathrm{GPa}$, and a Poisson's ratio of $\nu = 0.4$.

Figure 4.4(a) visualizes calculated temperature induced deformations of the unit cell shown in Figure 4.2(a) assuming periodic boundary conditions along the x, y, and z-directions. Figure 4.4(b) depicts the complex three-dimensional rotation of one cross leading to an inward movement of its center towards the center of the unit cell. The resulting effective thermal expansion coefficient is calculated to be $\alpha_{\mathrm{eff}} = -5.168 \times 10^{-5}\,\mathrm{K}^{-1}$.

If $\alpha_B = \alpha_A = 4 \times 10^{-5}\,\mathrm{K}^{-1}$ is assumed instead, the effective thermal expansion coefficient would be equal to both components, and hence positive. This implies that for continuity reasons, α_{eff} has to be zero for a certain

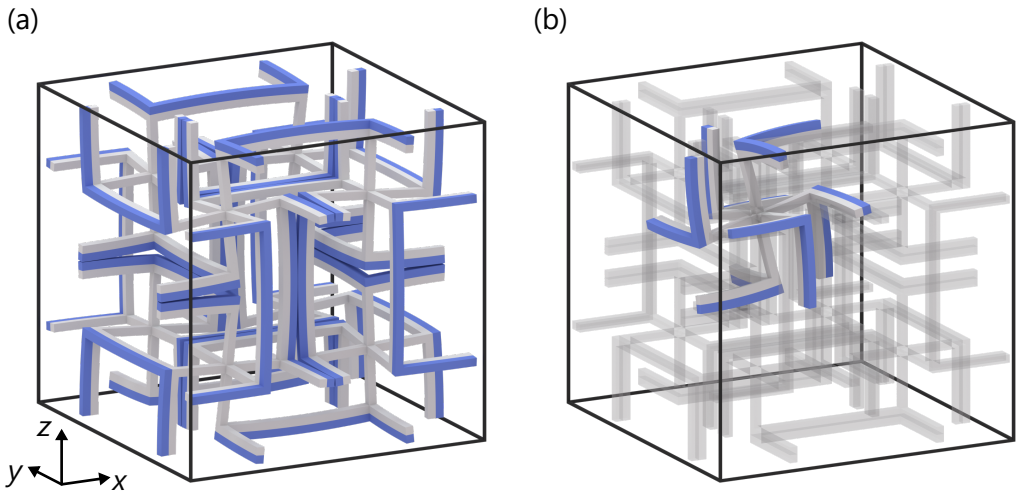

Figure 4.4: (a) Calculated deformed unit cell from Figure 4.2 under increased temperature showing an overall volume decrease. A negative effective thermal expansion coefficient of $\alpha_{\text{eff}} = -5.168 \times 10^{-5}\,\text{K}^{-1}$ is derived. For visualization, deformations have been largely exaggerated. (b) One eighth of the calculated deformed unit cell (slightly more exaggerated compared to (a)) containing one three-dimensional cross and bilayer beams is highlighted. It visualizes the complex rotations in three dimensions that leads to volume decrease. The underlying semi-transparent gray structure corresponds to the undeformed state of the unit cell. Material parameters are: $\alpha_{\text{A}} = 4 \times 10^{-5}\,\text{K}^{-1}$, $\alpha_{\text{B}} = 6 \times 10^{-5}\,\text{K}^{-1}$, $E_{\text{A}} = 4\,\text{GPa}$, $E_{\text{B}} = 3\,\text{GPa}$, and $\nu = 0.4$. Adapted from Reference [46].

intermediate value of α_{B}. This is shown in Figure 4.5, where the calculated effective thermal expansion coefficient is plotted as a function of α_{B}. As expected from Equation 4.4, α_{eff} decreases linearly with increasing α_{B}. The sign change happens at $\alpha_{\text{B}} \approx 5 \times 10^{-5}\,\text{K}^{-1}$, at a ratio of $\alpha_{\text{B}}/\alpha_{\text{A}} \approx 1.2$. The same numerical calculation was repeated for two additional ratios of $E_{\text{A}}/E_{\text{B}}$ (shown in red and yellow) while the Young's modulus of component A was fixed at $E_{\text{A}} = 4\,\text{GPa}$. Even at a ratio of $E_{\text{A}}/E_{\text{B}} = 4$, the influence of the Young's moduli is rather small, as expected from Equation 4.4.

For comparison, we have also performed numerical calculations on corresponding three-dimensional models of a basic element and a plane illustrated in Figure 4.1 with periodic boundary conditions along one and two dimensions, respectively. The three-dimensional models were obtained by extruding them by $b = 0.1\,\%\,a$ into the third dimension. Material parameters

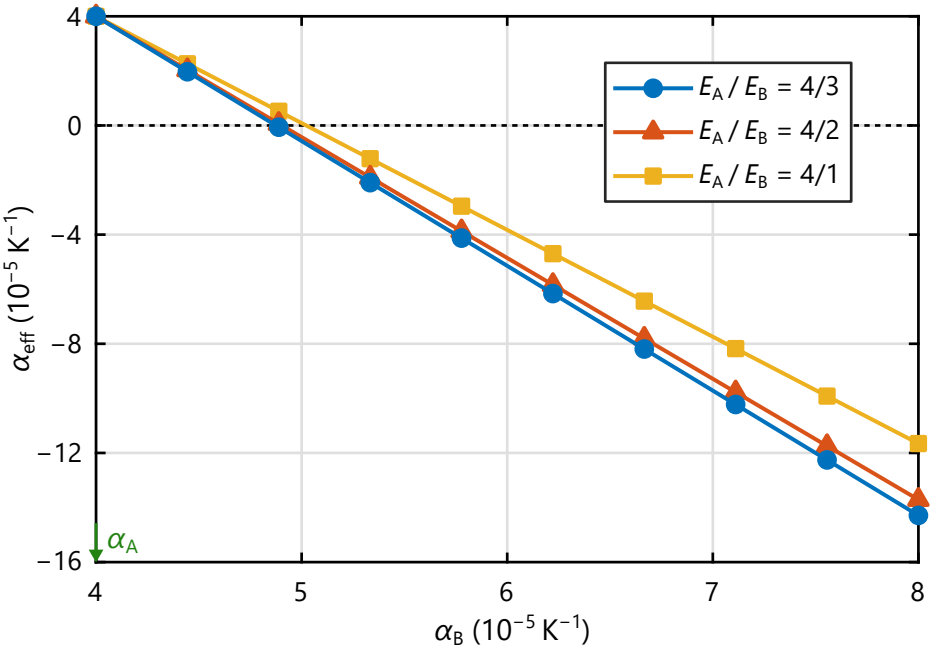

Figure 4.5: Calculated effective thermal expansion coefficient α_{eff} of the unit cell shown in Figure 4.2 for different thermal expansion coefficients of component B, α_{B}, and a constant thermal expansion coefficient of component A, $\alpha_{\mathrm{A}} = 4 \times 10^{-5}\,\mathrm{K}^{-1}$ (indicated by the green arrow). Different colors correspond to different Young's moduli ratios $E_{\mathrm{A}}/E_{\mathrm{B}}$ of the components (see legend) with a fixed value $E_{\mathrm{A}} = 4\,\mathrm{GPa}$. A sign change of α_{eff} happens at $\alpha_{\mathrm{B}} \approx 5 \times 10^{-5}\,\mathrm{K}^{-1}$. Adapted from Reference [46].

are the same as in Figure 4.4. An effective thermal expansion coefficient of $\alpha_{1\mathrm{D}} = -6.768 \times 10^{-5}\,\mathrm{K}^{-1}$ was obtained for the basic element and an almost identical thermal expansion coefficient of $\alpha_{2\mathrm{D}} = -6.768 \times 10^{-5}\,\mathrm{K}^{-1}$ was obtained for the plane, since at each cross, both connected basic elements perform a rotation in the same direction and with the same magnitude. The individual rotations, therefore, do not influence each other within a plane. Compared to the result for the three-dimensional unit cell, $\alpha_{1\mathrm{D}}$ and $\alpha_{2\mathrm{D}}$ are about 30 % larger. The reason will be explained in the next part.

Comparison with Analytical Solution

In Equation 4.4 we have derived an analytical expression for the thermal expansion coefficient of one basic element shown in Figure 4.1(a). With

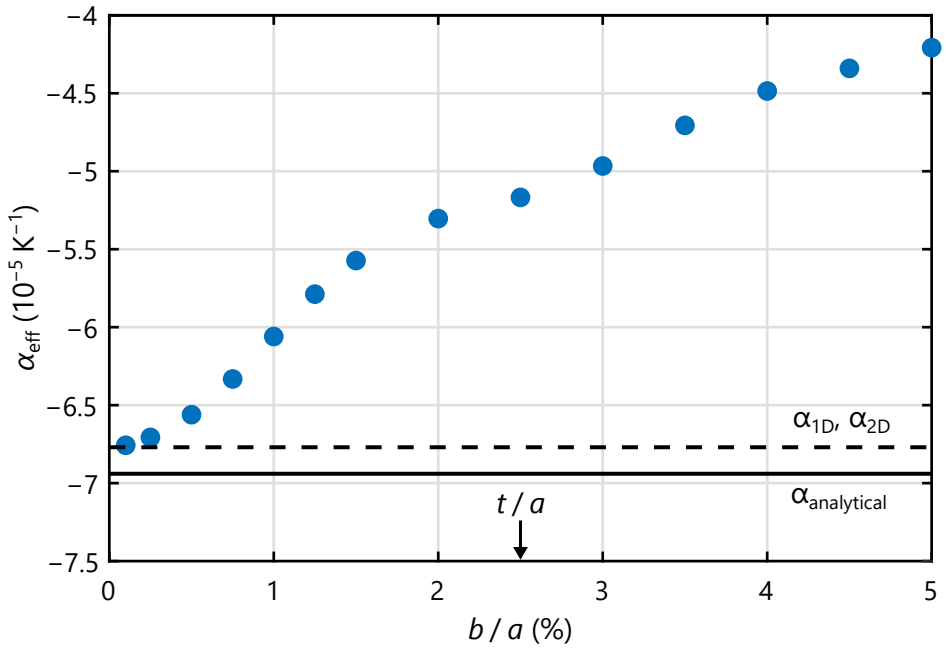

Figure 4.6: (a) Calculated effective thermal expansion coefficient α_{eff} of the unit cell shown in Figure 4.2 with respect to the beam width b/a. The small arrow refers to the layer thickness t/a. For comparison, the effective thermal expansion coefficient obtained by the analytical expression from Equation 4.4 is plotted as a solid line. The dashed line corresponds to the numerically calculated values $\alpha_{1D} \approx \alpha_{2D}$ for the basic element and the planar structure. For small values of b, α_{eff} approaches the dashed line.

the same geometrical material parameters as for the numerical calculations and the approximation $\langle\alpha\rangle \approx (\alpha_A + \alpha_B)/2$, we obtain an effective thermal expansion coefficient of $\alpha_{analytical} = -6.938 \times 10^{-5}\,K^{-1}$. With a relative deviation of 2.5 %, it fits nicely with the numerical results for both the basic element and the two-dimensional arrangement. The small difference could be caused by the influence of the attached lever arms, or by a deviation from the initial assumption of long and thin bilayer beams for Equation 2.95.

In the three-dimensional unit cell, however, each cross has to perform rotations around each cubic axis simultaneously. A rotation of a cross around the z-axis, for example, will also lead to additional bending of the beams connected on the top and bottom orthogonal to the bending direction causing the rotations. This reduces the magnitude of the rotations and

explains the difference in thermal expansion ($\alpha_{\text{eff}} = -5.168 \times 10^{-5}\,\text{K}^{-1}$). For $b/t \ll 1$, the additional bending can be performed much easier than the bending causing the rotations and one may assume that the thermal expansion coefficient of the unit cell converges to the thermal expansion coefficient of one basic element for $b/t \to 0$. To test this hypothesis, we have performed a numerical sweep for different values of b, and otherwise same standard parameters as used before.

The results are plotted in Figure 4.6. As predicted, the modulus of the effective thermal expansion coefficientincreases for falling b and approaches the numerically obtained values for the basic element and the planar structure (shown as dashed lines) for $b/t \ll 1$. The solid line near the dashed lines corresponds to the analytically obtained value. The same convergence behavior has been also confirmed for another set of parameters ($l/a = 30\,\%$, $t/a = 2\,\%$, $\alpha_{\text{A}} = 1 \times 10^{-5}\,\text{K}^{-1}$, $\alpha_{\text{B}} = 3 \times 10^{-5}\,\text{K}^{-1}$, $E_{\text{A}} = 3\,\text{GPa}$, $E_{\text{B}} = 1\,\text{GPa}$, and $\nu = 0.4$).

To investigate whether the linear dependence of the effective thermal expansion coefficient on l and $1/t$ from Equation 4.4 is also valid for the three-dimensional unit cell, we have additionally performed numerical sweeps for parameters l and t. The linear dependence of α on l is confirmed in Figure 4.7(a). In Figure 4.7(b), numerically obtained values for α are plotted over a/t. For a fixed value of $b/a = 2.5\,\%$ (blue points), an additional contribution due to a change in cross-section aspect ratio b/t, as we have seen before, causes a deviation from linearity. For fixed aspect ratios, here as $b/t = 1$ (red points), the linear dependence on $1/t$ is regained.

To conclude the numerical analysis, we can say that in order to obtain a large metamaterial effect, l/a has to be chosen as large as possible, while b/a and t/a have to be chosen as small as possible. We have also shown that the effective thermal expansion of the metamaterial can be tuned from positive, over zero, to negative values just by changing the thermal expansion coefficient of one constituent material within a small and positive range.

4.1.3 Gray-Tone Laser Lithography

Our micro-structured two-component metamaterial samples are fabricated by means of DLW, as described in the previous chapter. The numerical calculations have shown that for our current design of a negative thermal expansion metamaterial (Figure 4.1 and Table 4.1) a negative sign is obtained,

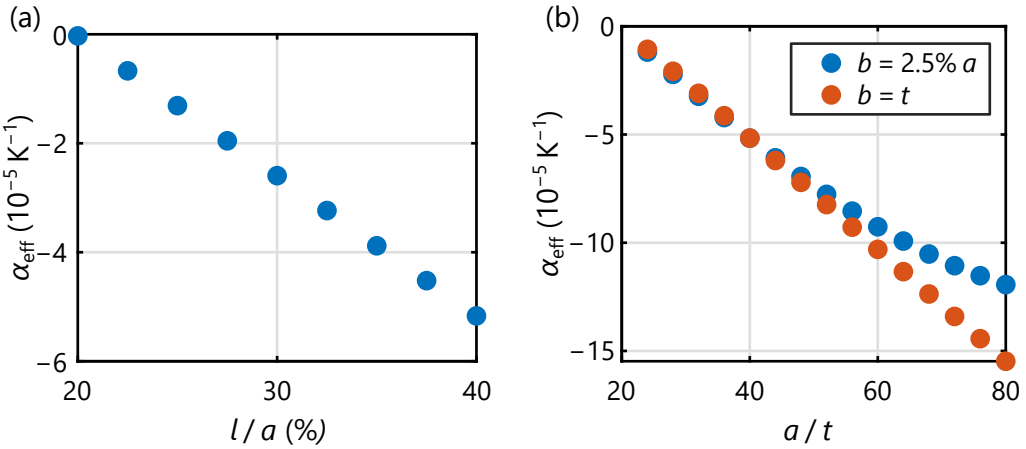

Figure 4.7: Calculated effective thermal expansion coefficient α_{eff} of the unit cell introduced in Figure 4.2 with respect to the relative cross length l/a, showing a linear dependence, and (b) with respect to the inverse layer thickness a/t. The blue points in (b), for which the beam width was fixed to $b/a = 2.5\,\%$, deviate from linearity. However, the red points, for which beam width and layer thickness are equal show a linear trend.

if the thermal expansion coefficients of the constituent materials have a ratio of at least 1.2. This can, for example, be realized using different photoresists for each component. However, this would involve a difficult multi-step process, which could render fabrication of large samples almost impossible with current technology. In our favor, we have found out that the thermal expansion coefficient of a structure written with the IP-Dip photoresist depends on the exposure dose. Just like a conventional printer can print different grayscale shades from one cartridge, we are able to employ gray-tone laser lithography [46], using the exposure power as a parameter, to 3D print different thermal expansion coefficients from only one photoresist.

Thermal Expansion Coefficients of Polymerized IP-Dip

In Figure 4.8(a), the thermal expansion coefficients of polymer cubes written with IP-Dip with dimensions of 100 µm × 100 µm × 100 µm are plotted against the exposure laser power. We have chosen a slicing distance of 500 nm, a hatching distance of 200 nm and a scan speed of 20 mm/s. To measure the thermal expansion coefficient, each polymer cube was heated from room temperature at $T_0 = 23\,^{\circ}\text{C}$ to about $T_0 + \Delta T = T_0 + 20\,\text{K}$ and subsequently cooled to room temperature again. Images were taken during

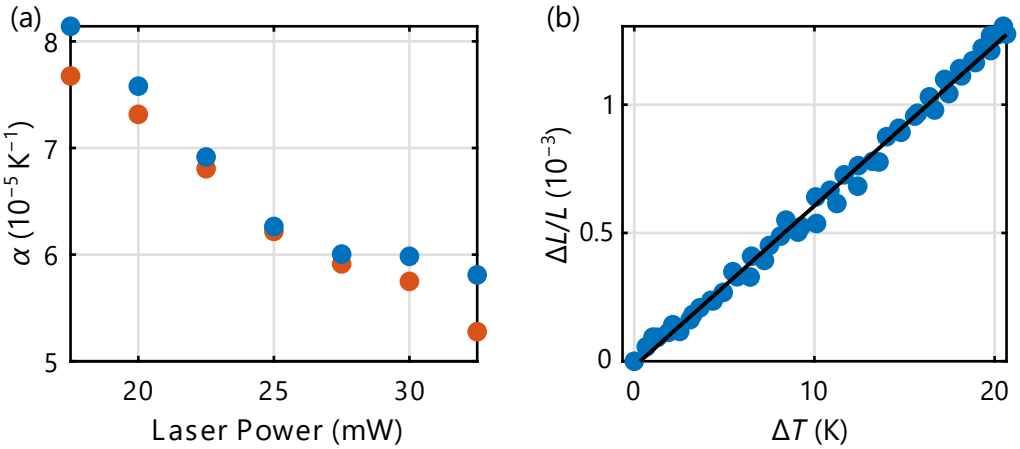

Figure 4.8: (a) Thermal expansion coefficients of 100 µm × 100 µm × 100 µm polymer cubes written with IP-Dip using different exposure laser powers. Blue and red points correspond to different sample series. (b) Measured relative length-change with respect to temperature increase of a cube written with a laser power of 25 mW (blue point in (a)). The slope of the linear fit (black line) determines the thermal expansion coefficient. Adapted from Reference [46].

this process and the relative length changes with respect to the image taken at T_0 were calculated via image cross-correlation (see Section 3.3.3) and plotted over ΔT. This is shown in Figure 4.8(b) for the cube fabricated with an exposure laser power of 25 mW (corresponds to the blue point at 25 mW) from Figure 4.8(a). The thermal expansion coefficient of the cube is obtained from the slope of the linear fit.

The different colors correspond to two different sets of samples. Apart from the smallest and largest exposure laser power the measured thermal expansion coefficients are very similar for both sets of sample. The deviations can be explained as follows: The smallest exposure laser power is near the polymerization threshold, where small changes of the exposure conditions have a large influence on the polymerized material, whereas at the largest exposure laser power, small explosions have already started to form spontaneously.

A clear decrease of the thermal expansion coefficient with respect to exposure laser power can be seen, from about $8 \times 10^{-5}\,\mathrm{K}^{-1}$ at low exposure laser powers down to about $5 \times 10^{-5}\,\mathrm{K}^{-1}$ at high exposure laser powers. We understand this behavior as a change in cross-linking density. Higher exposure powers are known to increase the cross-linking density inside the

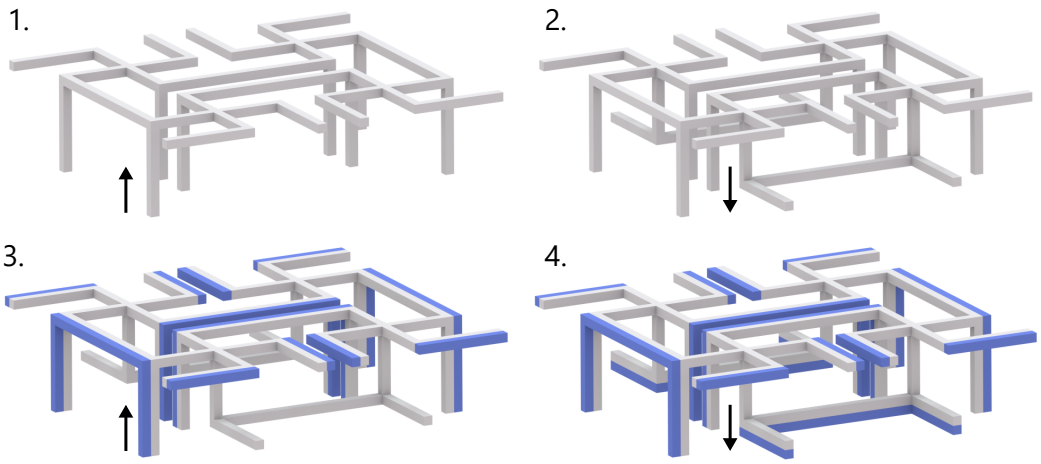

Figure 4.9: Writing strategy to avoid floating pieces. The arrow depicts the axial writing direction. Parts of the unit cell that are only connected on the top (2. and 4.) are written from top to bottom.

polymer [90, 91] and a higher cross-linking density tends to decrease thermal expansion [92, 93].

Fabrication

Metamaterials with negative effective thermal expansion were fabricated based on the design shown in Figure 4.2. Numerical calculations in Section 4.1.2 have demonstrated that large effects are obtained for large l/a and small b/a and t/a. We choose a fixed unit cell size of 100 µm and a minimum feature size of 2.5 µm, that can be comfortably and reproducibly fabricated with DLW. To avoid touching beams, the maximum cross length l/a was set to 40 %. As a result, we basically end up with the standard geometrical parameters listed in Table 4.1. These parameters are therefore our target parameters for fabrication. To correct for the aspect ratio of the voxel, that would lead to an increased thickness along the axial direction, all thicknesses in the axial direction have been reduced by 0.5 µm.

We have fabricated metamaterials composed of $4 \times 4 \times 2 = 32$ unit cells, stitched together from writing blocks with a size of $1.5a \times 1.5a \times 0.5a$. Stitching edges were moved away from the center of the beams by introducing an offset of $-0.23a$ in all directions. Each writing block was sliced with a distance of 500 nm and then hatched by parallel lines at a distance of

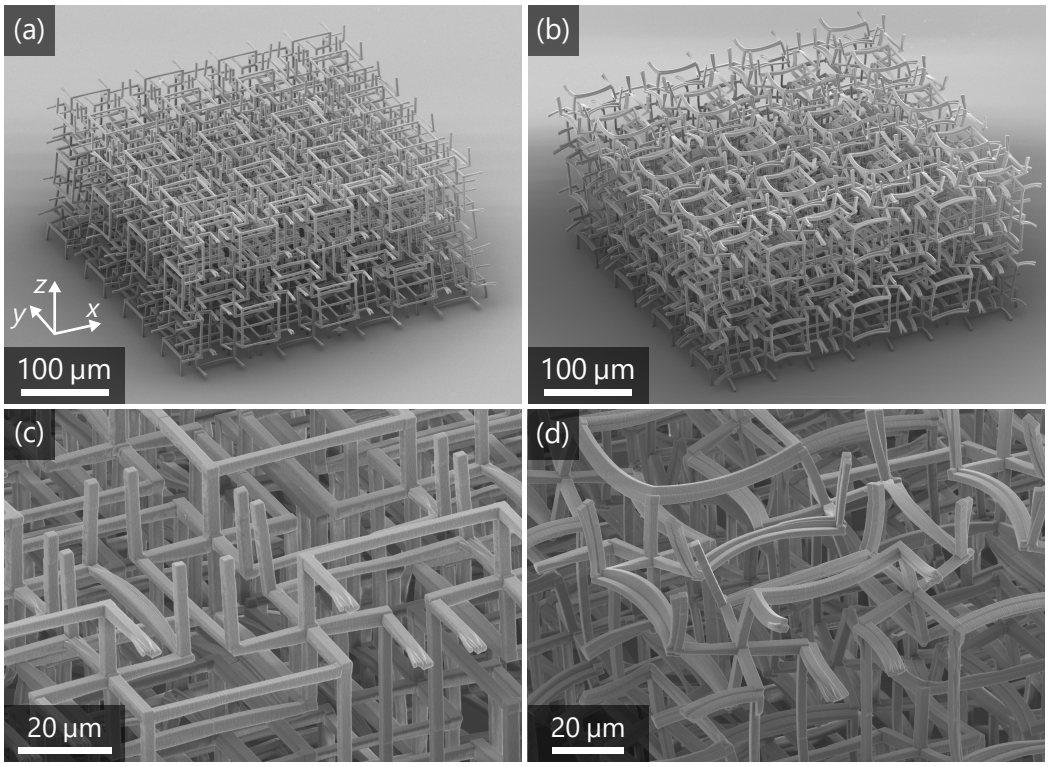

Figure 4.10: Scanning electron microscope pictures of fabricated metamaterial structures with $4 \times 4 \times 2$ unit cells following the blueprint depicted in Figure 4.2(a). (a) One-component control sample, where only the gray part of the sample shown in Figure 4.2(a) has been written. (b) Two-component sample with visible pre-bending of the beams compared to (a), due to different shrinkage of the two components during development. The metamaterial structure has reversed the shrinkage into an expansion of the sample compared to (a). This also confirms the operation principle of the metamaterial. (c) and (d) are magnified views of (a) and (b), respectively. Adapted from Reference [46].

200 nm. The average exposure power was set to 32.5 mW for component A and 19 mW for component B, both at a scan speed of 20 mm/s. Unconnected floating parts during fabrication were avoided by adapting the axial writing direction for different segments, as shown schematically for one unit cell in Figure 4.9.

Scanning electron microscope pictures of fabricated metamaterial structures are shown in Figure 4.10. The structure in Figure 4.10(a) is an one-component control sample, that only includes the gray component shown

in Figure 4.2(a). For the two-component structure in Figure 4.10(b), each component was written with a different exposure laser power. While the beams of the control sample are straight, as they are supposed to be, the beams of the two-component sample are visibly bent. The bending arises from different volume shrinkage of the components. A lower cross-linking density is connected with a larger thermal expansion coefficient as well as a higher shrinkage, as more residual monomer is washed away during development. Comparing Figure 4.10(a) and (b), this has resulted in an expansion (or negative shrinkage) of the two-component sample, confirming the operation principle of our metamaterial. It is basically the same behavior as negative swelling [94, 95], but under reversed experimental conditions.

Within the linear regime pre-bending does not change the principle of operation and is also unproblematic in the fabrication process of the negative thermal expansion metamaterial. However, if we change to the unit cell design of Figure 4.3(a) for large positive thermal expansion coefficients, where the constituents in each beam are exchanged, also the pre-bending will change in direction, resulting in large shrinkage. This leads to touching beams and a nullification of the metamaterial effect. Therefore, the shrinkage has to be compensated beforehand.

Using COMSOL Multiphysics we have calculated an expanded structure with $4 \times 4 \times 2$ unit-cells, with fixed constraints at the bottom and otherwise open boundaries for a large temperature change. The obtained deformed three-dimensional structure is shown in Figure 4.11 and is directly used as the model for fabrication with DLW. Shrinkage during development will ideally return it to its undeformed state with straight beams.

A temperature increase on the metamaterial with large positive effective thermal expansion bends the bilayer beams in the same direction as shrinkage during development does on the metamaterial with negative effective thermal expansion. As a result the structure shown in Figure 4.11 looks very similar to the fabricated metamaterial shown in Figure 4.10(b).

Due to the complexity of the structure, the slicing distance had to be decreased to 200 nm and the hatching line distance to 100 nm. To keep a similar exposure dose, a laser power of 24 mW was used for component A and 16 mW for component B, at the same scan speed of 20 mm/s. These are also the writing parameters for the metamaterials with an anisotropic thermal expansion (Figure 4.3(b)).

Scanning electron micrographs are shown in Figure 4.12. Panel (a) depicts

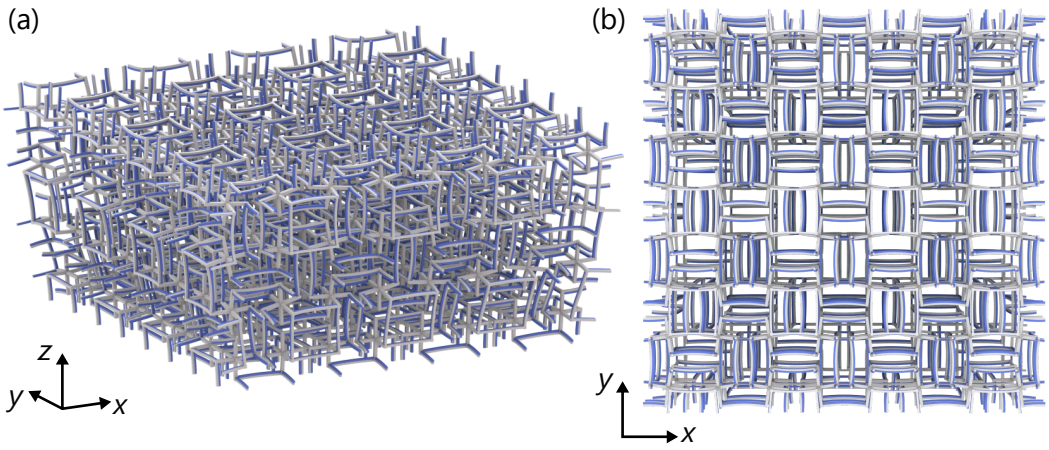

Figure 4.11: (a)Side view and (b) top view of the calculated deformed metamaterial structure consisting of $4 \times 4 \times 2$ unit cells designed for a large positive effective thermal expansion coefficient (Figure 4.3(a)) at a large temperature increase. The bottom is fixed in position and all other boundaries were modeled as open. This deformed structure is used as a model for fabrication and compensates the polymer shrinkage during development.

the metamaterial with with large positive thermal expansion fabricated in an expanded state with beams that are bent in the opposite direction as they do during development (see Figure 4.11). Notably, all beams are straight after fabrication (also see Figure 4.12(c)), indicating that the precompensation has been successful. Panel (b) shows a fabricated metamaterial designed for anisotropic thermal expansion, based on the unit cell shown in Figure 4.3.

4.1.4 Measurements

Fabricated metamaterial samples are measured using the setup described in Section 3.3. To minimize outgassing of the polymer, the samples are heated to 60 °C for one hour inside the chamber with the peltier element. Subsequently the chamber is flooded with dry nitrogen, sealed, and cooled back to room temperature ($T_0 = 23\,^{\circ}\mathrm{C}$). The camera image is focused on the upper xy-plane (P_1 in Figure 4.2(b)) of the top layer of unit cells.

Starting at room temperature, the chamber temperature is increased by $\Delta T = 10\,\mathrm{K}$ and afterwards by another 10 K ($\Delta T = 20\,\mathrm{K}$). At each of the three temperature points, we wait several hours, to be sure that micro-structure and sample chamber (where the temperature is measured), have the same

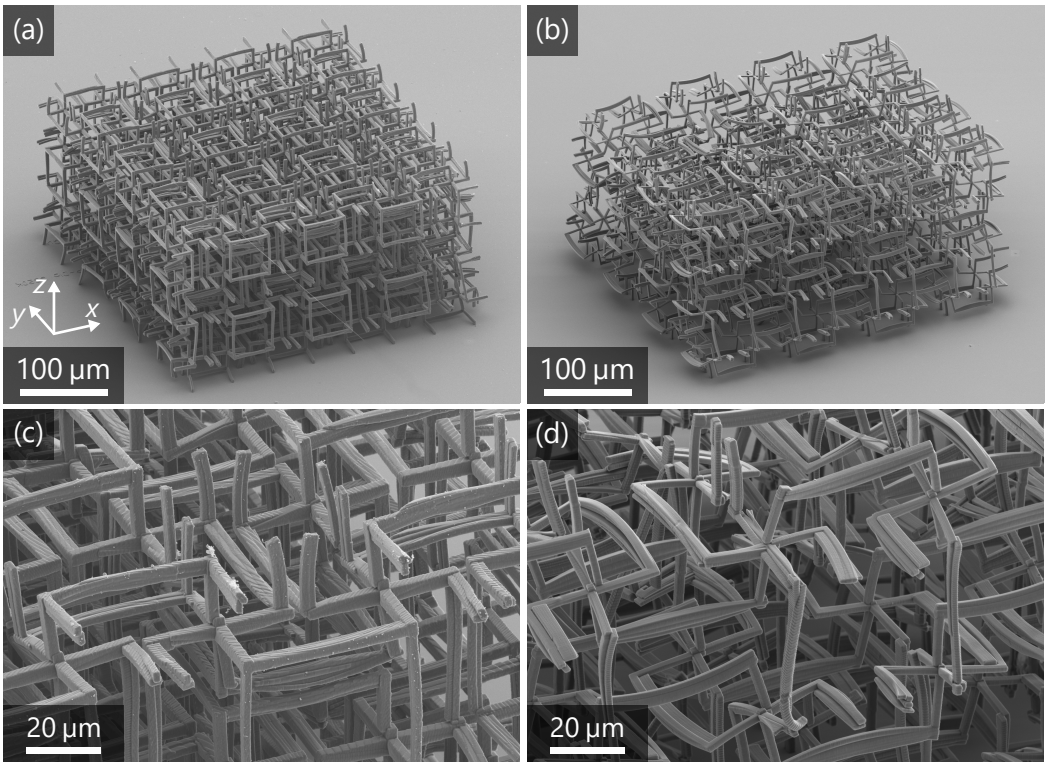

Figure 4.12: Scanning electron microscope pictures of fabricated metamaterial structures with $4 \times 4 \times 2$ unit cells. (a) Metamaterial structure designed for large positive thermal expansion, fabricated in using the precompensated model shown in Figure 4.11. The bilayer beams have been fabricated in a pre-bent state and have become straight again after development. (b) Metamaterial structure designed for anisotropic thermal expansion. (c) and (d) are magnified views of (a) and (b), respectively.

temperature. Afterwards, ten pictures are taken with the autofocus algorithm to compensate for any temperature induced defocussing (see Section 3.3.2). Additionally, lateral movement is tracked by means of image cross-correlation and most of it is compensated automatically during the measurement using the piezo stage.

After the images are taken, small individual ROIs of 33×33 pixels ($n_{\text{corr}} = 16$) are tracked with image cross-correlation (see Section 3.3.3) over all measurement images and their displacement vectors are calculated. This gives us the ability to determine the overall relative length change, as well as local deformations.

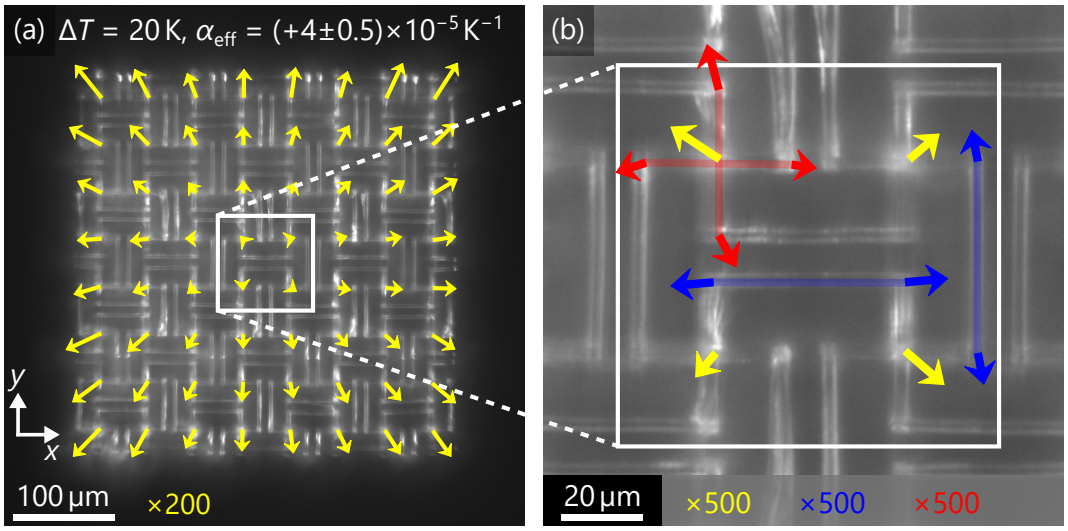

Figure 4.13: (a) Temperature induced displacement vector fields obtained by image cross-correlation and the underlying optical micrograph of an one-component control sample as shown in Figure 4.10. The sample consists of $4 \times 4 \times 2$ unit cells and was heated by $\Delta T = 20\,\mathrm{K}$. From the displacement vectors, a positive effective thermal expansion coefficient of $\alpha_{\mathrm{eff}} = (+4 \pm 0.5) \times 10^{-5}\,\mathrm{K}^{-1}$ is extracted. (b) Magnified view of (a). The arrows demonstrate a similar positive thermal expansion on the beams and crosses. All arrows have been scaled by the indicated factors. Adapted from Reference [46].

Negative Thermal Expansion

We begin with an one-component control sample based on the design shown in Figure 4.10(a), fabricated with an exposure laser power of 32.5 mW. Measured displacement vectors under a temperature increase of $\Delta T = 20\,\mathrm{K}$ are shown in Figure 4.13. All measured displacement vectors are averaged over the ten pictures taken and scaled by the indicated scaling factors. The yellow displacement vectors at the center of the crosses revealing roughly isotropic length changes, allowing us to calculate the effective thermal expansion coefficients analogous to the thermal expansion coefficient of copper (see Figure 3.6). As expected, all displacement arrows in Figure 4.13(a) point outwards. We obtain an positive effective thermal expansion coefficient of $\alpha_{\mathrm{eff}} = (+4 \pm 0.5) \times 10^{-5}\,\mathrm{K}^{-1}$ (the errors are estimated), which is caused by the positive thermal expansion coefficient of the polymer. The value is a little lower than the one measured on a cube with same exposure laser power in Figure 4.8. Obviously, exposure and polymerization conditions

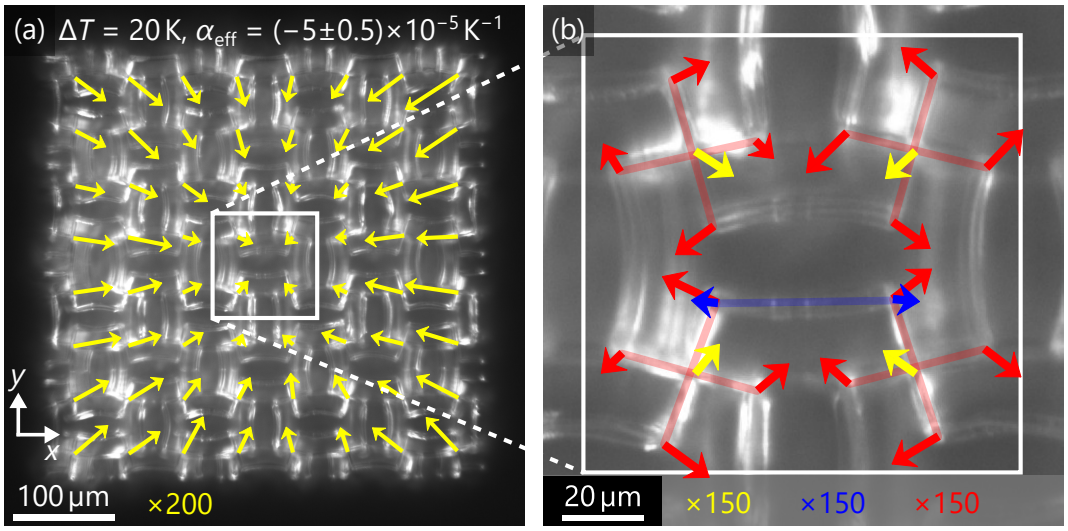

Figure 4.14: Same measurement as shown in Figure 4.13, but for the two-component sample. From the displacement vector field (a) a negative effective thermal expansion coefficient of $\alpha_{\text{eff}} = (-5 \pm 0.5) \times 10^{-5}\,\text{K}^{-1}$ is obtained. (b) Magnified view of (a) showing the mechanism within one unit cell. The positive expansion of the beams (blue arrows) are overcompensated by the rotation of the crosses (red arrows), resulting in an overall negative effective thermal expansion (yellow arrows). Adapted from Reference [46].

for a bulk cube and a porous structure with small feature sizes are not the same, even for equal exposure laser powers. In the magnified view shown in Figure 4.13(b), individual parts of one unit cell are measured. The behavior of one cross is highlighted by a set of four red arrows, sets of two blue arrows quantify the expansion of the beams and, just like before, the yellow arrows indicate the displacement of the cross centers. Within each set of arrows, the mean displacement vector is subtracted to only reveal the relative movement with respect to their mean position. The semitransparent lines are guides to the eye, connecting arrows that belong to the same set. As expected for the one-component material, each set of arrows shows the ordinary positive thermal expansion coefficient of the constituent material.

The two-component metamaterial shown in Figure 4.10(b) was fabricated with exposure laser powers of 32.5 mW and 19 mW for component A and B, respectively. In contrast to the one-component control sample, the displacement vectors of the two-component metamaterial (see Figure 4.14(b)) point towards its center and a negative effective thermal expansion coefficient

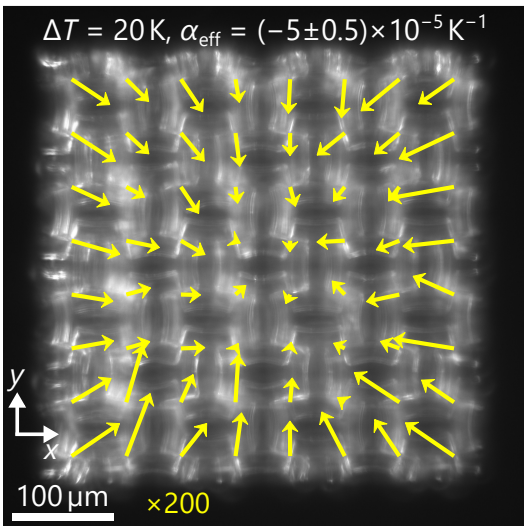

Figure 4.15: Displacement vector field of the same sample as shown in Figure 4.14, but focused on a lower layer (corresponds to P_2 in Figure 4.2). A negative effective thermal expansion coefficient of $\alpha_{\text{eff}} = (-5 \pm 0.5) \times 10^{-5}\,\text{K}^{-1}$ is obtained, but the arrows show much more noise as compared to the measurement in Figure 4.14 due to worse image quality.

of $\alpha_{\text{eff}} = (-5 \pm 0.5) \times 10^{-5}\,\text{K}^{-1}$ is extracted. From the arrows we can also calculate the anisotropy. In y-direction the thermal expansion coefficient is 25 % smaller in absolute value than in x-direction. We explain this with sample imperfections caused by drifts during writing and the pre-bending of the beams during development. Figure 4.14(b) verifies our understanding of the operation mechanism. The bilayer beams still expand positively, but unlike for the control sample, their bending causes rotations of the crosses, alternating between clockwise and anticlockwise rotations in a checkerboard pattern in the same way as it is illustrated in Figure 4.1. The rotations overcompensate the positive expansion of the beams causing an inward movement of the centers of the crosses and hence resulting in a negative effective thermal expansion coefficient.

Figure 4.15 displays the measured displacement vectors for the same sample that was already shown in Figure 4.14, but for the focus plane placed in a layer lower. This corresponds to the plane P_2 shown in Figure 4.2 for the upper layer of unit cells. The image quality is visibly worse, it is focused through the top layer, which is why arrow length and direction fluctuate much more, but the general shrinkage can clearly be seen. The

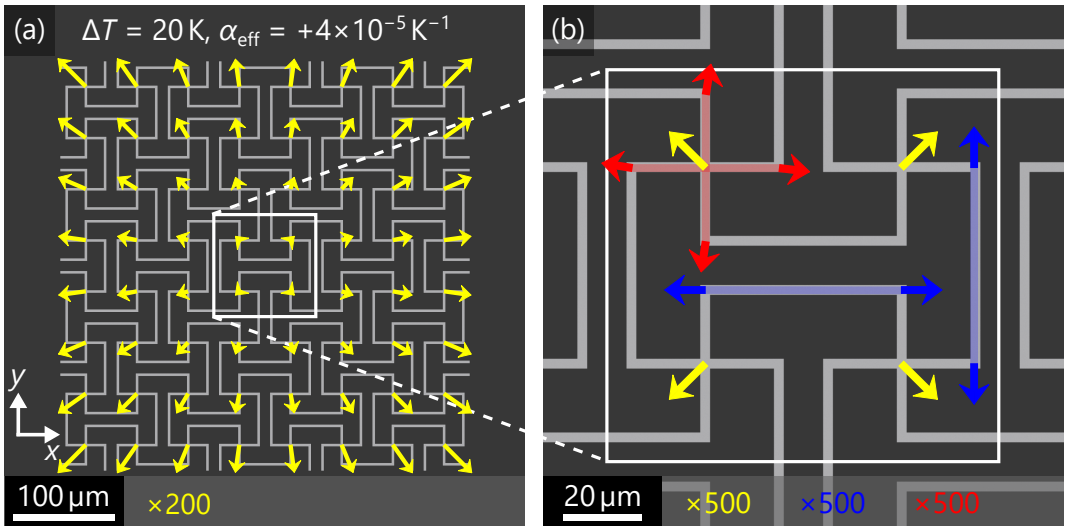

Figure 4.16: Numerical calculations corresponding to the measurements of the control sample shown in Figure 4.13 represented in the same way as the experiments. Material parameters are: $\alpha_A = 4 \times 10^{-5}\,\mathrm{K}^{-1}$, $E_A = 4\,\mathrm{GPa}$, $\nu = 0.4$. From the displacement vector field in (a), we obtain $\alpha_{eff} = +4 \times 10^{-5}\,\mathrm{K}^{-1}$. Adapted from Reference [46].

arrows point inwards and a negative effective thermal expansion coefficient of $\alpha_{eff} = (-5 \pm 0.5) \times 10^{-5}\,\mathrm{K}^{-1}$ is obtained, the same value within the errors as in the top layer. This finding confirms that α_{eff} is also negative inside the metamaterial volume, and not just the outermost layer.

The obtained experimental results are now compared with numerical calculations. The same geometrical and material parameters as in the structure shown in Figure 4.4 are used. To model the experimental conditions, we choose a finite sample with $4 \times 4 \times 2$ unit cells. The computational complexity is decreased by using two planes of mirror symmetry cutting through the center of the structure. One mirror plane is parallel to the xz-plane and the other is parallel to the yz-plane, reducing the geometry to $2 \times 2 \times 2$ unit cells. At the xz-mirror plane the y-component of the displacement vector is set to zero, and analogously the x-component of the displacement vector is set to zero at the yz-mirror plane. The bottom layer is fixed in position, and all other boundaries are free to move.

We present the numerical calculations in the same way as the experiments. Obtained displacement vectors for the one-component control structure are depicted in Figure 4.16 and a positive effective thermal expansion coefficient

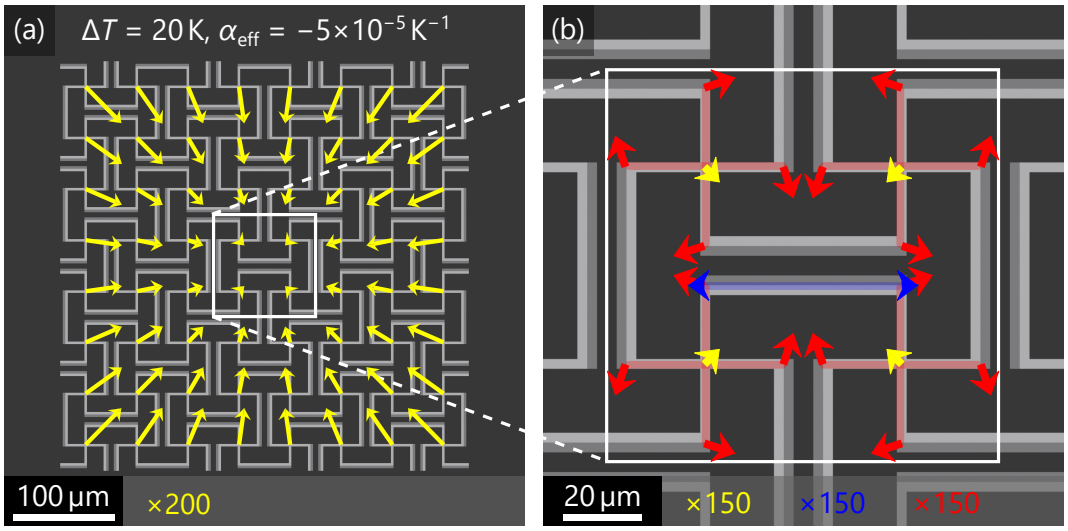

Figure 4.17: Numerical calculations corresponding to the measurements of the two-component metamaterial shown in Figure 4.14 represented in the same way. Material parameters are: $\alpha_A = 4 \times 10^{-5}\,\mathrm{K}^{-1}$, $\alpha_B = 6 \times 10^{-5}\,\mathrm{K}^{-1}$, $E_A = 4\,\mathrm{GPa}$, $E_B = 3\,\mathrm{GPa}$ and $\nu = 0.4$. A negative effective thermal expansion coefficient of $\alpha_{eff} = -5 \times 10^{-5}\,\mathrm{K}^{-1}$ is extracted from the arrows in (a). Adapted from Reference [46].

of $\alpha_{eff} = +4 \times 10^{-5}\,\mathrm{K}^{-1}$ is calculated. The displacement vectors agree well with the experimental results depicted in Figure 4.13. Looking closely into panel (b) a small residual rotation of the cross can be seen. It is a result of the boundary condition of a fixed bottom surface.

Calculated results of the two-component structure are shown in Figure 4.17 and a negative effective thermal expansion coefficient of $\alpha_{eff} = -5 \times 10^{-5}\,\mathrm{K}^{-1}$ is obtained. Again, the displacement vectors agree well with those shown in Figure 4.14 and also visualize the same rotations in panel (b).

Near Zero Thermal Expansion

In Figure 4.5, it was shown that near zero effective thermal expansion coefficient can be obtained by simply increasing the thermal expansion coefficient of component B. Therefore, we have fabricated a metamaterial identical to the one shown in Figure 4.14(a), but with an exposure laser power of 25 mW instead of 19 mW for component B, which results in a larger thermal expansion coefficient (see Figure 4.8).

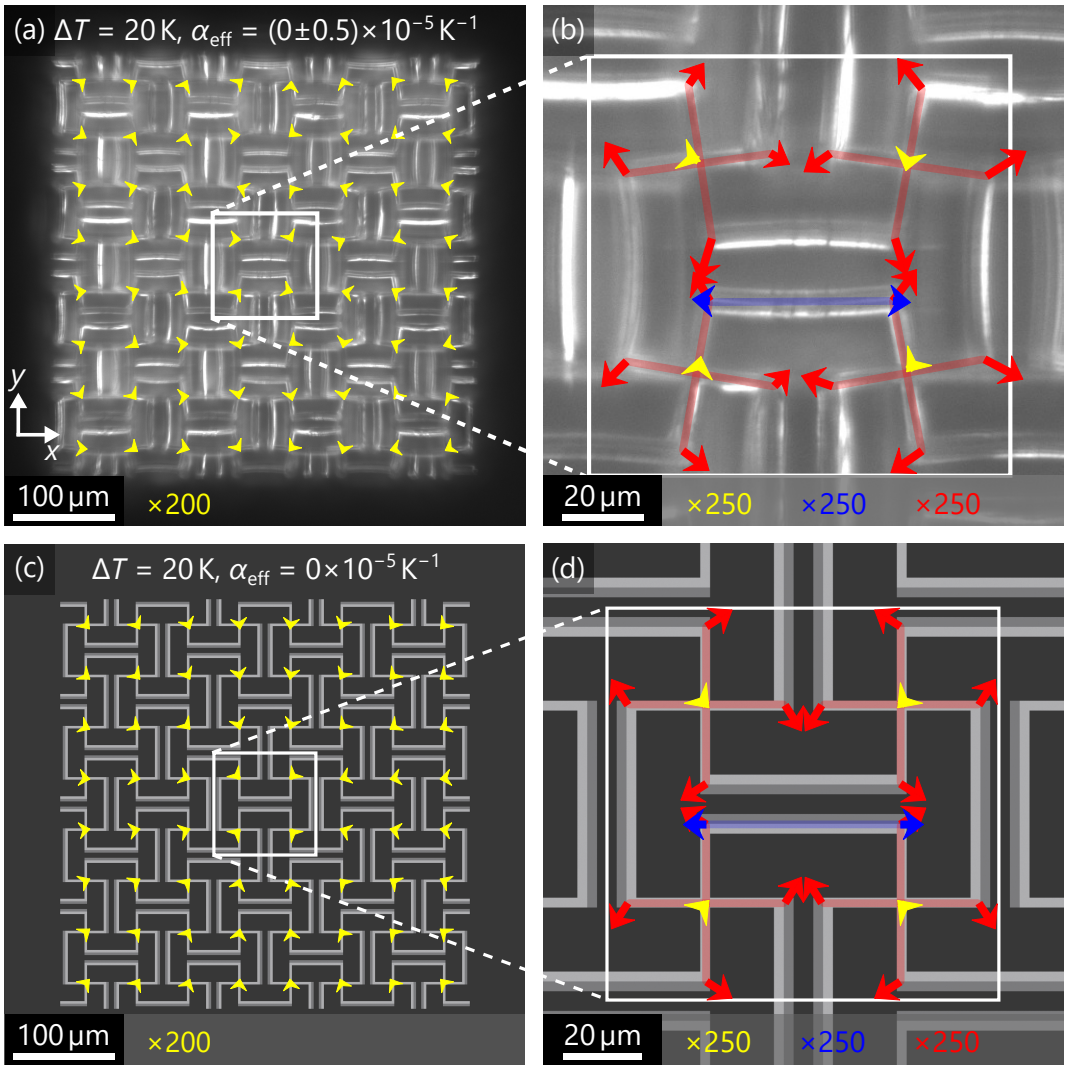

Figure 4.18: (a), (b) Same measurement as shown in Figure 4.14, but for a sample, fabricated with exposure laser powers of 25 mW and 32.5 mW instead of 19 mW and 32.5 mW. The measured displacement vectors agree well with the calculated ones in (c) and (d) and demonstrate a near zero effective thermal expansion coefficient of $\alpha_{\text{eff}} = (0 \pm 0.5) \times 10^{-5}\,\text{K}^{-1}$. Adapted from Reference [46].

On this metamaterial, we have performed the same measurement procedure and image cross-correlation analysis as shown in Figure 4.14. The obtained displacement vectors are depicted in Figure 4.18(a) and (b). The crosses rotate in the same directions as in Figure 4.14(b), but with less magnitude. At this point. they merely compensate the positive beam ex-

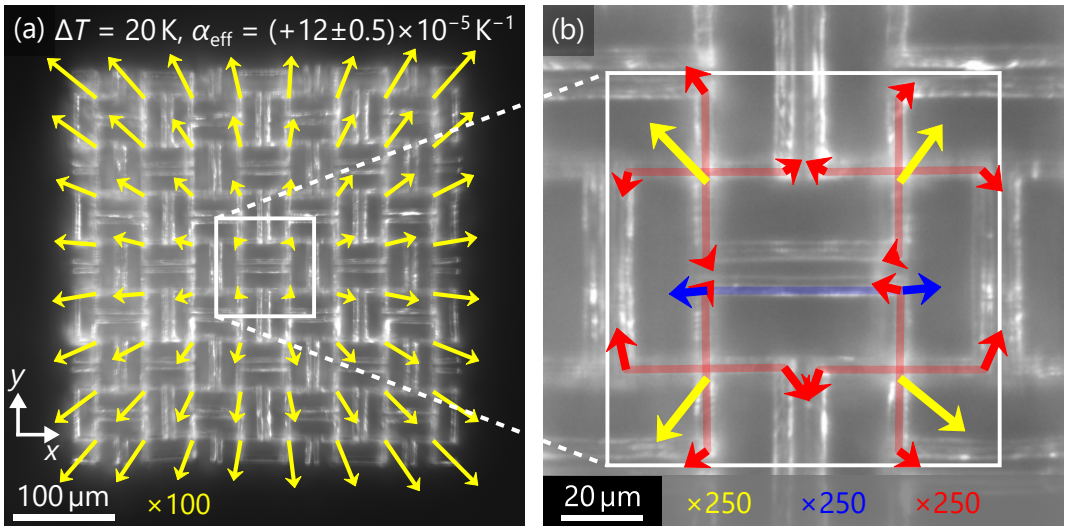

Figure 4.19: Same measurement as shown in Figure 4.14, but for a metamaterial structure with inverted components for the beams (see Figure 4.3(a)). Compared to Figure 4.14(b) crosses now rotate in the opposite direction, adding to the positive effective thermal expansion coefficient of the beams and leading to a large positive effective thermal expansion coefficient of $\alpha_{\text{eff}} = (+12 \pm 0.5) \times 10^{-5}\,\text{K}^{-1}$, which is larger than any of the constituents.

pansion, resulting in a near zero effective thermal expansion coefficient of $\alpha_{\text{eff}} = (0 \pm 0.5) \times 10^{-5}\,\text{K}^{-1}$. It also stands out that there is less pre-bending of the beams than before, indicating that the constituents are also more similar to each other with regard to shrinkage during development. In Figure 4.18(c) and (d), we have reproduced this behavior numerically, using $\alpha_{\text{B}} = 5 \times 10^{-5}\,\text{K}^{-1}$ compared to $\alpha_{\text{B}} = 6 \times 10^{-5}\,\text{K}^{-1}$ as shown in Figure 4.17. Again, numerical and experimental results agree well.

Large Positive, and Anisotropic Thermal Expansion

We have measured the fabricated metamaterial with large positive thermal expansion shown in Figure 4.12(a). The derived displacement vectors are shown in Figure 4.19. Compared to Figure 4.14(b), they reveal an opposite rotation direction of the crosses. Instead of compensating it, the geometrical effect now contributes to the positive expansion of the beams. This leads to a large positive effective thermal expansion coefficient of $\alpha_{\text{eff}} = (+12 \pm 0.5) \times 10^{-5}\,\text{K}^{-1}$.

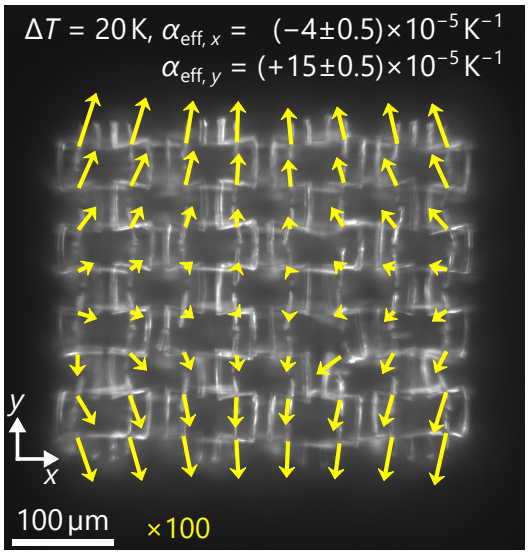

Figure 4.20: Image cross-correlation analysis of a metamaterial designed for anisotropic thermal expansion (see Figure 4.3) with $4 \times 4 \times 2$ unit cells. Effective thermal expansion coefficients of $\alpha_{\text{eff},\,x} = (-4 \pm 0.5) \times 10^{-5}\,\text{K}^{-1}$ along the x-direction and $\alpha_{\text{eff},\,y} = (+15 \pm 0.5) \times 10^{-5}\,\text{K}^{-1}$ along the y-direction are extracted from the displacement vectors.

Using the unit cell design for anisotropic thermal expansion (see Figure 4.3) we further demonstrate striking thermal expansion control. The displacement vectors measured on $4 \times 4 \times 2$ unit cells are shown in Figure 4.20. As designed it has a negative effective thermal expansion coefficient of $\alpha_{\text{eff},\,x} = (-4 \pm 0.5) \times 10^{-5}\,\text{K}^{-1}$ along the x-axis and a large positive effective thermal expansion coefficient of $\alpha_{\text{eff}} = (+15 \pm 0.5) \times 10^{-5}\,\text{K}^{-1}$ along the y-axis.

In conclusion, we have fabricated micro-structured three-dimensional two-component metamaterials by gray-tone laser lithography using only a single photoresist. On these thermoelastic metamaterials, we have experimentally demonstrated effective thermal length-expansion coefficients that ranged from positive value exceeding that of any of the constituents, over zero, to negative or anisotropic values.

4.2 Poroelastic Metamaterials

In the last section, we have introduced a two-component metamaterial, that applies a mechanism to convert positive volume changes of the constituents into a negative effective volume change to obtain negative thermal expansion. In principle, the mechanism works for any volume changes, as long it is different for both constituents by a factor of at least 1.2 for that particular unit cell, which is why we have also seen a negative shrinkage in Figure 4.10. Simply by exchanging the the constituents with different thermal expansion coefficients with constituents with different compressibilities of the same ratio, the effective metamaterial volume will expand under hydrostatic pressure increase, resulting in a negative effective (or unjacketed) compressibility (see Equation 2.99).

However, ordinary polymers have static bulk moduli of a few gigapascals [96], which means that the compressibilities lie below $10^{-9}\,\mathrm{Pa}^{-1}$ and a pressure change of 1 Pa, therefore, only results in relative length changes of around 10^{-10}. To obtain a relative length change of 10^{-3}, which we approximately observed in Figure 4.13 and 4.14, the surrounding hydrostatic pressure has to be increased by $10^7\,\mathrm{Pa} = 100\,\mathrm{bar}$, which is, of course, quite inconvenient for measurements. Therefore, we have introduced a novel idea of including sealed hollow volumes inside the unit cell to make use of the high compressibility of air or vacuum.

4.2.1 Metamaterial Designs

Our first design of a metamaterial with negative effective compressibility is based on the unit cell shown in Figure 4.2. Its vital elements are sealed hollow volumes inside three-dimensional cylindrical crosses, which replace the ordinary crosses. Instead of bilayer beams, it has only one constituent solid material. Figure 4.21(a) shows one unit cell inside a simple cubic translational lattice containing eight of these three-dimensional crosses. A cut through view of one cross is depicted in Figure 4.21(c).

A deformed version of the unit cell calculated with COMSOL Multiphysics (see Section 3.2) is shown in Figure 4.21(b). At increased hydrostatic pressure, the thin circular membranes of the crosses warp inwards (see cut through view in panel (d)). At each membrane, two beams are attached asymmetrically, which translates the warping into a rotation of the crosses, leading

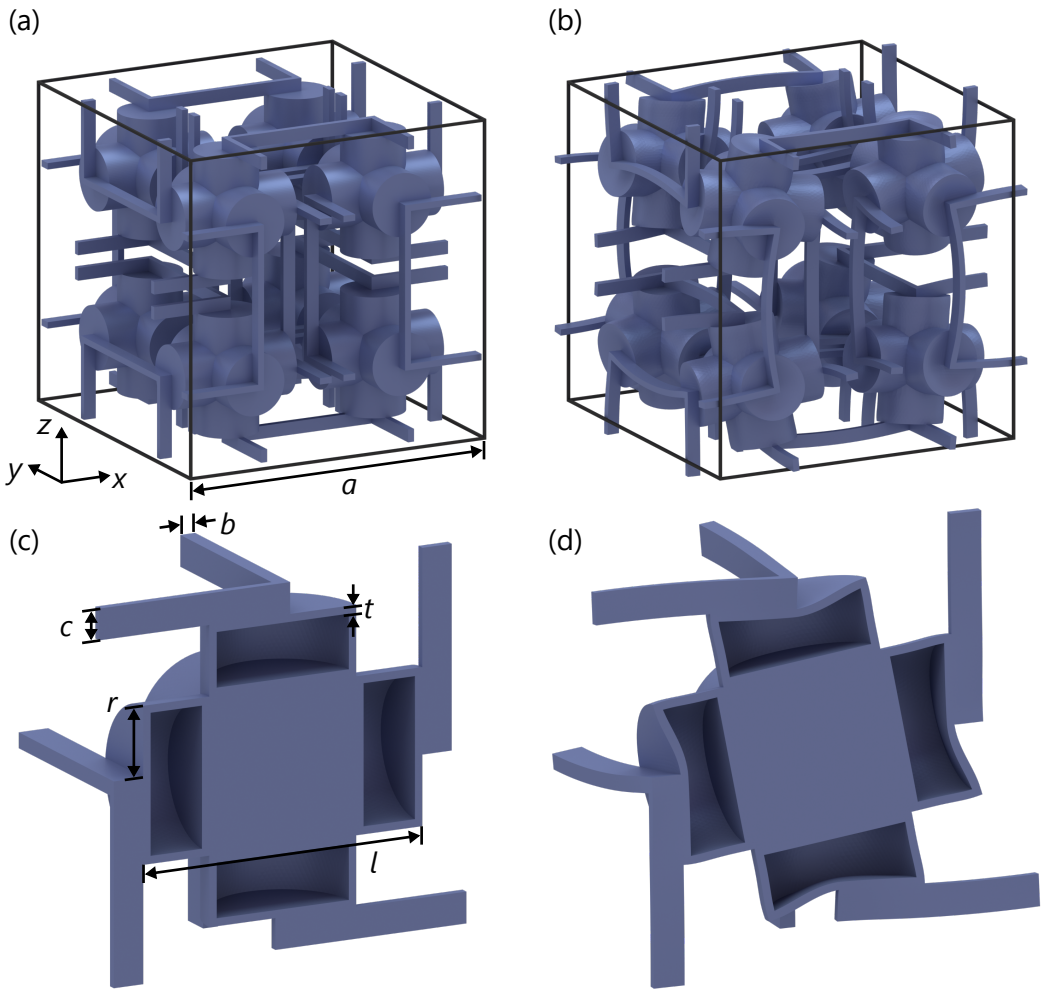

Figure 4.21: (a) Unit cell designed for negative effective compressibility based on Figure 4.1. It contains eight three-dimensional crosses with sealed hollow volumes inside. A cut through view of one cross is shown in (c). All relevant geometrical parameters are indicated. (b) Deformed unit cell under elevated hydrostatic pressure. The warping membranes (see (d)) cause a rotation of the crosses which leads to an overall expansion of the unit cell. Adapted from Reference [63].

to an overall expansion of the unit cell. This is similar to the mechanism for negative thermal expansion discussed in Section 4.1. But in this case, the small volume decrease caused by the positive compressibility of the constituent is negligible and easily overcompensated by the geometrical

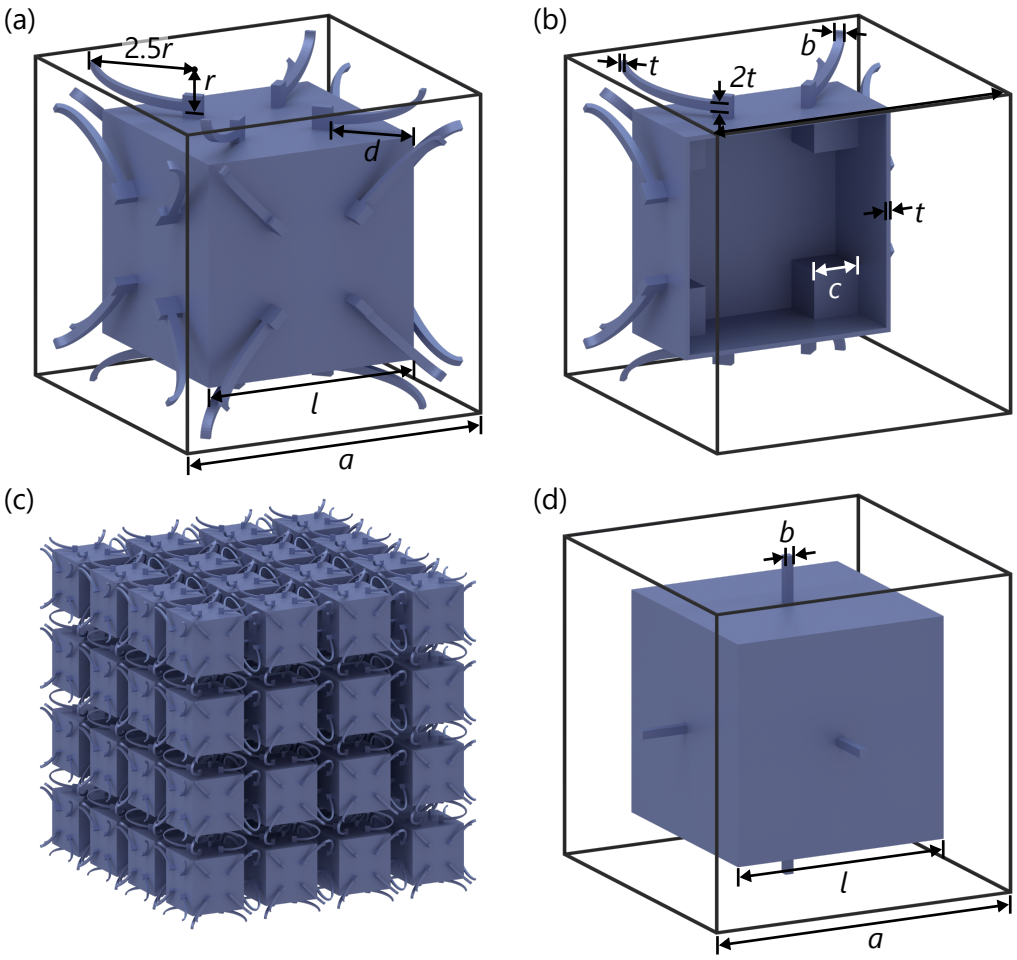

Figure 4.22: (a) Simplified design of a simple cubic unit cell with negative effective compressibility consisting of one hollow cube and lever arms attached to the faces. (b) Cut open unit cell showing the interior. Notice the smaller cubes inside at the corners. (c) Metamaterial with $4 \times 4 \times 4$ unit cells repeated in a simple cubic translational lattice. (d) In comparison, a unit cell designed for large positive effective compressibility with the same interior structure. The lever arms have merged into a single connector in the middle. All relevant geometrical parameters are indicated. Adapted from Reference [84].

effect.

More recently, we have introduced a simplified design depicted in Figure 4.22. Each unit cell has simple cubic symmetry and consists of only one

hollow cube with four lever arms attached to each face. Inside the hollow cube, there are smaller cubes sitting in each corner directly behind the lever arms as shown in the cut open unit cell in Figure 4.22(b). These smaller cubes are important for the development process, as we will see later. The principle of operation is similar. At increased hydrostatic pressure, the warping of the membranes rotates the attached lever arms, causing their ends to move outwards. This leads to an increase of the effective volume. A metamaterial made by $4 \times 4 \times 4$ unit cells is shown in Figure 4.22(c). In Figure 4.22(d), instead of four lever arms, a single connector is attached in the center of each membrane. In comparison to the other design, this leads to large positive effective compressibility.

4.2.2 Static Numerical Calculations

In order to obtain a better understanding of the proposed poroelastic metamaterials and to optimize geometrical parameters, we have performed numerical analyzes using COMSOL Multiphysics (see Section 3.2). The continuum elasticity problem is solved under linear approximation for a small increase of hydrostatic pressure ΔP. This is introduced as a normal force acting on all outer surfaces, including the surfaces at the boundary on the unit cell to mimic the conditions for an unjacketed compressibility test (see Section 2.2.4). Additionally, we assume periodic boundary conditions.

Parameter Sweeps

Let us first focus on the unit cell illustrated in Figure 4.21. The relevant geometrical parameters are the cross length l, the membrane thickness t and radius r, and the beam thickness c and width b. Like in Section 4.1.2, the absolute scale defined by the lattice constant a is irrelevant and only the relative sizes with respect to a matter. Therefore, we express each geometrical parameter with respect to a.

In Figure 4.23, we have performed numerical sweeps for the different geometrical parameters of the unit cell. Unless varied, each parameter is held constant at the standard values of $t/a = 1\,\%$, $r/a = 10\,\%$, $b/a = 2\,\%$, $c/a = 4\,\%$, and $l/a = 38\,\%$. The hollow volumes are assumed to be completely empty (vacuum).

Since the unit cells consist of only one constituent material, the effective compressibility scales proportionally with the constituent's Young's modulus

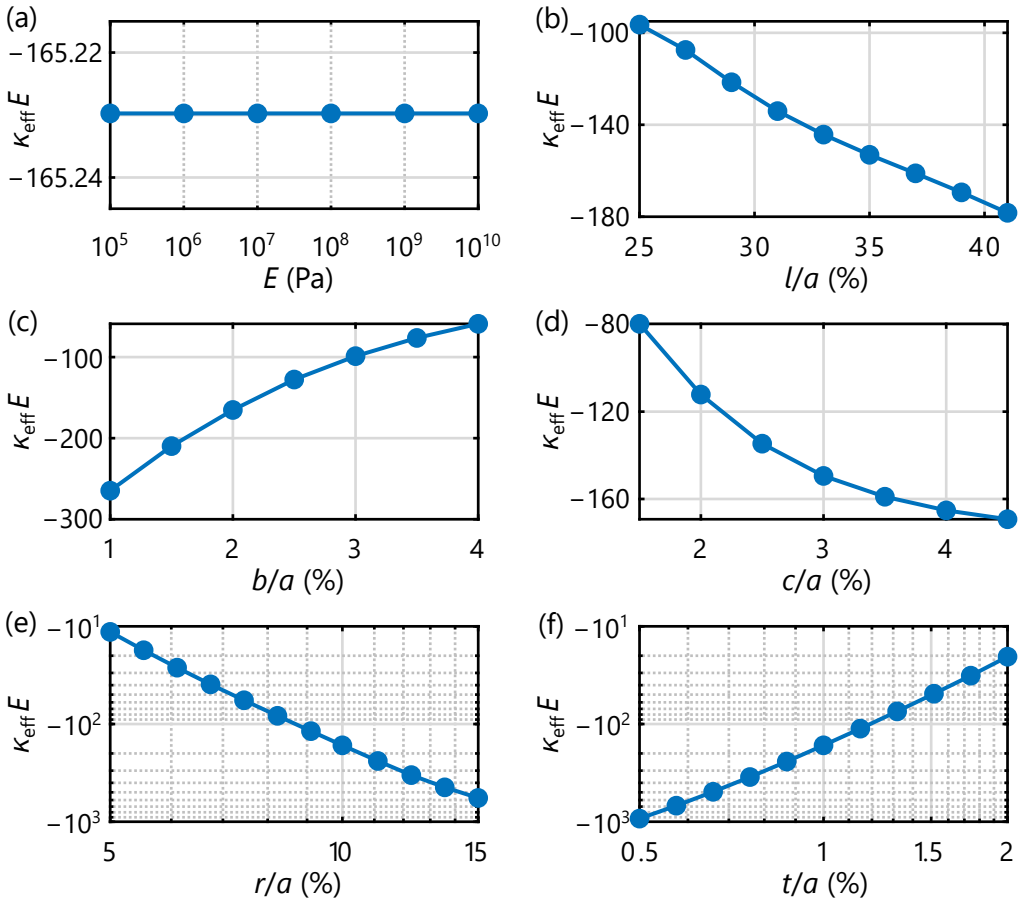

Figure 4.23: Numerical parameter sweeps on the unit cell introduced in Figure 4.21. (a) We calculate the dimensionless product $\kappa_{\text{eff}}E$ which is independent of E. For a standard parameter set of $t/a = 1\,\%$, $r/a = 10\,\%$, $b/a = 2\,\%$, $c/a = 4\,\%$, and $l/a = 38\,\%$ and a constituent's Poisson's ratio of $\nu = 0.4$, this set leads to $\kappa_{\text{eff}}E = -165.23$, compared to $\kappa E = +0.6$ of the constituent solid. (b)-(f) One geometrical parameter is varied as indicated. All other parameters are fixed to the standard parameter set. Adapted from Reference [63].

E. Or in other words, $\kappa_{\text{eff}}E$ is constant over E. This is numerically confirmed in Figure 4.23(a) over five orders of magnitude. Therefore, the calculated effective compressibility is represented by the dimensionless product $\kappa_{\text{eff}}E$, which is representative for any value of E. For the Poisson's ratio of the constituent, a typical polymer value of $\nu = 0.4$ is chosen. Together with the standard parameter values stated above, we obtain a negative effective compressibility $\kappa_{\text{eff}}E = -165.23$. Compared to the value for the constituent

material,

$$\kappa E = \frac{E}{K} = 3(1-2\nu) = 0.6\,, \tag{4.5}$$

the absolute value of the effective compressibility is more than two orders of magnitude larger. Remarkably, this unit cell also exhibits a negative Poisson's ratio of -0.97, which approaches the limit of a perfect dilational metamaterial [22].

Figure 4.23(b) demonstrates that the modulus of $\kappa_{\text{eff}}E$ increases for larger l/a, similar to the result in Figure 4.7(a). From panels (c) and (d) we conclude that large aspect ratios c/b of the beams are favorable. On the one hand, c/a has to be large since the beams should not bend in that direction to force the crosses to rotate. On the other hand, b/a has to be small, to allow the beams to bend easily along that direction to allowing the orthogonal rotations of the crosses. The membrane radius and thickness have, by far, the largest influence on $\kappa_{\text{eff}}E$ as seen in the double logarithmic plots of panels (e) and (f). To obtain a large effect, thin membranes with large radii are preferred.

We apply the gained knowledge to slightly adjust the geometrical parameters to $t/a = 0.7\,\%$, $r/a = 12\,\%$, $b/a = 1.5\,\%$, $c/a = 4\,\%$, and $l/a = 38\,\%$. These are the parameters further used for fabrication. To stay within experimentally feasible values, we choose a lattice constant of $a = 150\,\mu\text{m}$. Furthermore, the sealed hollow volumes are connected through the center of the cross, reducing the number of sealed hollow volumes by a factor of four. This does not noticeably alter the magnitude of effective compressibility but simplifies the fabrication process. The resulting unit cell is depicted in Figure 4.24.

Evacuated and Air-Filled Interior Volumes

Until now, all sealed hollow volumes were assumed to be evacuated, i.e. to have an interior pressure of $P_{\text{i}} = 0$. During the actual measurements, they are, however, air-filled with an initial interior pressure of $P_{\text{i}} = P_0 \approx 1.01\,\text{bar}$. When the external air pressure is increased by ΔP, the membranes warp inwards, decreasing the interior volume V_{i} and hence increasing the interior pressure by ΔP_{i}. We have numerically investigated the influence of gas filled interior volumes for the simple cubic unit cells in Figure 4.22 for different values of t/a and otherwise fixed and optimized geometrical parameters of: $b/a = 3\,\%$, $c/a = 15\,\%$, $d/a = \sqrt{2}(c/a + t/a + 0.04)$, $l/a = 70\,\%$, and $r/a = 48\,\% - 0.5\,l/a$. The elastic solid is modeled with typical polymer

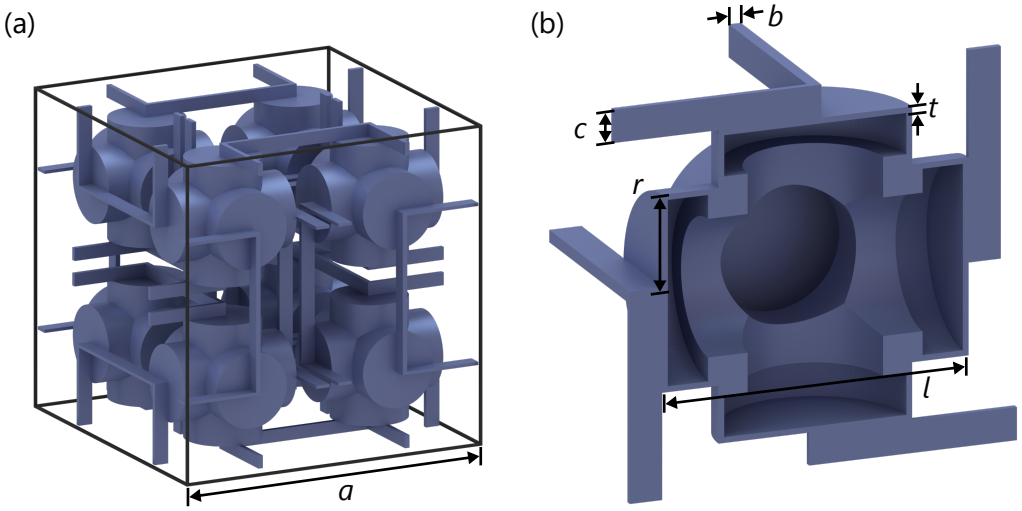

Figure 4.24: Adjusted unit cell optimized for fabrication (a) and a cut through on cross (b) based on the design shown in Figure 4.21. All interior hollow volumes within one cross are connected through the center. Geometrical parameters are $a = 150\,\mu\text{m}$, $t/a = 0.7\,\%$, $r/a = 12\,\%$, $b/a = 1.5\,\%$, $c/a = 4\,\%$, and $l/a = 38\,\%$. Adapted from Reference [83].

values of $E = 3\,\text{GPa}$ and $\nu = 0.4$. The gas is assumed to be an ideal gas. Since the interior volume is sealed, the equation $P_\text{i} V_\text{i} = n_i RT = \text{const.}$ holds. As initial conditions, the exterior hydrostatic pressure P and the interior gas pressure P_i are both set to the reference pressure $P_0 = 1.01\,\text{bar}$, at which the geometry is assumed to be at equilibrium. The interior hollow volume has an initial value of $V_\text{i} = V_{\text{i},0}$.

First, the exterior pressure is increased to $P = P_0 + \Delta P$ while the interior pressure is held constant ($P_\text{i} = P_0$) and the deformed unit cell (see insets in Figure 4.25) is calculated under periodic boundary conditions. Using Gauss's theorem, we can avoid meshing the interior and directly calculate the interior volume change ΔV_i by integrating the normal component of the displacement vector over the interior surface, which gives us the interior volume V_i for $P_\text{i} = P_0$. As the constituent material is nearly incompressible compared to the flexible membranes we can approximate $V_\text{i} \approx V_{\text{i},0}$ for $P_\text{i} = P = P_0 + \Delta P$. As the interior volume V_i is known for two values of P_i, we can linear interpolate in between to find the corresponding interior pressure that fulfills the condition $P_\text{i} V_\text{i} = n_\text{i} RT$. Including this value of P_i, the numerical calculations are repeated and the convergence of $P_\text{i} V_\text{i}$ towards $n_i RT$ is checked. This process can be iteratively refined. For the calculations

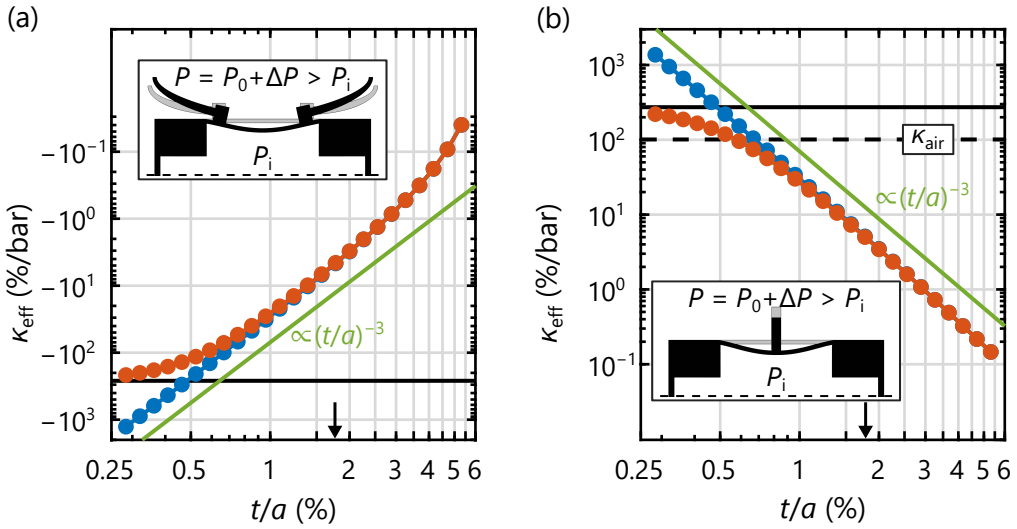

Figure 4.25: Calculated effective compressibilities for the unit cells with (a) $\kappa_{\text{eff}} < 0$ introduced in Figure 4.22(a) and (b) $\kappa_{\text{eff}} > 0$ introduced in Figure 4.22(d) over the membrane thickness t/a. Note the double-logarithmic scale. In the case of evacuated cubes ($P_i = P_0 = 0$ shown in blue), κ_{eff} diverges with the same slope as the green lines (3 and -3 for (a) and (b), respectively) for $t/a \to 0$. For air-filled cubes ($P_0 = 1.01\,\text{bar}$ shown in red), κ_{eff} converges towards the horizontal solid black lines instead, which are independently calculated. The dashed black line corresponds to the compressibility $\kappa_{\text{air}} = 101\,\%/\text{bar}$ of air. Two insets show a diagonal cut through the deformed unit cell (black) compared to the undeformed state at $\Delta P = 0$ (gray), illustrating the mechanism. The arrows point at the ratios t/a used in Figure 4.39. Parameters are: $b/a = 3\,\%$, $c/a = 15\,\%$, $d/a = \sqrt{2}(c/a + t/a + 0.04)$, $l/a = 70\,\%$ and $r/a = 48\,\% - 0.5l/a$. Adapted from Reference [84].

under linear approximation, however, no further iterations are needed. With the correct value for P_i, κ_{eff} is calculated.

The calculated values for κ_{eff} over t/a are summarized in Figure 4.25 in double-logarithmic plots. In the case of evacuated cubes (blue points), the effective compressibility diverges with $|\kappa_{\text{eff}}| \propto (t/a)^{-3}$ for $t/a \to 0$ both for the unit cell designed for $\kappa_{\text{eff}} < 0$ (panel (a) and Figure 4.22(a)) and $\kappa_{\text{eff}} > 0$ (panel (b) and Figure 4.22(d)), as indicated by the green lines. In the case of air-filled cubes (red points), κ_{eff} converges for $t/a \to 0$ in both panels. Interestingly, the red points in panel (b) converge to a value of about 270 %/bar, which is almost three times as large as the compressibility

$\kappa_{\text{air}} = 101\,\%/\text{bar}$ of air (dashed line).

To verify the iterative method to calculate the air filled cubes described above, we have modeled the air inside as an isotropic Cauchy elastic solid, with a bulk modulus of $K = 1.01 \times 10^5\,\text{Pa}$ and a near zero shear modulus. The results are indistinguishable from the ones obtained from the iterative method (red points in Figure 4.25).

There is an intuitive explanation for the different behavior between evacuated and air-filled cubes [84]: The elastic behavior of membranes was intensively studied by Timoshenko [88]. It is well-known that the displacement in the center of a thin clamped circular membrane with radius r_{m} and thickness t is proportional to r_{m}^4/t^3 for a fixed pressure difference between both sides. The scaling with t^{-3} also holds for different shapes, like rectangular membranes. The behavior of the cubes under a small pressure increase can be modeled with Hooke's springs. Along each principle cubic direction, there are two membranes on opposite sides of the cube. Their displacement can be expressed as an effective Hooke's spring with a spring constant $D_1 \propto 1/t^3$. The compression of the air inside acts like a second Hooke's spring D_2 parallel to the first. For evacuated cubes the resulting spring constant is equal to D_1, as $D_2 = 0$. This fits with the $(t/a)^{-3}$ scaling of the blue points in Figure 4.25. For air-filled cubes, D_2 is finite. As $D_1 \to 0$ for $t/a \to 0$, the resulting spring constant converges to D_2.

For a warped circular membrane, the displacement in the center is approximately twice as large as the average displacement. The relative length change is, therefore, about twice as large as the relative volume change $\Delta V_{\text{i}}/V_{\text{i}}$, that defines the spring constant D_2. In our case, the ratio is even larger. This is the reason why the air-filled cubes converge to an effective compressibility larger than that of air in Figure 4.25(b). We can put this into a simple formula. In the linear regime for a small increase of surrounding hydrostatic pressure ΔP, and a corresponding increase of the interior pressure ΔP_{i}, the compressibilities κ_{eff} and κ_{air} can be written as

$$\kappa_{\text{eff}} = -\frac{1}{V_{\text{eff}}}\frac{\Delta V_{\text{eff}}}{\Delta P}\,, \qquad \text{and} \qquad \kappa_{\text{air}} = -\frac{1}{V_{\text{i}}}\frac{\Delta V_{\text{i}}}{\Delta P_{\text{i}}}\,. \tag{4.6}$$

For $t/a \to 0$ the interior pressure change converges to ΔP. The effective compressibility in the limit of small t/a, can be expressed as

$$\kappa_{\text{eff}}^{\text{lim}} = \kappa_{\text{air}}\,\frac{\Delta V_{\text{eff}}/V_{\text{eff}}}{\Delta V_{\text{i}}/V_{\text{i}}}\,. \tag{4.7}$$

The fraction on the right side of the equation mainly depends on the area of the membranes and the size of the interior volume. At small t/a it is approximately constant with respect to t/a. We have calculated its value for the smallest t/a values of the evacuated cubes (blue points at the left end of plot panel in Figure 4.25). In the case of $\kappa_{\text{eff}} < 0$, a value of -2.6 is obtained, while for $\kappa_{\text{eff}} > 0$, the result is $+2.7$. The corresponding limits for the effective compressibility according to Equation 4.7 are plotted as solid horizontal lines in each graph. These horizontal lines are calculated from the behavior of the evacuated cubes alone and clearly predict the convergence behavior of κ_{eff} for the air-filled cubes (red points) for $t/a \to 0$.

These different results between air-filled and evacuated cubes brings up the question, whether the unboundedness of κ_{eff} is a direct consequence of the infinite compressibility of vacuum. Let us do a gedankenexperiment. We modify the unit cell with $\kappa_{\text{eff}} > 0$ (Figure 4.22) by assuming a rigid material everywhere, except in the center of the faces, where a flexible membrane with radius r_{m} and thickness t is embedded. We keep r_{m}^4/t^3 constant and scale b with r_{m} according to $b/r_{\text{m}} = \text{const.} \ll 1$. In the limit of $r_{\text{m}} \to 0$ $(\Delta V_{\text{eff}}/V_{\text{eff}})/(\Delta V_{\text{i}}/V_{\text{i}})$ diverges with $1/r_{\text{m}}^2$. Hence, even for air filled cubes, there is no fundamental bound for κ_{eff}.

4.2.3 Eigenfrequency Calculations

It is expected that poroelastic materials have two longitudinal modes (see Section 2.2.4) instead of one in ordinary isotropic elastic materials. To investigate whether the sign of κ_{eff} has any influence on the dynamic behavior, we have calculated the acoustic band structure of both the unit cells with $\kappa_{\text{eff}} < 0$ and $\kappa_{\text{eff}} > 0$ introduced in Figure 4.22.

We have chosen a lattice constant of 75 µm, a relative membrane thickness of $t/a = 2\,\%$ and otherwise the same geometrical parameters as in Figure 4.25. The constituent solid elastic material was modeled with a density of $\rho = 3000\,\text{kg/m}^3$, a Poisson's ratio of $\nu = 0.4$ and various Young's moduli E. The surrounding gas was modeled with a density of $\rho_{\text{air}} = 1.2\,\text{kg/m}^3$ and a bulk modulus of $K_{\text{air}} = 10^5\,\text{Pa}$.

Using COMSOL Multiphysics the coupled acousto–elastic wave equations were solved under Floquet-Bloch periodicity (see Section 3.2). Band structures for the unit cell with $\kappa_{\text{eff}} < 0$ and are shown in Figure 4.26, calculated for Young's Moduli of 2000 GPa, 700 GPa, 458 GPa, and 40 GPa. Here, the wave vectors $\vec{k}$ lie between the Γ and X-point of the reciprocal unit cell. There

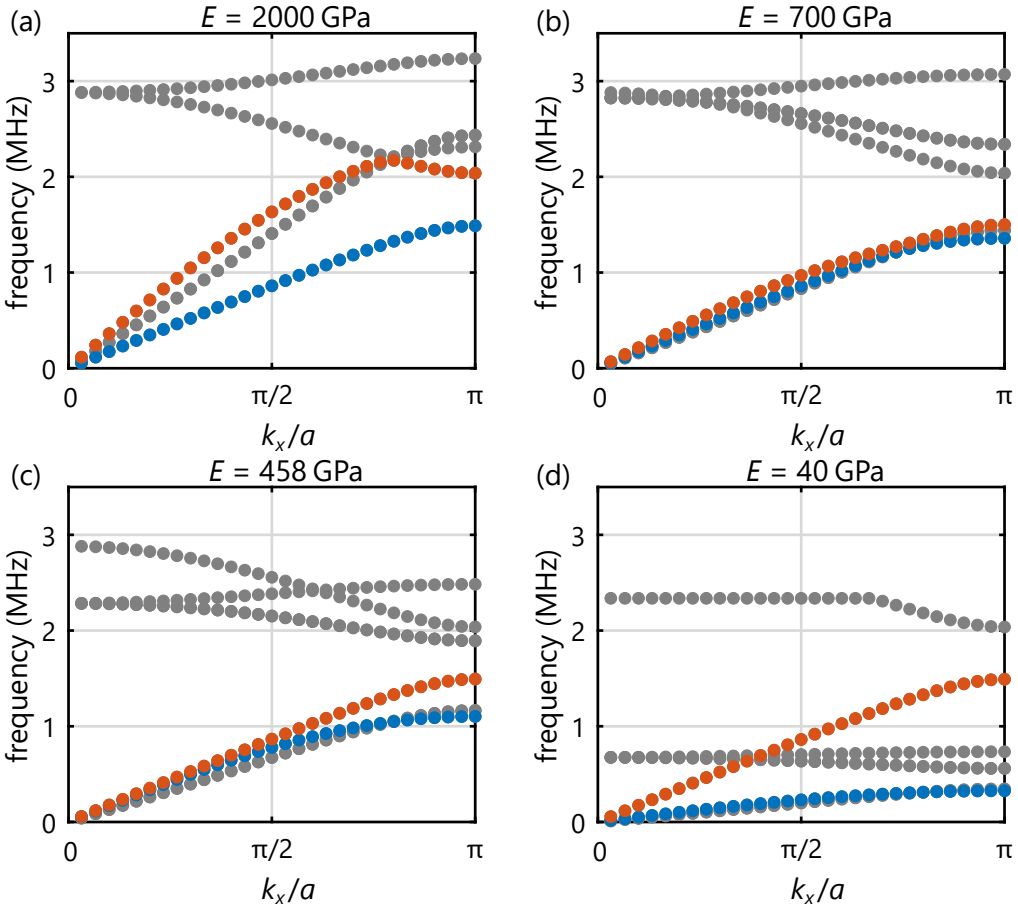

Figure 4.26: Acoustic band structures for wave vectors between Γ and X of the simple cubic Brillouin zone, calculated for the unit cell shown in Figure 4.22(a) with a constituent Young's modulus of (a) $E = 2000\,\mathrm{GPa}$, (b) $E = 700\,\mathrm{GPa}$, (c) $E = 458\,\mathrm{GPa}$, and (d) $E = 40\,\mathrm{GPa}$. Geometrical parameters are $a = 75\,\mu\mathrm{m}$, $t/a = 2\,\%$ and otherwise the same as in Figure 4.25. The two longitudinal bands are highlighted in blue and red.

are two longitudinal modes, highlighted in blue and red, respectively. Both are coupled acousto-elastic modes described with an acoustic pressure p in the fluid and an elastic dilatation e in the solid, with different relative amplitudes and phases.

In Figure 4.27, the dilatations e of the solid unit cells are plotted over the phase for $k_x/a = 0.1$. Blue and red curves correspond to blue and red points

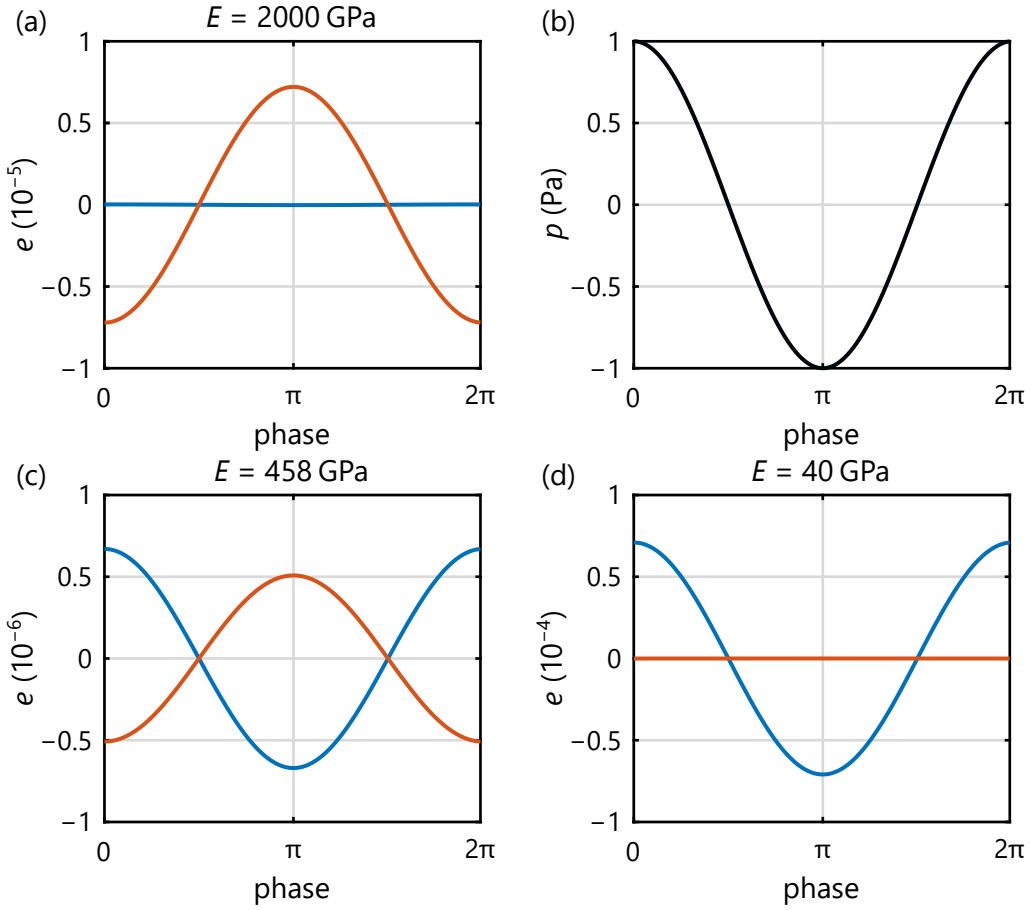

Figure 4.27: (a),(c), and (d) Dilatation e over the phase for the longitudinal modes at $k_x/a = 0.1$ shown in the panels (a),(c), and (d) of Figure 4.26. Blue and red curves correspond to blue and red points in Figure 4.26, respectively. The dilatations are normalized with regard to an acoustic pressure (b) with an amplitude of 1 Pa.

in Figure 4.26, respectively. Figure 4.28 and 4.29 show the same calculations as Figure 4.26 and 4.27, but for the unit cell with $\kappa_{\text{eff}} > 0$.

The amplitudes of e correspond to an acoustic pressure p normalized with an amplitude of $p_0 = 1\,\text{Pa}$ in the gas (see Figure 4.27(b)). For the upper longitudinal modes (red), e and p are out of phase, while they are in phase for the lower longitudinal modes (blue). This basically confirms the theoretical prediction of Biot [13] (also see Section 2.2.4). The acoustic wave

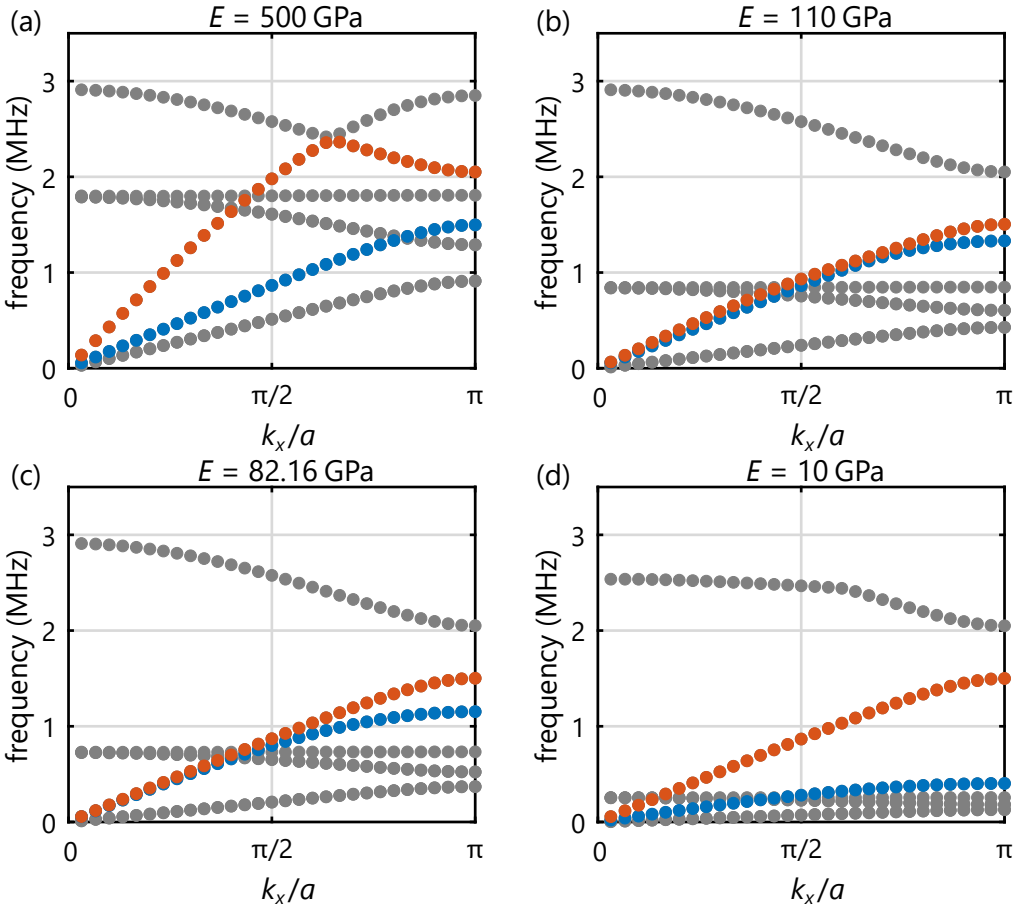

Figure 4.28: Acoustic band structures for wave vectors between Γ and X of the simple cubic Brillouin zone, calculated for the unit cell shown in Figure 4.22(d) with a constituent Young's modulus of (a) $E = 500\,\mathrm{GPa}$, (b) $E = 110\,\mathrm{GPa}$, (c) $E = 82,16\,\mathrm{GPa}$, and (d) $E = 10\,\mathrm{GPa}$. Geometrical parameters are $a = 75\,\mu\mathrm{m}$, $t/a = 2\,\%$ and otherwise the same as in Figure 4.25. Both longitudinal bands are highlighted in color.

in the gas has a maximum potential energy density of

$$\frac{E_{\mathrm{pot}}}{V} = \frac{p_0^2}{\rho_{\mathrm{air}}\, c_{\mathrm{air}}^2} = 3.54 \times 10^{-6}\,\mathrm{J/m^3}\,. \tag{4.8}$$

The maximum potential energy densities of the elastic mode are calculated via

$$\frac{E_{\mathrm{pot}}}{V} = \frac{1}{2} E_{\mathrm{solid}} e^2\,, \tag{4.9}$$

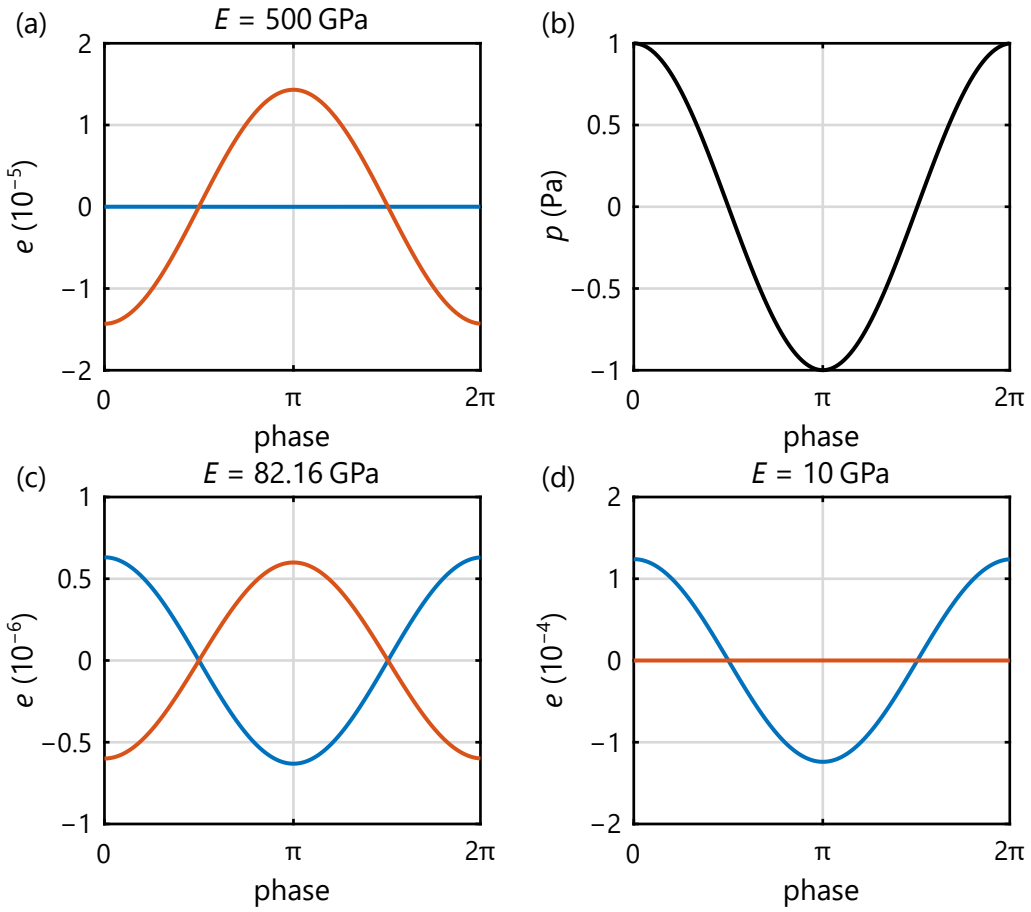

Figure 4.29: Same as Figure 4.27, but corresponding to Figure 4.28.

where E_{solid} is the Young's modulus of the solid structure.

From the amplitudes in Figure 4.27(a) and with the calculated value of $E_{\text{solid}} = 111.33\,\text{MPa}$, we obtain maximum energy densities of $E_{\text{pot}}/V = 2.61 \times 10^{-8}\,\text{J/m}^3$ for the blue curve and $E_{\text{pot}}/V = 2.90 \times 10^{-3}\,\text{J/m}^3$ for the red curve. Comparing these values with Equation 4.8 shows that the blue points in Figure 4.26(a) are mainly modes of acoustical nature, while the red points are mainly elastic modes. Also, an anticrossing between the red branch and the back folded blue branch is observed (at $\approx 2.2\,\text{MHz}$).

When lowering the Young's Modulus of the solid constituent, the elastic wave velocity decreases and hence, the red points in Figure 4.26 move downwards, while the blue points stay approximately constant. At the point where both branches are expected to cross, an anticrossing is observed

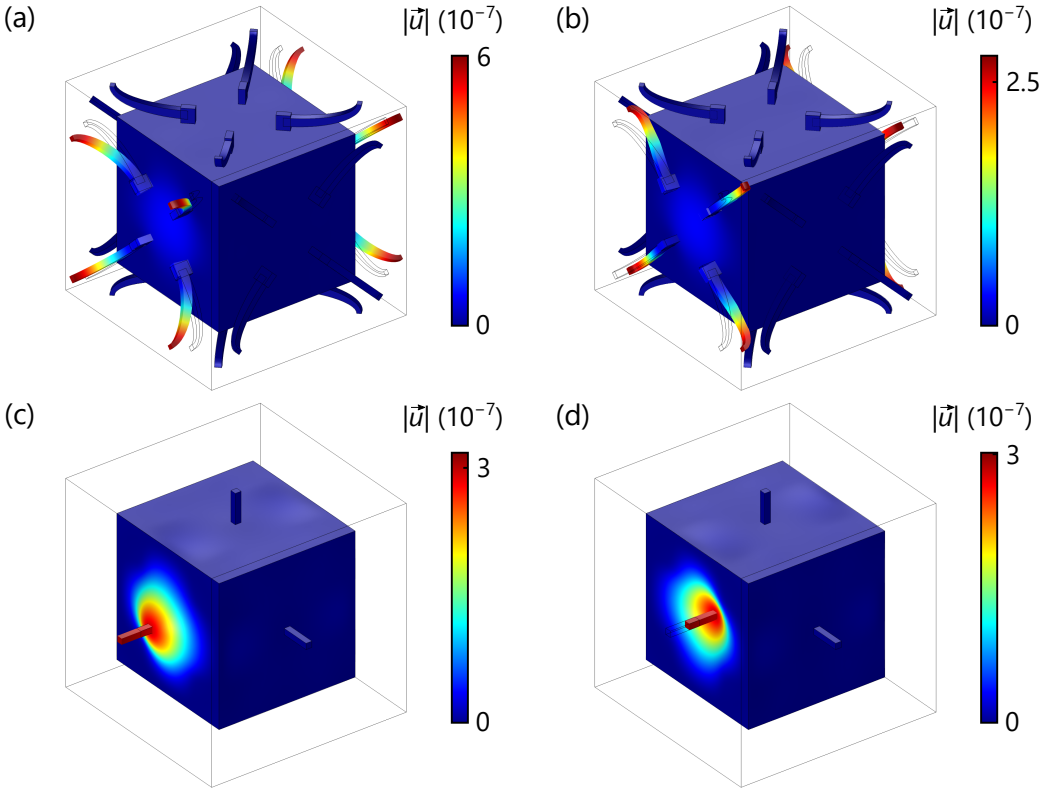

Figure 4.30: Elastic eigenmodes at a phase of zero corresponding to the (a) blue and (b) red curve of Figure 4.27(c), and the (c) blue and (d) red curve of Figure 4.29(c). The modulus of the displacement vector $|\vec{u}|$ is plotted in a false color scale.

again (see Figure 4.26(b) and (c)). The corresponding maximum energy densities to the amplitudes shown in Figure 4.27(c) are $E_{\text{pot}}/V = 5.72 \times 10^{-6}\,\text{J/m}^3$ (blue curve) and $E_{\text{pot}}/V = 3.29 \times 10^{-6}\,\text{J/m}^3$ (red curve). Both are on the same order as the maximum acoustical energy density (Equation 4.8), and are, therefore, strongly mixed acousto-elastic modes. Further decreasing E, acoustic and elastic modes decouple again. For $E = 40\,\text{GPa}$ in Figure 4.26(d), the blue points are mainly elastic modes, while the red points have become mainly acoustic modes. From Figure 4.27(d), we calculate maximum energy densities of $E_{\text{pot}}/V = 2.24 \times 10^{-2}\,\text{J/m}^3$ (blue curve) and $E_{\text{pot}}/V = 8.41 \times 10^{-10}\,\text{J/m}^3$ (red curve).

The shape of the longitudinal elastic eigenmodes are depicted in Figure 4.30. They correspond to Figure 4.27(c) and 4.29(c) at a phase of zero, and

look very similar for both unit cells.

Comparing the dynamic calculations of the unit cell with $\kappa_{\text{eff}} < 0$ $\kappa_{\text{eff}} > 0$, we observe no fundamentally different behavior. In Section 2.2.4, we have already seen that the dependence of the poroelastic constants on the sign of κ_{eff} enters as $\kappa_{\text{eff}}/\kappa_{\text{j}}$. The jacketed compressibility κ_{j} is even much larger than κ_{eff} for our structures. For the unit cell shown in 4.22(a), we have calculated $\kappa_{\text{eff}}/\kappa_{\text{j}} = -0.013$, which is only a minor contribution. Therefore, we conclude that the sign of κ_{eff} does not significantly alter the dynamic behavior of our poroelastic metamaterial.

4.2.4 Fabrication of Sealed Hollow Volumes

The fabrication of the required sealed hollow volumes is a challenging task. Not only do they have to be sealed, but also airtight with a timescale much longer than the time it takes for measurement. As mentioned in the previous chapter, one advantage of micro-fabrication with DLW over conventional macroscopic 3D printing methods is the ability to write without support structure. But even then, fabricated sealed hollow volumes will still be filled with the liquid monomer, that has to be removed.

We have discovered that the solvent (in our case mr-Dev 500) permeates through the membranes during development, expanding the hollow volumes in the process. This also means that the membranes are rather impermeable for the liquid monomer in comparison. For thin membranes, the osmotic pressure built inside rips them open, allowing the liquid monomer to escape. This process is shown in Figure 4.31. After dissolving all monomer and drying the sample, the hollow volumes will eventually be filled with air.

The key issue within this process is the way, in which the hollow volumes burst open. If the stresses during the build up of osmotic pressure are rather uniformly distributed, it will rip open large cracks, which are, of course, not airtight. The size of the cracks can be influenced by tailoring the stress distribution. If the stresses are confined in small "weak spots" of the membrane, these locations will break beforehand and the resulting cracks will be comparably small. Luckily for us, these small cracks can seal themselves afterwards, leaving us with airtight sealed hollow volumes.

We have investigated this process for different unit cells. All fabricated structures in this section are written with an exposure laser power of 19 mW, a slicing distance of 200 nm and a hatching distance of 100 nm. Figure 4.32(a)

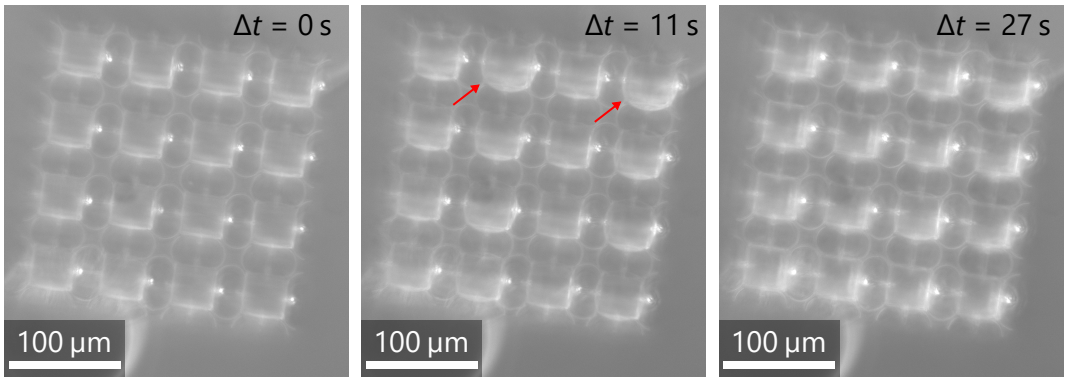

Figure 4.31: Structure with sealed hollow cubes during development with mr-Dev 500. The time passed after the first image (left) is taken is indicated. After a few seconds permeation of the solvent into the cubes lead to an expansion until they have almost spherical shape (see red arrows). After that, they burst and release the liquid monomer, that was trapped inside. After just half a minute, all cubes are ruptured.

shows a scanning electron microscope picture of a fabricated metamaterial with $2 \times 2 \times 2$ unit cells based on the design from Figure 4.24. The used geometrical parameters are $a = 150\,\mu\text{m}$, $t = 1.05\,\mu\text{m}$, $r = 18\,\mu\text{m}$, $b = 2.25\,\mu\text{m}$, $c = 6\,\mu\text{m}$, and $l = 57\,\mu\text{m}$. In the input geometry for DLW, we reduce the thickness of the membranes parallel to the xy-plane by $0.5\,\mu\text{m}$ to compensate for the aspect ratio of the laser focus. Note that due to the finite voxel sizes, the real membrane thicknesses are still expected to be larger than the numerical input values.

One of the cracks that opened during development can be seen in the middle of the membrane depicted in Figure 4.32(b). Its position fits with the location of the maximum von Mises stress calculated for an increase of internal pressure shown below. The lever arms are connected in a L-shape on the membrane, which confines the von Mises stress in a small region. The resulted crack is, therefore, rather small and has resealed after development. Later, we will see that it is also airtight. As all hollow volumes within one cross are interconnected, only one membrane needs to undergo the breaking and resealing process.

The best way to measure how airtight the volumes are, is by observing the expected metamaterial effect. Therefore, we compare the results with an identical metamaterial structure, but with holes inside each hollow cross (see Figure 4.32(c)) to make it intentionally not airtight. These crosses have no visible cracks, since the hole allowed the liquid photoresist to flow out

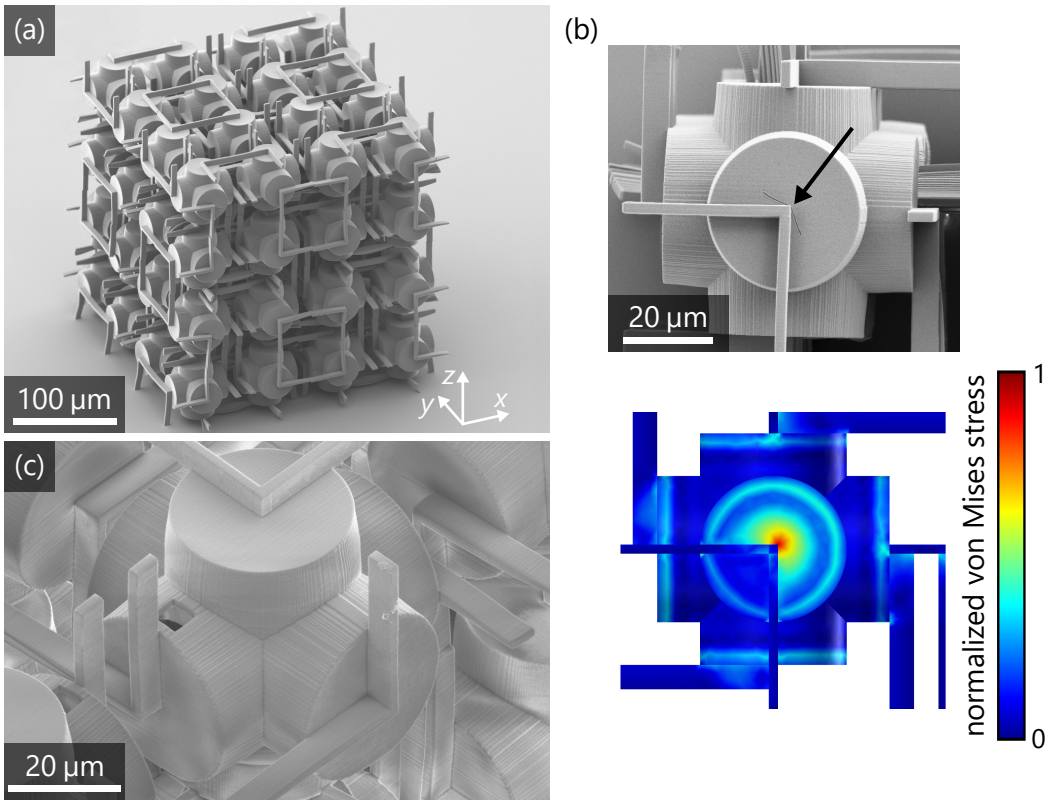

Figure 4.32: (a) Scanning electron micrograph of a fabricated metamaterial with $2 \times 2 \times 2$ unit cells based on the blueprint depicted in Figure 4.24. (b) Zoom-in onto one cross, showing a small crack that opened in the middle of one membrane during the development process. The position fits to the computed maximum von Mises stress shown below. (c) Zoom-in of a control sample with holes intentionally introduced into each hollow cross, resulting in an intentional not airtight structure. Adapted from Reference [83].

during development.

To show the importance of the smaller cubes at the interior corners shown in Figure 4.22(b), we have investigated similar design, but without the inner cubes. It is the structure that is observed in Figure 4.31. Scanning electron micrographs are depicted in Figure 4.33. As seen in panel (b) the calculated von Mises stresses are not concentrated in one spot, but rather along the edges of the cube. When these cubes break during development, large parts near the edges are experiencing stresses close to the yield stress, resulting in large cracks that leave open holes. Again, the position of maximum von

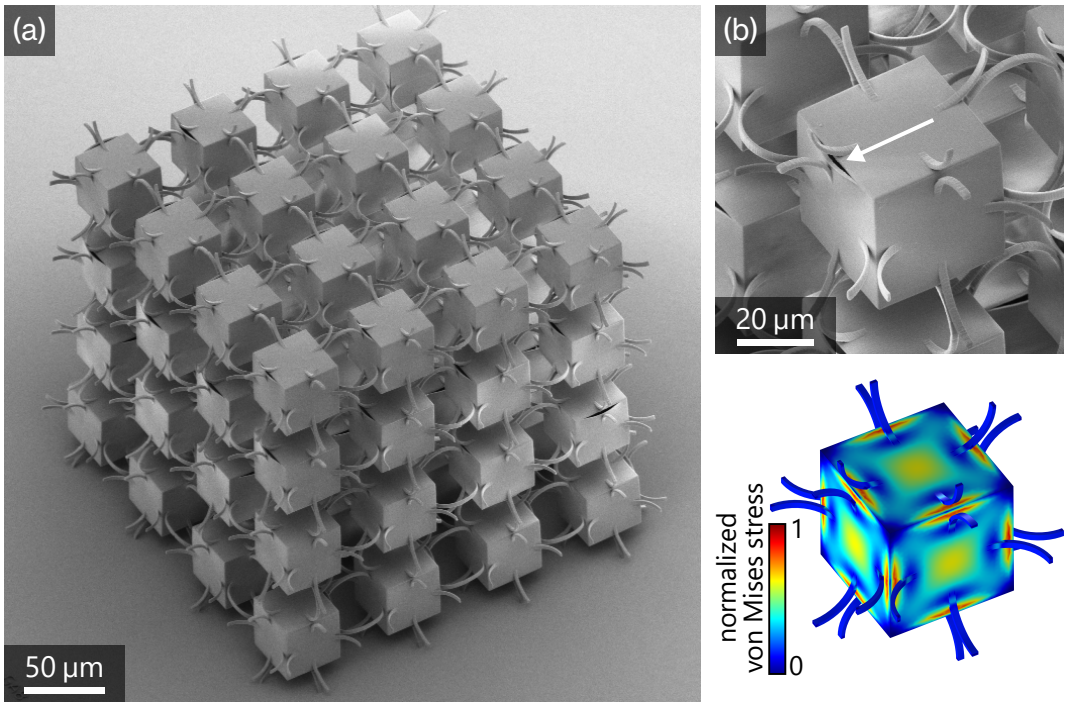

Figure 4.33: (a) Scanning electron micrograph of an unsuccessfully fabricated metamaterial based on a design similar to the one shown in Figure 4.22(a), but without the interior cubes sitting in each corner and a different arrangement of lever arms. (b) Magnified view, showing large openings along the edges of the hollow cubes. In the calculated von Mises stress distribution shown below, the maxima are not confined in a small spot, but rather extended along the edges of the cubes, causing the large openings during development.

Mises stresses calculated for an internal pressure increase fit well with the position of observed cracks.

This is why we have introduced smaller cubes at the corners inside the larger hollow cube for the designs of Figure 4.22. With increasing size c, the maximum von Mises stress moves away from the edges of the large cube towards the position, where the corner of the smaller cubes meets the membranes. We have fabricated $4 \times 4 \times 4$ unit cells of both the design for negative effective compressibility and the design for positive effective compressibility with a lattice constant of $a = 75\,\mu\text{m}$ and a membrane thickness of $t = 1.1\,\mu\text{m}$. Like before, the membrane thickness was reduced by $0.5\,\mu\text{m}$ along the axial direction to compensate for the aspect ratio. Other geometrical parameters were the same as for the numerical calculations, with absolute values of

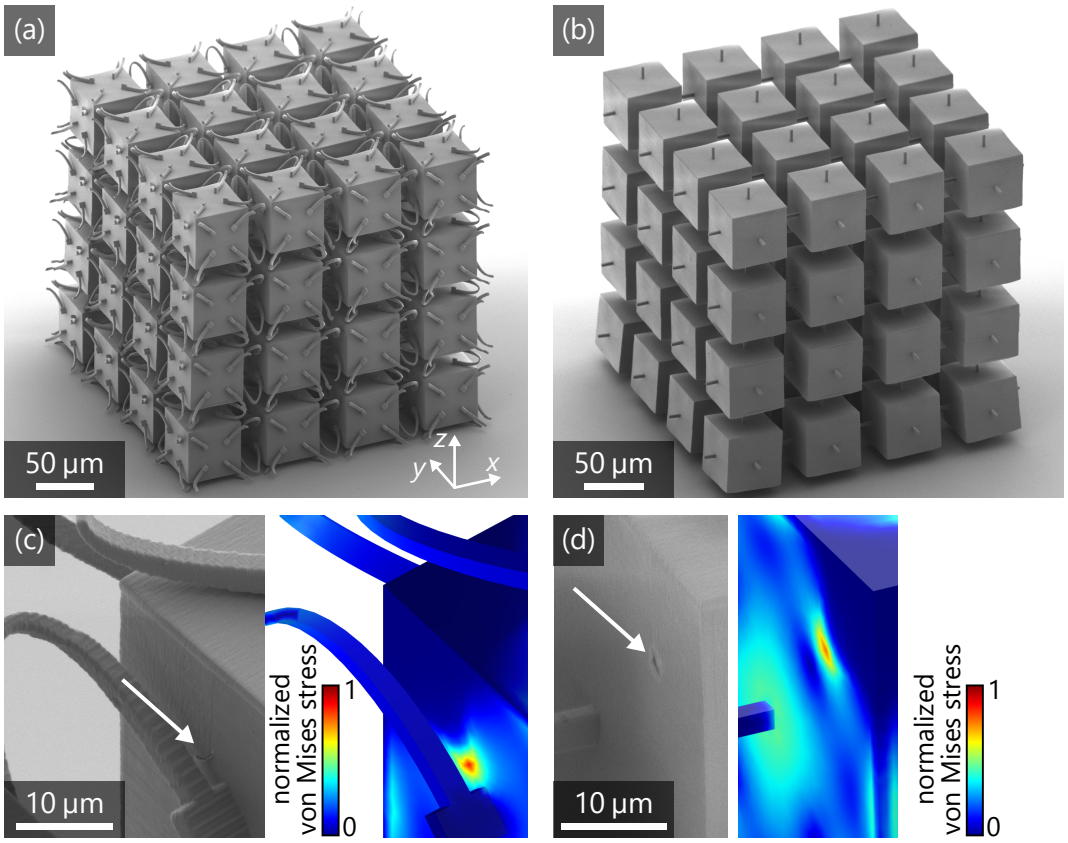

Figure 4.34: Scanning electron micrographs of a fabricated metamaterial structure consisting of $4 \times 4 \times 4$ unit cells designed with (a) $\kappa_{\text{eff}} < 0$ and (b) $\kappa_{\text{eff}} > 0$. It is based on the blueprints shown in Figure 4.22. (c) Magnified view of the sample shown in (a), zoomed in onto one of the small cracks that formed during the development process. The calculated von Mises stress distribution of the same section is depicted next to it. The maximum von Mises stress lies at the position where the crack occurred. (d) same as (c), but for the structure shown in (b). Adapted from Reference [84].

$b = 2.25\,\mu\text{m}$, $c = 11.25\,\mu\text{m}$, $d = 21.71\,\mu\text{m}$, $l = 52.5\,\mu\text{m}$ and $r = 9.75\,\mu\text{m}$. Electron micrographs of fabricated metamaterials are shown in Figure 4.34. The von Mises stresses are concentrated on the spot, where the corners of the inner cubes touch the membrane. As expected, these are the regions where small cracks occur during development.

Before measuring the effective compressibility of fabricated metamaterial structures, the question arises, whether the hollow volumes are really empty from liquid photoresist. We are able to confirm this under a widefield

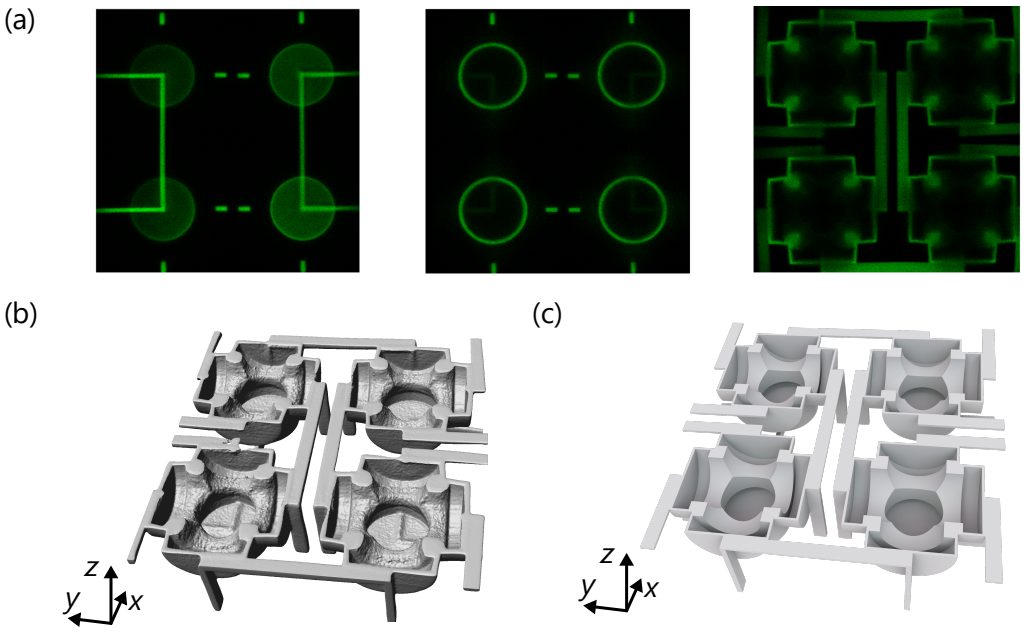

Figure 4.35: (a) Fluorescence images of different z-layers of one fabricated unit cell based on the design shown in Figure 4.24(b) (also compare Figure 4.32) acquired using a confocal laser scanning fluorescence microscope. (b) Cross-sectional view of a three-dimensional reconstruction calculated from the z-stack of fluorescence images taken. (c) Corresponding part of the unit cell cut out from the underlying three-dimensional blueprint of Figure 4.24. Adapted from Reference [83].

microscope because of the different refractive indices, but to be completely sure, we have examined one fabricated unit cell based on the blueprint in Figure 4.24 under a laser scanning fluorescence microscope (LSM510 META, Carl Zeiss AG) with an oil-immersion objective (Plan-Apochromat $63\times$ NA $= 1.4$, Carl Zeiss AG). Here, a droplet of immersion oil (Immersol 518 F, Carl Zeiss AG) is put directly onto the structure to minimize the refractive index mismatch. The written polymer and the liquid photoresist both exhibit significant autofluorescence [97]. In case the interior volumes are filled with liquid photoresist, the laser scanning fluorescence microscope would observe bright fluorescence inside, while empty interior volumes would not fluoresce.

Selected fluorescence images for different z-positions are depicted in Figure 4.35(a), showing the top part of the unit cell (left), cylindrical part of the

crosses (middle) and the center of the crosses (right). A cross-sectional view of the three-dimensional model obtained from the fluorescence data, represented as an iso-intensity surface, is depicted in Figure 4.35(b). The hollow interior structure of the crosses is clearly visible, which means that there is no residual photoresist inside. To compare the data, the corresponding part of the three-dimensional model (see Figure 4.24) is depicted in panel (d). As expected, the interior structures look very similar.

4.2.5 Static Measurements

As it was just demonstrated, we have successfully fabricated different poroelastic metamaterials that include hollow interior volumes. To test if these hollow volumes are actually airtight, we first compare both fabricated metamaterials depicted in Figure 4.32. One has presumably sealed and airtight hollow crosses, while the other has deliberately introduced holes in each cross and is, therefore, not airtight.

To measure the effective compressibility, the samples are put inside the pressure chamber (see Section 3.3). The air pressure inside the chamber is increased stepwise from $P_0 = 1\,\mathrm{bar}$ to a maximum pressure of $P = P_0 + \Delta P = 4.8\,\mathrm{bar}$ in less than 30 s. At each pressure step, one picture is taken after the pressure has stabilized (takes about 2 s) and the relative length change $\Delta L/L$ is measured via image cross-correlation. For $\Delta L/L \ll 1$, the relative effective volume change is obtained via $\Delta V_{\mathrm{eff}}/V_{\mathrm{eff}} \approx 3\Delta L/L$ and the effective compressibility

$$\kappa_{\mathrm{eff}} \approx -\frac{3}{L}\frac{\Delta L}{\Delta P} \tag{4.10}$$

can be calculated.

Measured relative length changes averaged in the xy-plane are plotted over the overpressure ΔP in Figure 4.36. For the sample with sealed crosses (blue points), the length change increases linearly with a relative length change of over 1 % at maximum overpressure. Here, we have also measured the behavior under decreasing pressure after reaching maximum overpressure (dark blue circles) and observe no hysteresis, suggesting that most of the crosses are actually airtight. From this length change we calculate a large negative effective compressibility of $\kappa_{\mathrm{eff}} = -0.8\,\%/\mathrm{bar}$.

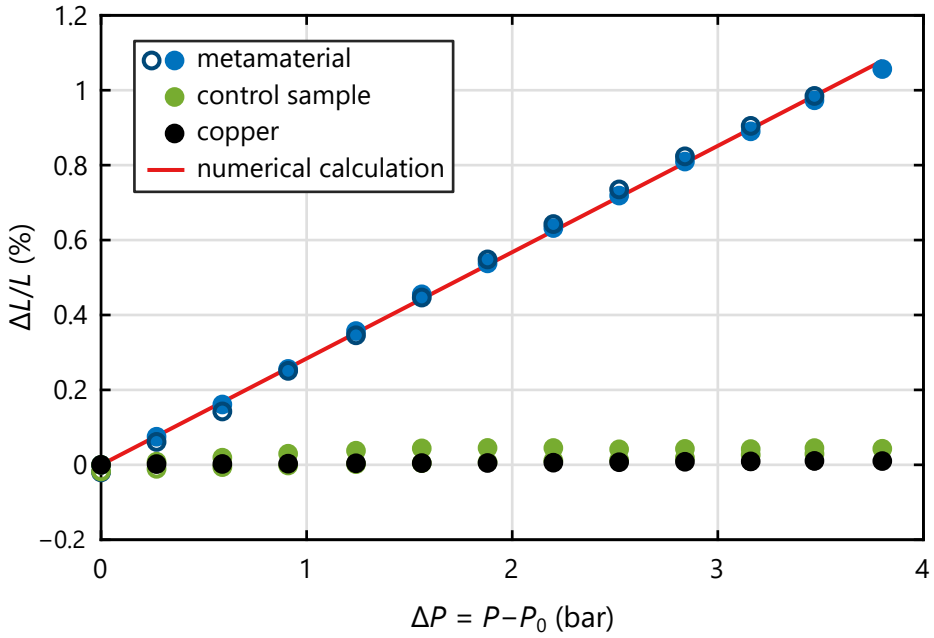

Figure 4.36: Relative length change with respect to applied overpressure ΔP. Full dots are measured during pressure increase, circles are measured during pressure decrease. The blue data points are taken on a metamaterial sample (see Figure 4.32(a)). The observed length increase corresponds to a negative effective compressibility of $-0.8\,\%/\text{bar}$. The same measurement on a control structure with intentional holes introduced into each cross (see Figure 4.32(c)) and on a piece of copper are shown in green and black, respectively. The red line is calculated numerically with the following parameters: $t/a = 1.15\,\%$, $r/a = 12\,\%$, $b/a = 1.5\,\%$, $c/a = 4\,\%$, $l/a = 38\,\%$, $E = 3\,\text{GPa}$, and $\nu = 0.4$. Adapted from Reference [83].

Figure 4.37(a) shows the displacement vectors with respect to their mean position (compare Figure 4.14) that correspond to the blue point at the largest overpressure $\Delta P = 3.8\,\text{bar}$ in Figure 4.36. All arrows point outwards, demonstrating a very homogeneous expansion in the xy-plane.

It is, of course, important to check, whether the sample also expands in the z-direction. Therefore, we have performed the same measurement on the same sample, but turned by 90° to image the xz-plane. An image taken at $\Delta P = 3.8\,\text{bar}$ is depicted in Figure 4.37(b). The displacement vectors are calculated with respect to the glass substrate on the bottom. As the bottom layer is fixed to the substrate, the bottom unit cells can hardly move

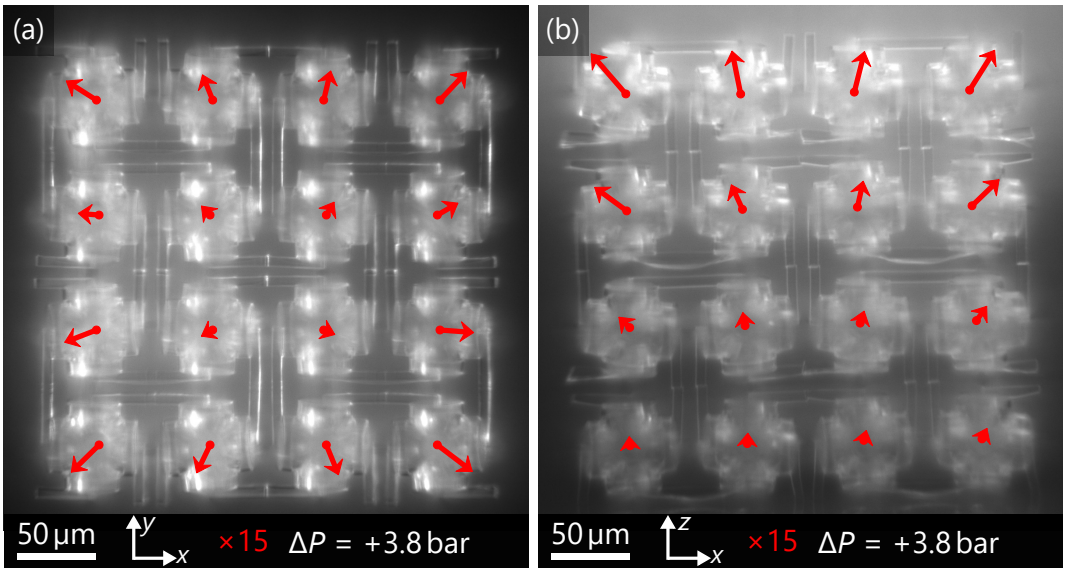

Figure 4.37: Displacement vectors calculated from measured images using image cross-correlation on a metamaterial composed of $2 \times 2 \times 2$ unit cells (compare Figure 4.32(a)) under a pressure increase of $\Delta P = 3.8\,\text{bar}$ superimposed onto (a) top view and (b) side view of the poroelastic metamaterial. The arrows indicate a large negative effective compressibility. From the vectors in (a) we derive $\kappa_{\text{eff}} = -0.8\,\%/\text{bar}$. For the control structure that exhibits holes inside each hollow cross, the displacement vectors are smaller than the small red circles in the middle of each cross. All arrows have been scaled by the indicated factors. Adapted from Reference [83].

sidewards, which is why the arrows there mainly point upwards. This boundary effect vanishes at the second layer of unit cells (third and forth layer of crosses from the bottom), which exhibit ordinary bulk behavior like in panel (a).

This result is compared with numerical calculations. We have seen in Figure 4.23(f) that κ_{eff} strongly depends on the membrane thickness t/a, which is simultaneously the parameter most difficult to control during DLW. Therefore, we choose t/a as a fit parameter and otherwise same parameters as in Figure 4.24. With material parameters of $E = 3\,\text{GPa}$ and $\nu = 0.4$ and a thickness of $t/a = 1.15\,\%$ we reproduce the metamaterial behavior numerically (red line in Figure 4.36). This thickness is 675 µm larger than the thickness $t/a = 0.7\,\%$ used as an input value for fabrication. However, due to the finite voxel size, fabricated membranes thicknesses are larger than the input values. A lateral voxel size of 500 nm is not unusual for the

exposure powers we use. Sample imperfections (see Figure 4.37) are another source for deviations. All in all, the numerical values are consistent with the experiments within the fabrication errors.

During the same measurement of the metamaterial sample with holes in each cross there is no difference between the interior pressure and the surrounding chamber pressure and the membranes do not warp. As a result, nearly zero relative length change is measured (green points in Figure 4.36). We obtain the same result for a piece of copper (black points in Figure 4.36).

Strictly speaking, we would expect to measure a small negative length change caused by the positive bulk material compressibilities. For the larges pressure increase $\Delta P = 3.8\,\text{bar}$ the relative length change is expected to lie in the order of -10^{-5} for the metamaterial with holes and around -9×10^{-7} for copper (see Section 3.3.5). Instead we measure small positive relative length changes of 1.0×10^{-4} and 4.3×10^{-4}, respectively. For copper, this has been explained as an artifact of the measurement setup due to warping of the chamber window in Section 3.3.5. The magnitude of this optical effect is about two order of magnitudes smaller than the effective metamaterial compressibilities and therefore negligible. On top of this measurement artifact, the metamaterial with holes showed an additional length increase. We attribute this to absorption of gas, which causes a swelling of the bulk polymer under pressure. For CO_2, this swelling effect is even larger as we will see later.

In Figure 4.23, the membrane thickness t has been identified as one of the parameters with the largest influence on the effective compressibility. We also want to reproduce this trend experimentally and have fabricated and measured three additional samples with the same parameters as for the sample measured in Figure 4.36, three samples with a reduced membrane thickness of $\Delta t = -0.2\,\mu\text{m}$, and three more samples with an increased thickness of $\Delta t = +0.2\,\mu\text{m}$. Measured effective compressibilities are plotted over Δt in Figure 4.38. They demonstrate the anticipated trend of larger modulus of negative effective compressibility for thinner membranes. A difference of $0.4\,\mu\text{m}$ in membrane thickness changed the effective compressibility by a factor of three.

Large Negative or Positive Effective Compressibility

We were able to obtain even larger effects with the simplified simple-cubic unit cell design. The relative length change of nominally identical samples

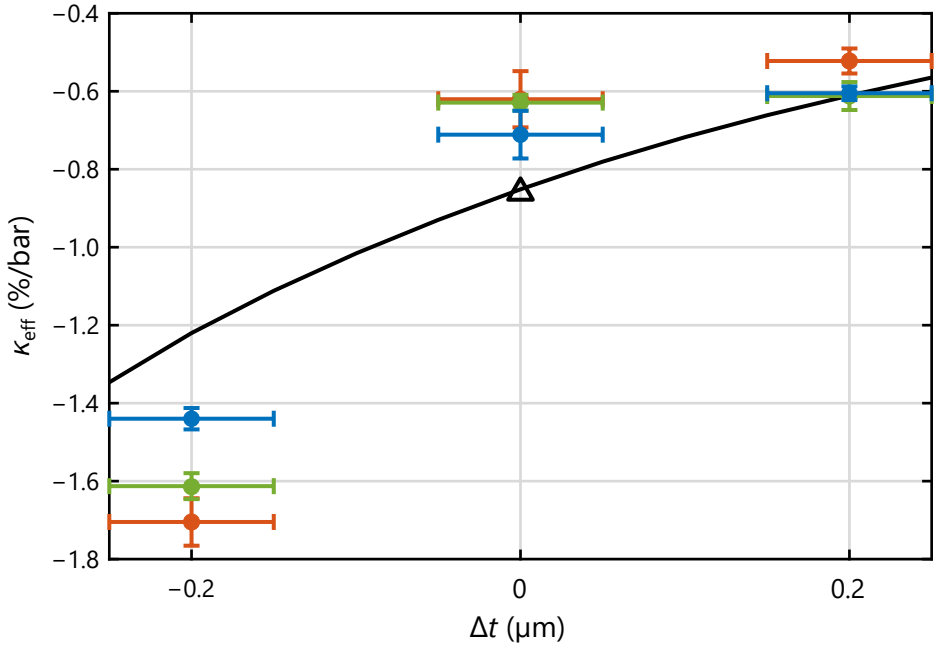

Figure 4.38: Effective compressibility with respect to a change in membrane thickness Δt and otherwise identical parameters as in Figure 4.36. The dots are calculated from measured displacement data. Different colors at each Δt represent different samples fabricated with nominally identical parameters. All horizontal error bars are estimated, vertical error bars are $\pm 3\sigma$ calculated from 10 measurements taken on one sample. The black triangle is derived from the blue points in Figure 4.36. The solid black line is calculated numerically (Δt corresponds to a lattice constant of $a = 150\,\mu\mathrm{m}$). Adapted from Reference [83].

as shown in Figure 4.34 has been measured with the same process as before. Results are plotted in Figure 4.39. There, we have observed unusually large length changes of $\Delta L/L = 5\,\%$ for the sample with negative effective compressibility (panel (a)) and $\Delta L/L = -5\,\%$ for the sample with positive effective compressibility (panel (b)) at a maximum pressure increase of $\Delta P = 3.8\,\mathrm{bar}$. The slopes are initially linear, which we have reproduced with numerical calculations in the linear regime (black line). From the initial slopes we derived an effective compressibility of $\kappa_{\mathrm{eff}} = -4.7\,\%/\mathrm{bar}$ and $\kappa_{\mathrm{eff}} = 5.0\,\%/\mathrm{bar}$ for Figure 4.39(a) and (b), respectively.

As the absolute values $|\kappa_{\mathrm{eff}}|$ are much larger than in Figure 4.36, geometrical nonlinearities are not negligible any more. At large pressures we observe

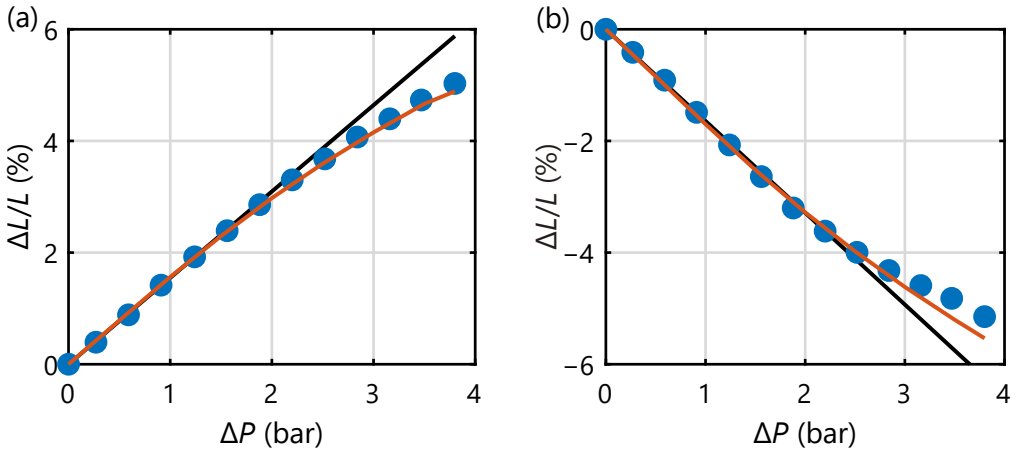

Figure 4.39: Relative length change versus hydrostatic pressure increase measured via image cross-correlation (blue dots). (a) Metamaterial as shown in Figure 4.34(a) with a large negative effective compressibility of $\kappa_{\text{eff}} = -4.7\,\%/\text{bar}$. (b) Metamaterial designed for $\kappa_{\text{eff}} > 0$ as shown in Figure 4.34(b) demonstrating large positive effective compressibility of $\kappa_{\text{eff}} = 5.0\,\%/\text{bar}$. The black lines are numerical calculation in the linear regime as in Figure 4.25 with $t/a = 1.76\,\%$ and $t/a = 1.78\,\%$ for (a) and (b), respectively. The red curves are the same calculations but including geometrical nonlinearities. Adapted from Reference [84].

significant deviations between the measured data and the linear calculations, starting at around $\Delta P = 2\,\text{bar}$ or $\Delta L/L = 3\,\%$. Therefore, we have also included numerical calculations that consider geometrical nonlinearities (red curves). Apart from that, they are identical to the linear calculations. Clearly, the red curves fit much better to the experimental data.

For the largest pressure changes, the length changes are easily visible on the microscopic images. In Figure 4.40, we have put optical micrographs of the samples as shown in Figure 4.34 taken at $\Delta P = 0\,\text{bar}$ and $\Delta P = 3.8\,\text{bar}$ side by side. Panel (a) and (b) show the sample with $\kappa_{\text{eff}} < 0$ (see Figure 4.40(a)) and a clear expansion at increased pressure can be seen. Panel (c) and (d) show the sample with $\kappa_{\text{eff}} > 0$ (see Figure 4.40(b)) and a shrinkage is observed. The magnitudes are quantified with image cross-correlation. One ROI of 121×121 pixels is chosen in the middle of each cube. These displacement vectors are used to calculate the largest length changes plotted in Figure 4.39.

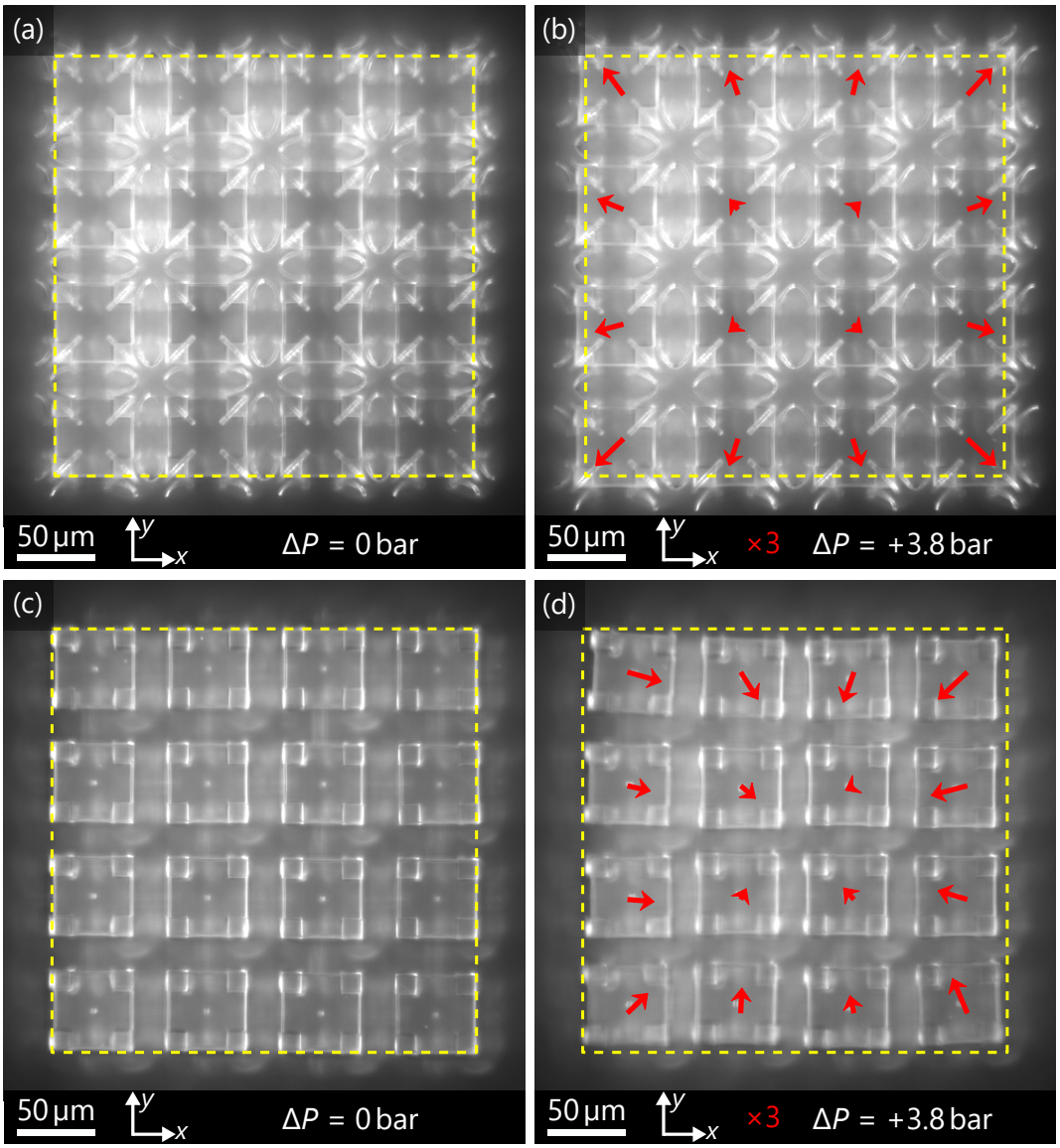

Figure 4.40: Optical micrographs of the fabricated metamaterial shown in Figure 4.34(a) taken at (a) reference pressure $P_0 \approx 1\,\text{bar}$ and (b) under a pressure increase of $\Delta P = 3.8\,\text{bar}$. The dashed yellow box marks the outer edges of the cubes in (a). The same box is put in (b) to visualize the change in size. Red arrows are calculated with image cross-correlation. They are scaled with a scaling factor of three. (c) and (d) depict the same as (a) and (b), but for a fabricated metamaterial as shown in Figure 4.34(b). A clear shrinkage is observed in (d). Adapted from Reference [84].

4.2.6 Gas Permeation Through Polymer Membranes

The lack of hysteresis in Figure 4.36 suggests that the sealed hollow volumes can be considered as airtight for at least the measurement time. To quantify the time constant, we have measured $\Delta L/L$ of the same metamaterial as in Figure 4.36 over time. The results are shown in Figure 4.41 (blue points). At $t = 0$ the chamber pressure is increased from $P_0 \approx 1\,\text{bar}$ to $P = P_0 + 3.8\,\text{bar}$ and a relative length change of $\Delta L/L \approx 1\,\%$ is observed. Afterwards the chamber pressure is held constant at $\Delta P = 3.8\,\text{bar}$ and $\Delta L/L$ is monitored over time. After one hour the metamaterial has relaxed back to its initial state with $\Delta L/L = 0$. At this point the sealed hollow volumes have accommodated to the increased chamber pressure. The chamber pressure is now abruptly decreased to the initial value P_0 while the hollow volumes still are at increased pressure, which warps the membrane outwards. The mechanism is effectively reversed and we observe a negative relative length change of $\Delta L/L \approx -1\,\%$ that decays back to zero with approximately the same time constant. From the exponential fits (red curves), a time constant of $\tau_{\text{air}} = 745\,\text{s} = 12.4\,\text{min}$ is derived, much longer than the measurement time for Figure 4.36.

One possible reason for the pressure compensation over time could be cracks that are not completely airtight, which causes air flows through the remaining holes. Assuming laminar flow and small circular holes with radius r_h and a length equal to the L, the air flow is described by the Hagen–Poiseuille equation. For compressible fluids it reads:

$$Q = \frac{\dot{n}RT}{P_\text{c}} = \frac{\pi r_\text{h}^4 (P_\text{i} - P_\text{c})}{8\mu L} \left(\frac{P_\text{i} + P_\text{c}}{2P_\text{c}} \right) . \tag{4.11}$$

Q is the volume flow at chamber pressure P_c, P_i is the pressure inside the hollow volumes and μ is the viscosity of the fluid or gas. The dependence on r_h^4 stands out immediately and quantitative calculations (see Appendix A) reveal that r_h has to be in the order of 10 nm to explain the observed time constant. Since the remaining holes would be a result of the rather erratic cracking and resealing process during development, fluctuations in their size would cause large differences in the time constant between samples. If r_h differs by a factor of two, the time constants are expected to differ by a factor of 16. This is not the case, as time constants on the same order of magnitude were measured on different samples (compare Figure 4.42). As a result, we assume the majority of the cracks to be properly sealed and our explanation

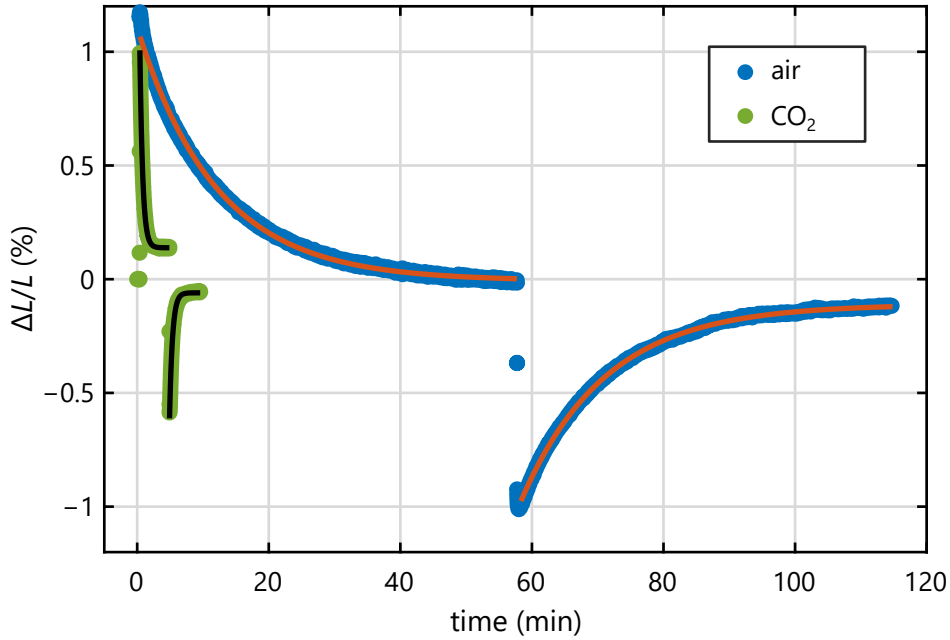

Figure 4.41: The relative length change $\Delta L/L$ of the metamaterial shown in Figure 4.37 is measured over time to determine the time constant of gas permeation through the membranes of the crosses. At $t = 0$, the chamber pressure is increased from ambient atmospheric pressure $P_0 \approx 1\,\text{bar}$ to $P = P_0 + 3.8\,\text{bar}$ and then held constant. $\Delta L/L$ shows an exponential decay. After $\Delta L/L$ has reached a nearly constant value, the chamber pressure is decreased to P_0. This results in a reversed effect and a second decay is measured. Red and black curves are exponential fits. If the chamber is pressurized with air (blue points) we derive a time constant of $\tau_{\text{air}} = 745\,\text{s}$. For CO_2 (green points) the decay is significantly faster, with a time constant of $\tau_{CO_2} = 26\,\text{s}$. Adapted from Reference [83].

for the exponential decay of $\Delta L/L$ over time is permeation of air through the membranes, just like for the solvent during development (see Figure 4.31).

Permeation includes different processes that lead to a particle flow through the a membrane like diffusion, sorption and desorption. The substance flow $\dot{n}$ can be calculated via an equation similar to Fick's first law:

$$\dot{n} = \frac{kA(P_\text{i} - P_\text{c})}{\mu L} \,. \tag{4.12}$$

It depends on the permeability k, which depends strongly on the type of

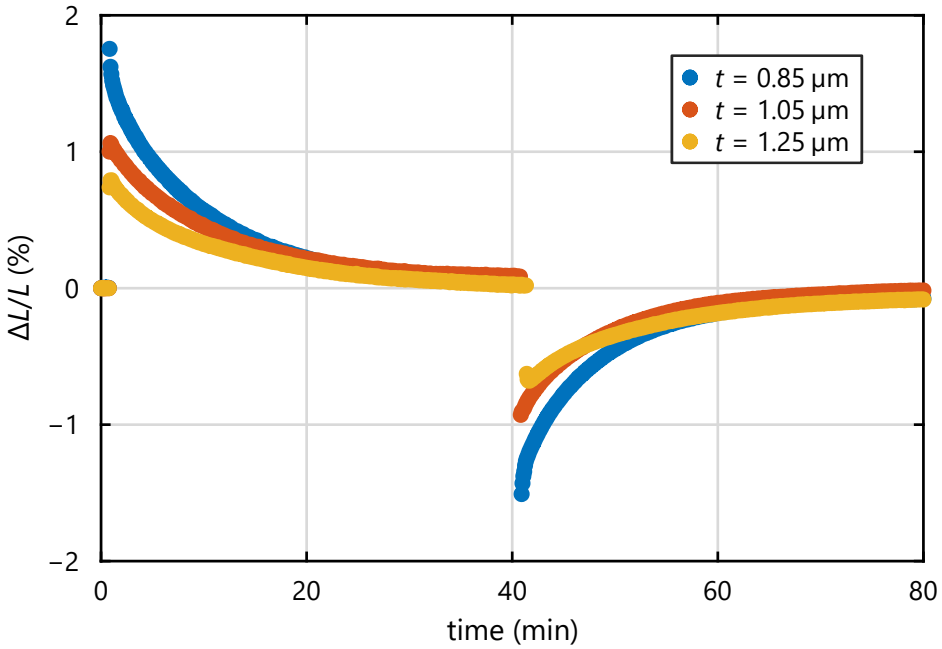

Figure 4.42: Decay of the relative length change over time as shown in Figure 4.41, but for samples with different membrane thicknesses t (see Figure 4.38). The numerical input values for t are listed in the legend. From exponential fits, time constants of $\tau_{0.85} = 492\,\mathrm{s}$, $\tau_{1.05} = 556\,\mathrm{s}$ and $\tau_{1.25} = 669\,\mathrm{s}$ are obtained for samples with numerical input values of $t = 0.85\,\mu\mathrm{m}$, $t = 1.05\,\mu\mathrm{m}$ and $t = 1.25\,\mu\mathrm{m}$, respectively. As expected from Equation 4.12, the decay times decrease for thinner membranes.

gas or liquid that permeates through the membranes. In literature, the ratio k/μ, which is another measure for permeability, is often quoted in the units 1 barrer $\approx 3.346 \times 10^{-16}\,\mathrm{mol\,m/(s\,m^2\,Pa)}$ [98]. It is connected to the diffusivity D (in units $\mathrm{m^2/s}$) and the solubility S (in units $\mathrm{mol/(m^3\,Pa)}$) via $k/\mu = DS$ [99].

For many polymers the value for CO_2 it is often more than one order of magnitude higher than for N_2, caused by the high solubility of CO_2 [100–103]. Therefore, we have repeated the same measurement on the same sample, but pressurized the chamber with CO_2. This is plotted in green in Figure 4.41. As expected, the decay times are significantly shorter. The exponential fits for CO_2 (black curves) give a time constant of $\tau_{CO_2} = 26\,\mathrm{s}$. At the end of the first decay, $\Delta L/L$ approaches a plateau, which we explain with solution of CO_2 into the bulk polymer that causes a swelling. We have seen a similar

swelling behavior with lower magnitude for the control sample pressurized with air in Figure 4.36.

For the measured time constants of τ_{CO_2} and τ_{air} in Figure 4.41 we calculate $k/\mu = 0.02\,\text{barrer}$ for air and $k/\mu = 0.6\,\text{barrer}$ for CO_2 (see Appendix A). Compared to the range of values reported in literature [101, 104], these are even rather low permeabilities. Also, the fact that they lie more than one order of magnitude apart is another confirmation that the observed pressure equalization over time is caused by permeation rather than Poiseuille flow through a hole. For the latter, the only variable that depends on the type of gas is the dynamic viscosity, which does not depend on pressure for ideal gases [105]. As the dynamic viscosities of air ($\mu = 18.5\,\mu\text{Pa s}$) and CO_2 ($\mu = 15\,\mu\text{Pa s}$) [106] have a relative difference of only about 20 %, they can not explain the observed time constants.

Also O_2 has usually a higher permeability than N_2 [102], which could be the reason, why the single exponential fits in Figure 4.41 does not fit the blue data points (air) well at the beginning of the decay. For air, which for the most part consists of 78 % N_2 and 21 % O_2, two exponential decay times are expected.

In summary, the time dependent measurements of $\Delta L/L$ have shown that the cracks we have seen in Figure 4.32(b) are resealed and airtight. The observed exponential decay is a result of gas permeation through the polymer. Just by observing $\Delta L/L$ we were able to measure the permeability and distinguish between different gases.

5 Chapter 5 Conclusion

In this thesis, I have explored the possibility of tailoring thermal expansion and effective compressibility with a metamaterial to lie outside range of its constituents.

The fundamentals were covered in Chapter 2, which included an introduction to thermodynamics and continuum mechanics. It was shown that the static compressibility can not become negative in thermodynamic equilibrium. From the field of poroelasticity the effective (or unjacketed) compressibility was introduced, which, in contrast, can become negative. In Section 2.3 bounds of material properties were discussed and the reason, why most materials have positive thermal expansion was explained.

The methods were introduced Chapter 3, including an overview of the fabrication method direct laser writing, a brief explanation of the finite-element method with COMSOL Multiphysics, and a description of the measurement setup. The measurement method image cross-correlation was explained and demonstrated thoroughly.

With these methods it was possible to measure the thermal expansion coefficient of copper, which was done as a benchmark. Moreover, a small systematic magnification error during pressure controlled measurement was identified and quantified. It was caused by pressure induced warping of the glass window on top of the pressure chamber.

The main results of this work were summarized in Chapter 4. In Section 4.1.1, I have introduced different two-component metamaterial designs used to tailor the effective thermal expansion coefficient. Instead of complicated multi-step fabrication with two different photoresists, I have demonstrated the ability to fabricate multi-component structures with one photoresist. With the exposure laser power as the adjustment parameter I have shown that it is possible to tune the thermal expansion coefficient of the polymerized material from about $5 \times 10^{-5}\,\mathrm{K}^{-1}$ to $8 \times 10^{-5}\,\mathrm{K}^{-1}$.

With this ability, two-component metamaterials were fabricated in only one writing step and a negative effective thermal expansion coefficient of $\alpha_{\text{eff}} = (-5 \pm 0.5) \times 10^{-5}\,\text{K}^{-1}$, as well as a near zero effective thermal expansion coefficient of $\alpha_{\text{eff}} = (0 \pm 0.5) \times 10^{-5}\,\text{K}^{-1}$ were obtained. The measurement method with image cross-correlation enabled us to observe the principle of operation as well, demonstrating that the crosses rotate in the expected directions.

Fabrication of the metamaterial design for large positive thermal expansion has proven to be rather challenging, due to the fact that the pre-bending of the beams causes a large positive shrinkage during sample development. In earlier experiments, this has always resulted in touching parts, that canceled the effect. Nevertheless, fabrication was successful eventually by precompensating the shrinkage and a large positive effective thermal expansion coefficient of $\alpha_{\text{eff}} = (+12 \pm 0.5) \times 10^{-5}\,\text{K}^{-1}$ was obtained. In the end of Section 4.1, also an anisotropic metamaterial was fabricated and measured, showing effective thermal expansion coefficients of $\alpha_{\text{eff},\,x} = (-4 \pm 0.5) \times 10^{-5}\,\text{K}^{-1}$ along the x-axis and $\alpha_{\text{eff}} = (+15 \pm 0.5) \times 10^{-5}\,\text{K}^{-1}$ along the y-axis. With such a high thermal expansion control, these thermoelastic metamaterials can become a promising candidate to protect sensitive instruments from thermally induced stresses.

The results on poroelastic metamaterials were presented in Section 4.2. I have introduced novel designs that employ sealed hollow volumes to obtain very large negative or positive effective compressibilities. In Section 4.2.2 the unit cells were analyzed with finite-element calculations, which showed that the membrane thickness has the largest influence on the metamaterial effect. Additionally, the difference between air filled and evacuated hollow volumes was quantified. On the dynamic behavior, the sign of the effective compressibility did not show any significant influence. We have contributed this to the small ratio of $|\kappa_{\text{eff}}/\kappa_{\text{j}}|$.

In Section 4.2.4 it was shown, that the the sealed liquid photoresist is dissolved from the fabricated hollow volumes through cracks that occur due to osmotic pressure increase. By designing the structure in such a way that the von Mises stresses during pressure increase are confined in a small region, I have succeeded in fabricating empty hollow volumes that are airtight. The emptiness has been confirmed by confocal laser scanning microscopy while measurements of the effective compressibility over time has proven that the hollow volumes are airtight and that the observed decay times are due to gas permeation through the membranes.

Experimentally, positive and negative effective compressibilities as large as $-4.7\,\%/\mathrm{bar}$ and $5.0\,\%/\mathrm{bar}$ were obtained (Section 4.2.5), making the deformations easily visible just by looking at the sample images. In future, the large length changes of poroelastic metamaterials could be used to build actuators, for example, in programmable metamaterials [107–110], or soft robotics [111] with the surrounding air pressure as an external stimulus.

Appendix A

A Time Constants

Estimation of Hole Radius

We roughly estimate the radius r_h of a circular hole inside the membrane to explain the time constant $\tau_{air} = 745\,s$ of the decay shown in Figure 4.41 (blue points) with the Hagen-Poiseuille equation

$$\frac{\dot{n}RT}{P_c} = \frac{\pi r_h^4 (P_i - P_c)}{8\mu L}\left(\frac{P_i + P_c}{2P_c}\right) . \tag{A.1}$$

In the case of small pressure differences, we can approximate

$$\frac{P_i + P_c}{2P_c} \approx 1 , \qquad V_i = \text{const.} . \tag{A.2}$$

With $\dot{n} = \dot{P}_i V_i/(RT)$ we obtain a differential equation

$$\dot{P}_i = \frac{\pi r_h^4 P_c}{8\mu L V_i}(P_i - P_c) , \tag{A.3}$$

which has a known solution

$$P_i(t) = P_c + (P_i(0) - P_c)\exp\left(-\frac{\pi r_h^4 P_c}{8\mu L V_i}t\right) , \tag{A.4}$$

and hence a time constant of

$$\tau = \frac{8\mu L V_i}{\pi r_h^4 P_c} \tag{A.5}$$

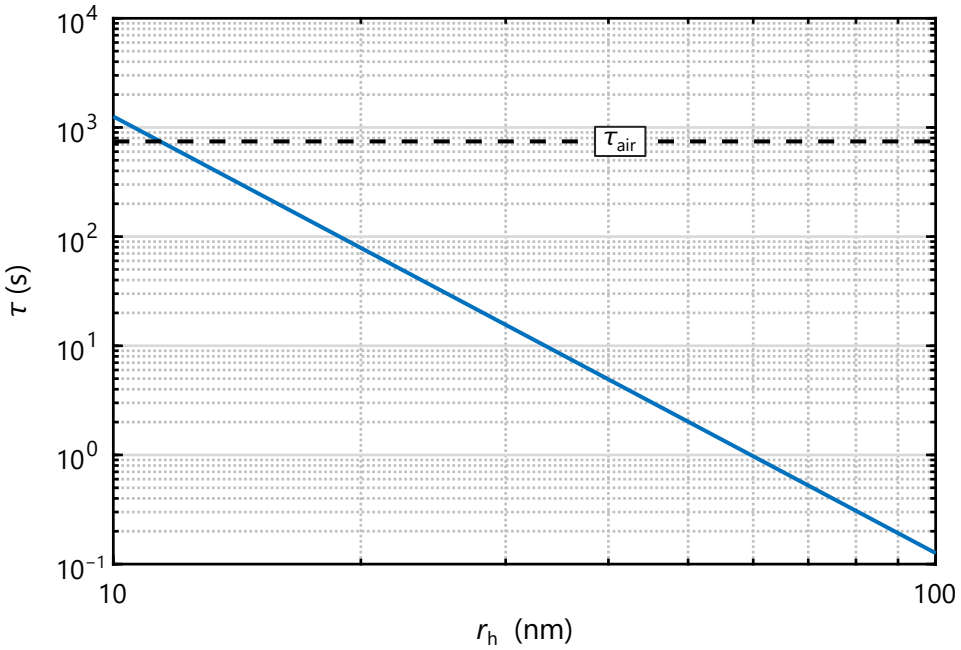

Figure A.1: Time constant τ of pressure equalization versus hole radius r_h in double-logarithmic scale. Measured time constant in Figure 4.41 for air is shown as a dashed line. The lines cross at $r_h = 11.4\,\text{nm}$.

For $\tau = \tau_{air}$ we insert all constants (listed in Table A.1) and obtain a hole radius of $r_h = 11.4\,\text{nm}$.

Until now, we have assumed small pressure differences. For the maximum pressure difference at the start of the measurement in Figure 4.41, the calculations have an additional factor $(P_i + P_c)/(2P_c) \approx 0.6$. Including this factor, the calculated hole radius has a similar value of $r_h = 13.0\,\text{nm}$.

Estimation of Permeabilities

We have explained the decay shown in Figure 4.41 with permeation of gas through the membranes. Here, we calculate the permeabilities that correspond to the measured time constants. From Equation 4.12 we obtain

$$\dot{P}_i = \frac{kART}{V_i \mu L}(P_i - P_c)\ . \tag{A.6}$$

Parameter	Value	Description
V_i	74080 µm^3	volume of hollow interior
A	9776 µm^2	effective membrane area
L	1.725 µm	hole length or membrane thickness
τ_{air}	745 s	measured time constant for air
τ_{CO_2}	26 s	measured time constant for CO_2
P_c	4.8×10^5 Pa	chamber pressure
R	8.314 J/(mol K)	ideal gas constant
μ	18.5 µPa s	dynamic viscosity of air
T	296.15 K	room temperature

Table A.1: Constants used for calculations in this chapter. They correspond to the three-dimensional cross shown in Figure 4.24 and the measurement shown in Figure 4.41.

The time constant is

$$\tau = \frac{V_i \mu L}{kART} \tag{A.7}$$

For the measured time constants in Figure 4.41 and the constants are listed in Table A.1, we obtain permeabilities of $k/\mu = 0.02$ barrer for air and $k/\mu = 0.6$ barrer for CO_2.

B Appendix B
Primitive Unit Cells

Here, we show possible primitive unit cells for the design shown in 4.2. If the unit cell is repeated in a cubic translational lattice, there is additional translational invariance along the space diagonals $(\pm a/2, \pm a/2, \pm a/2)^T$. Therefore, the Wigner–Seitz cell is is a truncated octahedron, as shown in Figure B.1, and the one shown in 4.2 is a bcc unit cell consisting of two primitive unit cells. However, the structure inside the truncated octahedron contains lots of disconnected parts, making the Wigner–Seitz cell unsuitable to describe the metamaterial with.

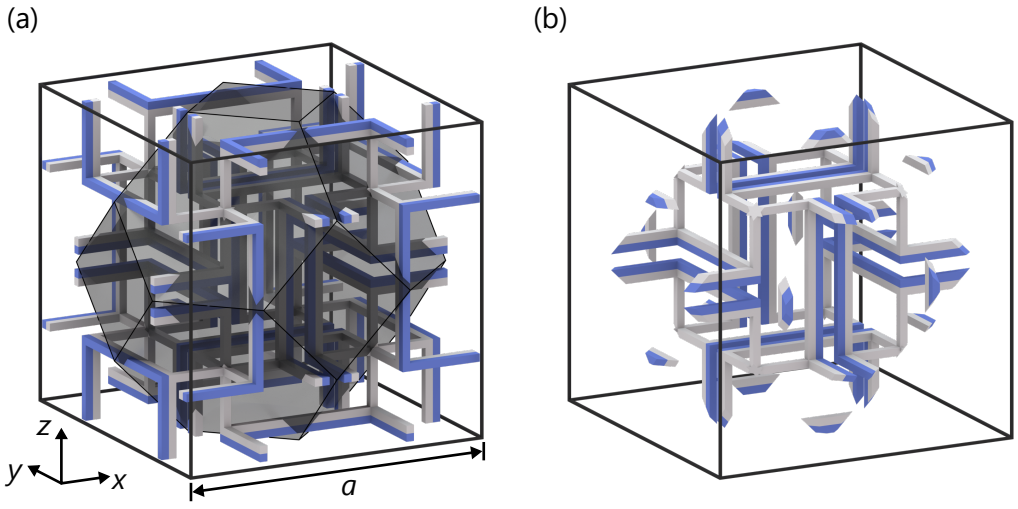

Figure B.1: (a) Unit cell as shown in Figure 4.2 with a truncated octahedron indicating the Wigner–Seitz cell. (b) Wigner–Seitz cell obtained by intersecting the unit cell with the truncated octahedron.

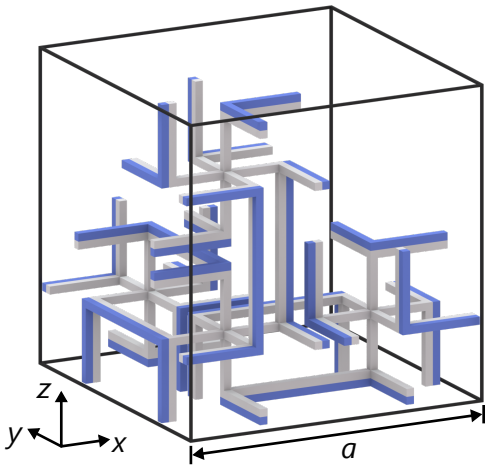

Figure B.2: Primitive unit cell containing four of the eight octants in Figure 4.2.

A possible primitive unit cell, that is connected, is shown in Figure B.2. It consists of four of the eight octants, one along each space diagonal, of the unit cell shown in Figure 4.2. However, it is rather asymmetric.

Bibliography

[1] P. Song and S. Hwang, "Mechanical properties of high-strength steel fiber-reinforced concrete", Constr. Build. Mater. **18**, 669–673 (2004) (Cited on page 3).

[2] T. Koschny, C. M. Soukoulis, and M. Wegener, "Metamaterials in microwaves, optics, mechanics, thermodynamics, and transport", J. Opt. **19**, 084005 (2017) (Cited on pages 4, 32).

[3] G. Dolling, M. Wegener, C. M. Soukoulis, and S. Linden, "Negative-index metamaterial at 780 nm wavelength", Opt. Lett. **32**, 53–55 (2007) (Cited on pages 4, 32, 33).

[4] G. W. Milton and A. V. Cherkaev, "Which elasticity tensors are realizable?", J. Eng. Mater. Technol. **117**, 483–493 (1995) (Cited on page 4).

[5] G. W. Milton, *The theory of composites* (Cambridge University Press, Cambridge, UK, 2002) (Cited on pages 4, 23, 25, 32).

[6] R. Lakes, "Cellular solids with tunable positive or negative thermal expansion of unbounded magnitude", Appl. Phys. Lett. **90**, 221905 (2007) (Cited on pages 4, 35).

[7] L. E. Reichl, *A modern course in statistical physics* (John Wiley & Sons, 2016) (Cited on pages 7, 8, 12, 15, 38).

[8] W. S. Slaughter, *The linearized theory of elasticity* (Birkhäuser, Boston, 2002) (Cited on pages 7, 20–22).

[9] F. Schwabl, *Statistische Mechanik*, 3., aktualisierte Aufl., Springer-Lehrbuch (Springer, Berlin, 2006) (Cited on pages 15, 34).

[10] M. Kadic, T. Bückmann, R. Schittny, and M. Wegener, "Metamaterials beyond electromagnetism", Rep. Prog. Phys. **76**, 126501 (2013) (Cited on pages 23, 32).

[11] B. Das, *Problems and Solutions in Thermoelasticity and Magneto-thermoelasticity*, SpringerLink : Bücher (Springer, Cham, 2017) (Cited on page 24).

[12] M. A. Biot, "Thermoelasticity and irreversible thermodynamics", J. Appl. Phys. **27**, 240–253 (1956) (Cited on pages 25, 27).

[13] M. A. Biot, "Theory of propagation of elastic waves in a fluid-saturated porous solid. I. Low-Frequency Range", J. Acoust. Soc. Am. **28**, 168–178 (1956) (Cited on pages 25, 30, 31, 102).

[14] M. Biot and D. Willis, "The Elastic Coefficients of the Theory of Consolidation", J. Appl. Mech. **24**, 594–601 (1957) (Cited on pages 25, 27, 29, 30, 42).

[15] A. H.-D. Cheng, *Poroelasticity*, Theory and Applications of Transport in Porous Media (Springer, Cham, 2016) (Cited on page 25).

[16] A. Norris, "On the correspondence between poroelasticity and thermoelasticity", J. Appl. Phys. **71**, 1138–1141 (1992) (Cited on page 27).

[17] D. Lynden-Bell, "Negative specific heat in astronomy, physics and chemistry", Physica A **263**, 293–304 (1999) (Cited on page 32).

[18] N. Liu, H. Liu, S. Zhu, and H. Giessen, "Stereometamaterials", Nat. Photonics **3**, 157 (2009) (Cited on page 32).

[19] J. K. Gansel, M. Thiel, M. S. Rill, M. Decker, K. Bade, V. Saile, G. von Freymann, S. Linden, and M. Wegener, "Gold helix photonic metamaterial as broadband circular polarizer", Science **325**, 1513–1515 (2009) (Cited on pages 32, 43).

[20] C. M. Soukoulis and M. Wegener, "Past achievements and future challenges in the development of three-dimensional photonic metamaterials", Nat. Photonics **5**, 523 (2011) (Cited on pages 32, 33).

[21] M. Kadic, T. Bückmann, N. Stenger, M. Thiel, and M. Wegener, "On the practicability of pentamode mechanical metamaterials", Appl. Phys. Lett. **100**, 191901 (2012) (Cited on page 32).

[22] T. Bückmann, R. Schittny, M. Thiel, M. Kadic, G. W. Milton, and M. Wegener, "On three-dimensional dilational elastic metamaterials", New J. Phys. **16**, 033032 (2014) (Cited on pages 32, 33, 55, 96).

[23] X. Zheng, H. Lee, T. H. Weisgraber, M. Shusteff, J. DeOtte, E. B. Duoss, J. D. Kuntz, M. M. Biener, Q. Ge, J. A. Jackson, et al., "Ultralight, ultrastiff mechanical metamaterials", Science **344**, 1373–1377 (2014) (Cited on page 32).

[24] J. Li and C. T. Chan, "Double-negative acoustic metamaterial", Phys. Rev. E **70**, 055602 (2004) (Cited on pages 32, 40).

[25] R. V. Craster and S. Guenneau, *Acoustic metamaterials: Negative refraction, imaging, lensing and cloaking*, Vol. 166 (Springer, Dordrecht, 2013) (Cited on page 32).

[26] T. Frenzel, J. David Brehm, T. Bückmann, R. Schittny, M. Kadic, and M. Wegener, "Three-dimensional labyrinthine acoustic metamaterials", Appl. Phys. Lett. **103**, 061907 (2013) (Cited on page 32).

[27] S. A. Cummer, J. Christensen, and A. Alù, "Controlling sound with acoustic metamaterials", Nat. Rev. Mater. **1**, 16001 (2016) (Cited on pages 32, 40).

[28] R. Schittny, M. Kadic, S. Guenneau, and M. Wegener, "Experiments on transformation thermodynamics: molding the flow of heat", Phys. Rev. Lett. **110**, 195901 (2013) (Cited on page 32).

[29] W. Zhou, P. Chen, Q. Pan, X. Zhang, and B. Chu, "Lead-Free Metamaterials with Enormous Apparent Piezoelectric Response", Adv. Mater. **27**, 6349–6355 (2015) (Cited on page 32).

[30] C. Kern, M. Kadic, and M. Wegener, "Experimental evidence for sign reversal of the Hall coefficient in three-dimensional metamaterials", Phys. Rev. Lett. **118**, 016601 (2017) (Cited on pages 32, 33).

[31] D. R. Smith, W. J. Padilla, D. Vier, S. C. Nemat-Nasser, and S. Schultz, "Composite medium with simultaneously negative permeability and permittivity", Phys. Rev. Lett. **84**, 4184 (2000) (Cited on page 33).

[32] K. Bertoldi, P. M. Reis, S. Willshaw, and T. Mullin, "Negative Poisson's ratio behavior induced by an elastic instability", Adv. Mater **22**, 361–366 (2010) (Cited on page 33).

[33] S. Babaee, J. Shim, J. C. Weaver, E. R. Chen, N. Patel, and K. Bertoldi, "3D soft metamaterials with negative Poisson's ratio", Adv. Mater. **25**, 5044–5049 (2013) (Cited on page 33).

[34] M. Briane and G. W. Milton, "Homogenization of the three-dimensional Hall effect and change of sign of the Hall coefficient", Arch. Ration. Mech. Anal. **193**, 715 (2009) (Cited on page 33).

[35] M. Kadic, R. Schittny, T. Bückmann, C. Kern, and M. Wegener, "Hall-effect sign inversion in a realizable 3D metamaterial", Phys. Rev. X **5**, 021030 (2015) (Cited on page 33).

[36] T. Mary, J. Evans, T. Vogt, and A. Sleight, "Negative thermal expansion from 0.3 to 1050 Kelvin in ZrW2O8", Science **272**, 90–92 (1996) (Cited on pages 33, 35).

[37] W. Miller, C. Smith, D. Mackenzie, and K. Evans, "Negative thermal expansion: a review", J. Mater. Sci. **44**, 5441–5451 (2009) (Cited on pages 34, 35).

[38] J. N. Grima, V. Zammit, and R. Gatt, "Negative thermal expansion", Xjenza **11**, 17–29 (2006) (Cited on page 35).

[39] J. N. Grima, M. Bajada, S. Scerri, D. Attard, K. Dudek, and R. Gatt, "Maximizing negative thermal expansion via rigid unit modes: a geometry-based approach", Proc. R. Soc. A **471**, 20150188 (2015) (Cited on page 35).

[40] J. Evans, T. Mary, T. Vogt, M. Subramanian, and A. Sleight, "Negative thermal expansion in ZrW2O8 and HfW2O8", Chem. Mater. **8**, 2809–2823 (1996) (Cited on page 35).

[41] R. Roy, D. K. Agrawal, and H. A. McKinstry, "Very low thermal expansion coefficient materials", Ann. Rev. Mater. Sci. **19**, 59–81 (1989) (Cited on page 35).

[42] R. Lakes, "Cellular solid structures with unbounded thermal expansion", J. Mater. Sci. **15**, 475–477 (1996) (Cited on pages 35, 36).

[43] C. S. Ha, E. Hestekin, J. Li, M. E. Plesha, and R. S. Lakes, "Controllable thermal expansion of large magnitude in chiral negative Poisson's ratio lattices", Phys. Status Solidi B **252**, 1431–1434 (2015) (Cited on page 36).

[44] L. Wu, B. Li, and J. Zhou, "Isotropic negative thermal expansion metamaterials", ACS Appl. Mater. Interfaces **8**, 17721–17727 (2016) (Cited on pages 36, 66).

[45] Q. Wang, J. A. Jackson, Q. Ge, J. B. Hopkins, C. M. Spadaccini, and N. X. Fang, "Lightweight mechanical metamaterials with tunable negative thermal expansion", Phys. Rev. Lett. **117**, 175901 (2016) (Cited on page 36).

[46] J. Qu, M. Kadic, A. Naber, and M. Wegener, "Micro-Structured Two-Component 3D Metamaterials with Negative Thermal-Expansion Coefficient from Positive Constituents", Sci. Rep. 7, 40643 (2017) (Cited on pages 36, 55, 59, 67, 69, 72, 73, 76, 77, 79, 83, 84, 86–88).

[47] L. Ai and X.-L. Gao, "Metamaterials with negative Poisson's ratio and non-positive thermal expansion", Compos. Struct. **162**, 70–84 (2017) (Cited on page 36).

[48] E. Boatti, N. Vasios, and K. Bertoldi, "Origami metamaterials for tunable thermal expansion", Adv. Mater. **29**, 1700360 (2017) (Cited on page 36).

[49] S. Timoshenko, "Analysis of bi-metal thermostats", J. Opt. Soc. Am. **11**, 233–255 (1925) (Cited on page 36).

[50] A. B. Pippard, *Response and stability: An introduction to the physical theory* (CUP Archive, 1985) (Cited on page 37).

[51] M. O'Donnell, E. Jaynes, and J. Miller, "Kramers–Kronig relationship between ultrasonic attenuation and phase velocity", J. Acoust. Soc. Am. **69**, 696–701 (1981) (Cited on page 38).

[52] R. S. Lakes, T. Lee, A. Bersie, and Y. Wang, "Extreme damping in composite materials with negative-stiffness inclusions", Nature **410**, 565 (2001) (Cited on page 38).

[53] T. Frenzel, C. Findeisen, M. Kadic, P. Gumbsch, and M. Wegener, "Tailored Buckling Microlattices as Reusable Light-Weight Shock Absorbers", Adv. Mater. **28**, 5865–5870 (2016) (Cited on pages 38, 39).

[54] B. Moore, T. Jaglinski, D. Stone, and R. Lakes, "Negative incremental bulk modulus in foams", Philos. Mag. Lett. **86**, 651–659 (2006) (Cited on page 39).

[55] R. Lakes and K. W. Wojciechowski, "Negative compressibility, negative Poisson's ratio, and stability", Phys. Status Solidi B **245**, 545–551 (2008) (Cited on page 39).

[56] Z. G. Nicolaou and A. E. Motter, "Mechanical metamaterials with negative compressibility transitions", Nat. Mater. **11**, 608–613 (2012) (Cited on page 40).

[57] Z. Liu, X. Zhang, Y. Mao, Y. Y. Zhu, Z. Yang, C. T. Chan, and P. Sheng, "Locally resonant sonic materials", Science **289**, 1734–1736 (2000) (Cited on page 40).

[58] N. Fang, D. Xi, J. Xu, M. Ambati, W. Srituravanich, C. Sun, and X. Zhang, "Ultrasonic metamaterials with negative modulus", Nat. Mater. **5**, 452–456 (2006) (Cited on page 40).

[59] J. Christensen, M. Kadic, O. Kraft, and M. Wegener, "Vibrant times for mechanical metamaterials", MRS Commun. **5**, 453–462 (2015) (Cited on page 40).

[60] R. H. Baughman, S. Stafström, C. Cui, and S. O. Dantas, "Materials with negative compressibilities in one or more dimensions", Science **279**, 1522–1524 (1998) (Cited on pages 40, 42).

[61] J. N. Grima, D. Attard, R. Caruana-Gauci, and R. Gatt, "Negative linear compressibility of hexagonal honeycombs and related systems", Scr. Mater. **65**, 565–568 (2011) (Cited on page 40).

[62] A. B. Cairns, J. Catafesta, C. Levelut, J. Rouquette, A. Van Der Lee, L. Peters, A. L. Thompson, V. Dmitriev, J. Haines, and A. L. Goodwin, "Giant negative linear compressibility in zinc dicyanoaurate", Nat. Mater. **12**, 212–216 (2013) (Cited on page 40).

[63] J. Qu, M. Kadic, and M. Wegener, "Poroelastic metamaterials with negative effective static compressibility", Appl. Phys. Lett. **110**, 171901 (2017) (Cited on pages 41, 92, 95).

[64] R. Gatt and J. N. Grima, "Negative compressibility", Phys. Status Solidi RRL **2**, 236–238 (2008) (Cited on pages 42, 66, 68).

[65] S. Kawata, H.-B. Sun, T. Tanaka, and K. Takada, "Finer features for functional microdevices", Nature **412**, 697 (2001) (Cited on page 43).

[66] T. Bückmann, M. Thiel, M. Kadic, R. Schittny, and M. Wegener, "An elasto-mechanical unfeelability cloak made of pentamode metamaterials", Nat. Commun. **5**, 4130 (2014) (Cited on pages 43, 55).

[67] T. Frenzel, M. Kadic, and M. Wegener, "Three-dimensional mechanical metamaterials with a twist", Science **358**, 1072–1074 (2017) (Cited on pages 43, 47, 55).

[68] M. Deubel, G. Von Freymann, M. Wegener, S. Pereira, K. Busch, and C. M. Soukoulis, "Direct laser writing of three-dimensional photonic-crystal templates for telecommunications", Nat. Mater. **3**, 444 (2004) (Cited on page 43).

[69] J. Kaschke and M. Wegener, "Gold triple-helix mid-infrared metamaterial by STED-inspired laser lithography", Opt. Lett. **40**, 3986–3989 (2015) (Cited on page 43).

[70] T. Bückmann, N. Stenger, M. Kadic, J. Kaschke, A. Frölich, T. Kennerknecht, C. Eberl, M. Thiel, and M. Wegener, "Tailored 3D mechanical metamaterials made by dip-in direct-laser-writing optical lithography", Adv. Mater. **24**, 2710–2714 (2012) (Cited on pages 43, 47).

[71] B. Richter, V. Hahn, S. Bertels, T. K. Claus, M. Wegener, G. Delaittre, C. Barner-Kowollik, and M. Bastmeyer, "Guiding cell attachment in 3D microscaffolds selectively functionalized with two distinct adhesion proteins", Adv. Mater. **29**, 1604342 (2017) (Cited on page 43).

[72] J. Fischer, J. B. Mueller, J. Kaschke, T. J. Wolf, A.-N. Unterreiner, and M. Wegener, "Three-dimensional multi-photon direct laser writing with variable repetition rate", Opt. Express **21**, 26244–26260 (2013) (Cited on page 44).

[73] M. Thiel, J. Fischer, G. Von Freymann, and M. Wegener, "Direct laser writing of three-dimensional submicron structures using a continuous-wave laser at 532 nm", Appl. Phys. Lett. **97**, 221102 (2010) (Cited on page 44).

[74] J. B. Mueller, J. Fischer, Y. J. Mange, T. Nann, and M. Wegener, "In-situ local temperature measurement during three-dimensional direct laser writing", Appl. Phys. Lett. **103**, 123107 (2013) (Cited on page 44).

[75] J. Fischer and M. Wegener, "Three-dimensional optical laser lithography beyond the diffraction limit", Laser Photonics Rev. **7**, 22–44 (2013) (Cited on pages 44, 45).

[76] E. Hecht, *Optik, 4., überarbeitete Auflage* (Oldenburg, Wien-München, 2005) (Cited on pages 45, 62).

[77] T. Bückmann, "On mechanical metamaterials", PhD thesis (Karlsruhe Institute of Technology, 2015) (Cited on page 46).

[78] M.-S. Kang, H. Ma, H.-L. Yip, and A. K.-Y. Jen, "Direct surface functionalization of indium tin oxide via electrochemically induced assembly", J. Mater. Chem. **17**, 3489–3492 (2007) (Cited on page 47).

[79] J. Reddy, *An Introduction to the Finite Element Method, 3rd Edition*, 3rd (McGraw-Hill Education, 2005) (Cited on page 49).

[80] L. Firestone, K. Cook, K. Culp, N. Talsania, and K. Preston Jr, "Comparison of autofocus methods for automated microscopy", Cytometry **12**, 195–206 (1991) (Cited on page 53).

[81] Y. Sun, S. Duthaler, and B. J. Nelson, "Autofocusing in computer microscopy: selecting the optimal focus algorithm", Microsc. Res. Tech. **65**, 139–149 (2004) (Cited on page 53).

[82] J. P. Lewis, "Fast normalized cross-correlation", in Vision interface, Vol. 95, 120123 (1995), pp. 15–19 (Cited on pages 55, 56).

[83] J. Qu, A. Gerber, F. Mayer, M. Kadic, and M. Wegener, "Experiments on Metamaterials with Negative Effective Static Compressibility", Phys. Rev. X **7**, 041060 (2017) (Cited on pages 55, 97, 108, 111, 113, 114, 116, 120).

[84] J. Qu, M. Kadic, and M. Wegener, "Three-dimensional poroelastic metamaterials with extremely negative or positive effective static volume compressibility", Extreme Mech. Lett. (2018) (Cited on pages 55, 93, 98, 99, 110, 117, 118).

[85] C. Eberl, R. Thompson, and D. Gianola, "Free digital image correlation and tracking functions", www.mathworks.com/matlabcentral/fileexchange/12413 (2010) (Cited on page 56).

[86] F. Nix and D. MacNair, "The thermal expansion of pure metals: copper, gold, aluminum, nickel, and iron", Phys. Rev. **60**, 597 (1941) (Cited on page 58).

[87] W. Overton Jr and J. Gaffney, "Temperature variation of the elastic constants of cubic elements. I. Copper", Phys. Rev. **98**, 969 (1955) (Cited on page 60).

[88] S. P. Timoshenko and S. Woinowsky-Krieger, *Theory of plates and shells* (McGraw-hill, New York, 1959) (Cited on pages 62, 99).

[89] H. Bach, ed., *Low thermal expansion glass ceramics*, 2. ed., Schott series on glass and glass ceramics (Springer, Berlin, 2005) (Cited on page 66).

[90] T. Baldacchini, M. Zimmerley, C.-H. Kuo, E. O. Potma, and R. Zadoyan, "Characterization of microstructures fabricated by two-photon polymerization using coherent anti-stokes Raman scattering microscopy", J. Phys. Chem. B **113**, 12663–12668 (2009) (Cited on page 78).

[91] A. Žukauskas, I. Matulaitienė, D. Paipulas, G. Niaura, M. Malinauskas, and R. Gadonas, "Tuning the refractive index in 3D direct laser writing lithography: towards GRIN microoptics", Laser Photonics Rev. **9**, 706–712 (2015) (Cited on page 78).

[92] L. E. Nielsen, "Cross-linking–effect on physical properties of polymers", J. Macromol. Sci. Part C **3**, 69–103 (1969) (Cited on page 78).

[93] J. E. Dietz and N. A. Peppas, "Reaction kinetics and chemical changes during polymerization of multifunctional (meth) acrylates for the production of highly crosslinked polymers used in information storage systems", Polymer **38**, 3767–3781 (1997) (Cited on page 78).

[94] J. Liu, T. Gu, S. Shan, S. H. Kang, J. C. Weaver, and K. Bertoldi, "Harnessing buckling to design architected materials that exhibit effective negative swelling", Adv. Mater. **28**, 6619–6624 (2016) (Cited on page 80).

[95] H. Zhang, X. Guo, J. Wu, D. Fang, and Y. Zhang, "Soft mechanical metamaterials with unusual swelling behavior and tunable stress-strain curves", Sci. Adv. **4**, eaar8535 (2018) (Cited on page 80).

[96] R. Warfield and F. R. Barnet, "Elastic constants of bulk polymers", Angew. Makromol. Chem. **27**, 215–217 (1972) (Cited on page 91).

[97] Q. Shi, B. Sontheimer, N. Nikolay, A. Schell, J. Fischer, A. Naber, O. Benson, and M. Wegener, "Wiring up pre-characterized single-photon emitters by laser lithography", Sci. Rep. **6**, 31135 (2016) (Cited on page 111).

[98] S. Stern, "The "barrer" permeability unit", J. Polym. Sci., Part B: Polym. Phys. **6**, 1933–1934 (1968) (Cited on page 121).

[99] B. D. Freeman, "Basis of permeability/selectivity tradeoff relations in polymeric gas separation membranes", Macromolecules **32**, 375–380 (1999) (Cited on page 121).

[100] R. Barrer and E. K. Rideal, "Permeation, diffusion and solution of gases in organic polymers", J. Chem. Soc. Faraday Trans. **35**, 628–643 (1939) (Cited on page 121).

[101] P. Kjeldsen, "Evaluation of gas diffusion through plastic materials used in experimental and sampling equipment", Water Res. **27**, 121–131 (1993) (Cited on pages 121, 122).

[102] H. Lin and B. D. Freeman, "Gas solubility, diffusivity and permeability in poly (ethylene oxide)", J. Membr. Sci. **239**, 105–117 (2004) (Cited on pages 121, 122).

[103] L. Bao, J. R. Dorgan, D. Knauss, S. Hait, N. S. Oliveira, and I. M. Maruccho, "Gas permeation properties of poly (lactic acid) revisited", J. Membrane Sci. **285**, 166–172 (2006) (Cited on page 121).

[104] L. M. Robeson, "Polymer membranes for gas separation", Curr. Opin. Solid State Mater. Sci. **4**, 549–552 (1999) (Cited on page 122).

[105] W. Sutherland, "LII. The viscosity of gases and molecular force", Philos. Mag. Ser. 5 **36**, 507–531 (1893) (Cited on page 122).

[106] W. M. Haynes, *CRC handbook of chemistry and physics* (CRC press, 2014) (Cited on page 122).

[107] T. J. Cui, M. Q. Qi, X. Wan, J. Zhao, and Q. Cheng, "Coding metamaterials, digital metamaterials and programmable metamaterials", Light Sci. Appl. **3**, e218 (2014) (Cited on page 125).

[108] B. Florijn, C. Coulais, and M. van Hecke, "Programmable mechanical metamaterials", Phys. Rev. Lett. **113**, 175503 (2014) (Cited on page 125).

[109] C. Coulais, E. Teomy, K. de Reus, Y. Shokef, and M. van Hecke, "Combinatorial design of textured mechanical metamaterials", Nature **535**, 529–532 (2016) (Cited on page 125).

[110] H. Park, H. Kwon, Y. An, W.-R. Yu, M.-W. Moon, and K. Hur, "Mechanical Metamaterials with Thermoresponsive Switching between Positive and Negative Poisson's Ratios", Phys. Status Solidi RRL **12**, 1800040 (2018) (Cited on page 125).

[111] C. Majidi, "Soft robotics: a perspective—current trends and prospects for the future", Soft Rob **1**, 5–11 (2014) (Cited on page 125).

Acknowledgments

Here I would like to thank all people who contributed to this work and supported me during my time as a PhD candidate.

First of all, I would like to thank Prof. Dr. Martin Wegener for the opportunity to work in his group on this fascinating topic, his guidance throughout the whole time, and the opportunities provided for me to present my results on international conferences. I also thank Prof. Dr. Georg Weiß, who kindly agreed to serve as the second reviewer, for his interest in this work.

I thank PD Dr. Andreas Naber for his important input regarding the Bayer filter, which has solved the measurement problems I had in the beginning.

Dr. Muamer Kadic has provided a lot of help regarding the finite-element calculations and I also thank him for all the discussions we had. It was a pleasure working with him. I have also worked together with Alexander Gerber during his bachelor thesis and thank him for the joint work and the fruitful discussions.

I want to express my gratitude to Frederik Mayer for his help at the laser scanning microscope, and to Vincent Hahn, Tobias Frenzel, Dr. Martin Schumann, and Andreas Wickberg for their time to take SEM images of my samples.

Without other group members, the time would not have been quite as fun and as productive as it was. I therefore thank all current and former group members not only for the time and all the discussions during work, but also for all the fun events we had afterwards.

Moreover I want to thank all the staff that kept everything running in the background and providing excellent organizational and technical support. Especially our technician Johann Westhauser, who has designed the sample chambers, Frank Landhäußer from the mechanical workshop, who was very excited to try out their 3D printer to fabricate a macroscopic model of my unit cell, Claudia Alaya, Monika Brenkmann, and Ursula Mösle from the secretary who were always friendly and helpful, and the electronics workshop with Werner Gilde, Michael Hippe, and Helmuth Lay, who provide an excellent IT-infrastructure at the institute.

Thanks to all the proofreaders who helped to minimize the number of errors in this thesis, namely Vincent Hahn, Dr. Muamer Kadic, Christian Kern, Tobias Frenzel, Frederik Mayer, Jessica Meier, Tobias Messer, Patrick Müller, Alexander Münchinger, Andreas Niemeyer, Jan Reiner, Heyu Tang, and Andreas Wickberg.

Finally, I want to thank my family for all their love and support, and especially my wife Heyu, who is always there for me. I am very fortunate to have her in my life.